Combining expansion microscopy with other super-resolution techniques

Inaugural-Dissertation

to obtain the academic degree

Doctor rerum naturalium (Dr. rer. nat.)

submitted to the Department of Biology, Chemistry and Pharmacy

of Freie Universität Berlin

by

Mengfei Gao

2019

This doctorate study was conducted from June 2015 to July 2019 under the supervision of Prof. Dr. Helge Ewers in the Department of Biology, Chemistry and Pharmacy of Freie Universität Berlin.

1st Reviewer: Prof. Dr. Helge Ewers, Freie Universität Berlin

2nd Reviewer: Prof. Dr. Francesca Bottanelli, Freie Universität Berlin

Date of disputation: 20.01.2020

Abstract

Expansion microscopy (ExM) was introduced since 2015 and has been fast developed since then. This technique, via physical enlargement of fluorescence carried biological samples, can resolve structures of tens of nanometers with conventional microscopes.

Here I discussed the current methods in ExM and influences of different fixation, protease digestion and labelling methods used in ExM. Validation of ExM was also carried out in the work using image registration of microtubule cytoskeletons and the 190 nm periodic structures of β-spectrin ring structures in neurons.

Next, the combination of ExM with other super-resolution techniques, *e.g.* stimulated emission depletion (STED) microscopy was proposed. The centrosome protein CEP152, the primary cilium and microtubule were resolved using expansion STED (ExSTED) microscopy. With the optimized ExSTED microscopy, a sub-10 nm 2D and a sub-50 nm 3D resolution was achieved. Structured illumination microscopy (SIM) was also attempted to image the expanded hydrogels, but severe artifacts were observed.

Finally, a tri-functional fluorescent probe was proposed, where a fluorescent dye was linked with a benzyl-guanine and an acrylic acid group. The probe was used to stain a SNAP-tagged nuclear pore protein in cells and used to crosslink proteins to acrylamide-based hydrogel in ExM.

Zusammenfassung

Expansionsmikroskopie (ExM) wurde seit dem Jahr 2015 schnell weiter entwickelt. Diese Technik ermöglicht durch physikalische Vergrößerung von fluoreszenzgetragenen biologischen Sonden die Strukturen von einigen Nanometern größ mit herkömmlichen Mikroskopen aufzulösen.

Hier diskutiere ich die aktuellen Methoden für die ExM und die Einflüsse verschiedener Fixierungs-, Proteaseverdauungs- und Markierungsmethoden, die für ExM verwendet werden. Eine Validierung dieser Methoden wurde auch in dieser Arbeit durchgeführt. Nachdem ein Optimiertes Protokoll ausgewählt worden war, wurde ExM angewendet, um β-Spektrinringstrukturen in Neuronen abzubilden. Dadurch konnten die periodischen Strukturen von 190 nm aufgelöst werden.

Als nächstes wurde die Kombination von ExM mit anderen Superauflösungstechniken, d. h. Stimulated Emission Depletion (STED) Mikroskopie, vorgeschlagen. Das Centrosomenprotein CEP152, das primäre Cilium und zellulare Mikrotubuli wurden durch den Einsatz von Expansion STED (ExSTED) Mikroskopie aufgelöst. Mit der optimierten ExSTED Mikroskopie wurde eine 2D-Auflösung von unter 10 nm und eine 3D-Auflösung von unter 50 nm erreicht. Strukturierte Beleuchtungsmikroskopie (SIM) wurde ebenfalls ausgewandt, um die expandierten Hydrogele abzubilden, es wurden jedoch schwerwiegende Artefakte beobachtet.

Schließlich wurde eine tri-funktionelle fluoreszierende Sonde vorgeschlagen, bei der ein fluoreszierender Farbstoff mit einer Benzylguanin- und einer Acrylsäuregruppe verknüpft war. Die Sonde wurde verwendet, um ein SNAP-markiertes Kernporenprotein in Zellen zu färben und um das Protein für die ExM mit einem Hydrogel auf Acrylamidbasis zu vernetzen.

Contents

List of abbreviations

PSF	point spread function
FWHM	full width half maximum
2D	two-dimension
3D	three-dimension
TIRF	total internal reflection fluorescence
HILO	highly inclined and laminated optical sheet
SMLM	single molecule localization microscopy
STED	stimulated emission depletion
SIM	structured illumination microscopy
PALM	photoactivated localization microscopy
STORM	stochastic optical reconstruction microscopy
***d*STORM**	direct STORM
PAINT	points accumulation for imaging in nanoscale topography
DyMIN	dynamic intensity minimum
ExM	expansion microscopy
CLARITY	clear lipid-exchanged acrylamide hybridized rigid imaging/ immunostaining / *in situ*-hybridization-compatible tissue-hydrogel
ProExM	protein retention ExM
NHS	hydroxy succinimide
MA-NHS	methacrylic acid N-hydroxy succinimide ester
AcX	acryloyl-X, SE, 6-((acryloyl)amino) hexanoic acid, succinimidyl ester
MAP	magnified analysis of the proteome
iExM	iterative ExM
U-ExM	ultra-structure ExM
DMAA	N, N-dimethylacrylamide
GUI	graphical user interface

PBS	phosphate-buffered saline
SDS	sodium dodecyl sulfate
ExSTED	expansion STED
PFA	paraformaldehyde
DMSO	dimethyl sulfoxide
SDS	sodium dodecyl sulfate
RPE	retinal pigmented epithelial
MDCK	Madin-Darby canine kidney
ExSIM	expansion SIM
GFP	green fluorescent protein
YFP	yellow fluorescent protein
RhoB	rhodamine B
TMR	tetramethyl rhodamine
FBS	fetal bovine serum
DMEM	Dulbecco's modified Eagle medium
BG	benzyl-guanine
DTT	dithiothreitol
aa	acrylic/ methacrylic acid
DIV	day(s) *in vitro*
MEM	minimum essential medium
MWCO	molecular weight cut off

List of figures and tables

Chapter I Introduction

Fluorescent microscopy and diffraction limit

Fluorescence microscopy is a very important tool to investigate biological questions. This method technically refers to microscopy using a fluorescent marker. When emitting with a certain wavelength of light, the fluorescent dye used as a marker absorbs and subsequently emits light at a longer wavelength. By selectively labelling the target structure using these markers and applying corresponding emission light, we can specifically track the positions of the objects and study the interaction between different biological substances.

The structures, however, are not endlessly resolvable due to diffraction limit. For example, when a single fluorescent bead with a diameter of 100 nm is imaged with the wide-field fluorescence microscope, what appears on the camera will be a more than 300 nm-sized blurry dot. And when two such beads are moving towards each other, with their distribution of the intensity, the so-called point spread function (PSF), overlapping upon each other, the two individual points will be gradually become in-distinguishable. In the late 19^{th} century, Rayleigh has pointed out this resolution limit, which is the minimum distance d between the PSFs to allow the separation of two subjects (Fig. 1.1):

$$d = 0.61\lambda / NA \qquad \text{(Equation 1)}$$

where λ is the wavelength of the illumination light, and NA equals the objective numerical aperture. The limit is also referred to as the Rayleigh criteria and is 200 – 300 nm in spatial and more than 500 nm in axial with the wide-field fluorescent microscopy (Fig.1.2 a).

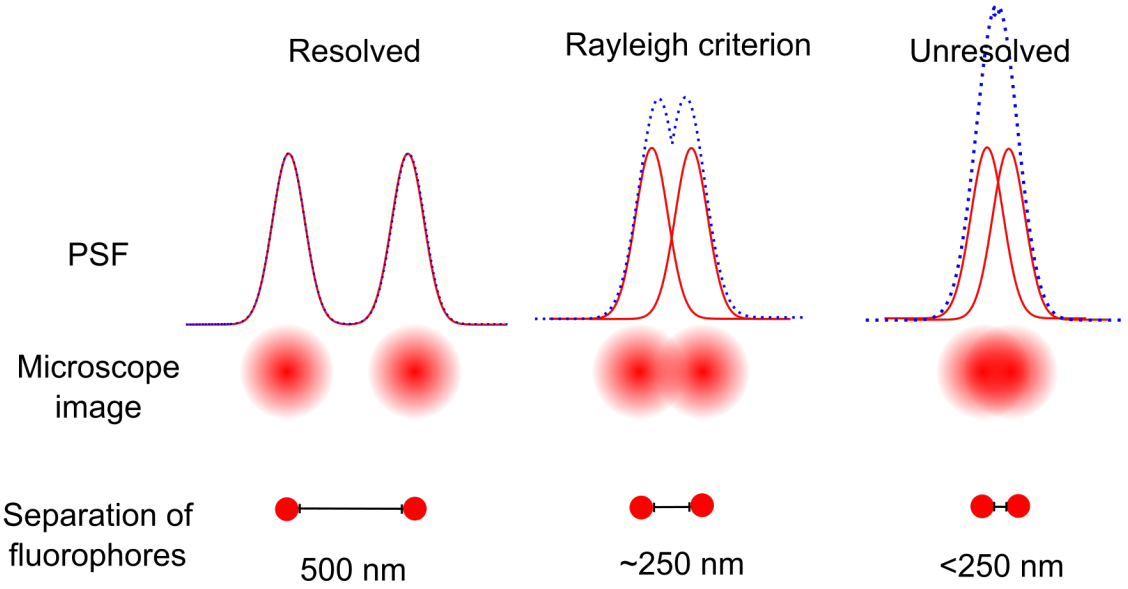

Figure 1.1 Schematic explanation of the Rayleigh criterion. When light from the sample passes through the objective, the points of the sample appear in blurry patterns. When two image points are far apart from each other, they can be easily recognized as separate objects. However, when the distance between the two points is reduced such that the first minimum of one PSF coincides with the maximum of the next, the so-called Rayleigh criterion is met and the imaging process is considered diffraction-limited, i.e. the two points cannot be resolved from one another.

Contrast-enhancing fluorescence microscopy

In the early days of fluorescence microscopy, the resolution of microscope images was restricted by diffraction limit, during when several techniques were developed to enhance the image quality, especially in improving the signal to noise ratio and the axial resolution from the basic wide-field illumination techniques. Total internal reflection fluorescence (TIRF) microscopy (Fish 2009; Mattheyses, Simon, and Rappoport 2010) (Fig.1.2 b) is one of the techniques that can greatly lower the background signal in a region closing to the surface. When the excitation light encounters the interface between two media of strongly differing refractive indices, a

high incident angle of the light results in a phenomenon called total internal reflection. A so-called evanescent wave, which travels along the interface while decaying exponentially with distance away from the surface, remains at the interface and can be employed to illuminate a fluorescence-labelled samples at the glass, specimen interface of a coverslip. Due to exponentially decay of the evanescent wave in axial direction, much of the axial background can be eliminated, hence, the contrast of the signals will be enhanced. Up to date, highly inclined and laminated optical sheet (HILO) microscopy (Tokunaga, Imamoto, and Sakata-Sogawa 2007) is also widely used and it takes the advantage of the TIRF microscopy but the illumination depth can be extended to a few μm.

Another widely used technique, confocal microscopy (Fig.1.2 c), was developed to reduce the out-of-focus blur in widefield illuminations, where the full field illumination is replaced by a diffraction limited spot illumination. Point scanning or laser scanning microscopy (Shotton 1989) and spinning disk confocal microscopy (Oreopoulos, Berman, and Browne 2014) are the most widely used confocal techniques. The former has only a single laser source to scan the field of view, while the latter utilizes multiple pinholes on a spinning disk to project thousands of excitation light beams on the sample. The subsequently detected image resolution of a spinning disk confocal microscope is lower than what can be achieved from a laser scanning microscope, but the acquisition time is greatly shortened with the help of the spinning disk induced larger illumination field (Murray et al. 2007).

The improvements of contrast can also be achieved via mathematical image reconstruction. Theoretically, the degradation or the blur of images can be described as an application of the PSF to every single point in the sample being illuminated, which is termed mathematically as convolution. And the reverse computational method is called deconvolution. There are two kinds of algorithms to perform deconvolution: 1) Deblurring, in which a 2D plane from a 3D image stack is sharpened by subtracting the blur source from its nearest neighboring stacks. 2) Image restoration, which uses the

information of the PSF to reversely derive a 3D raw image (McNally et al. 1999; Sibarita 2005).

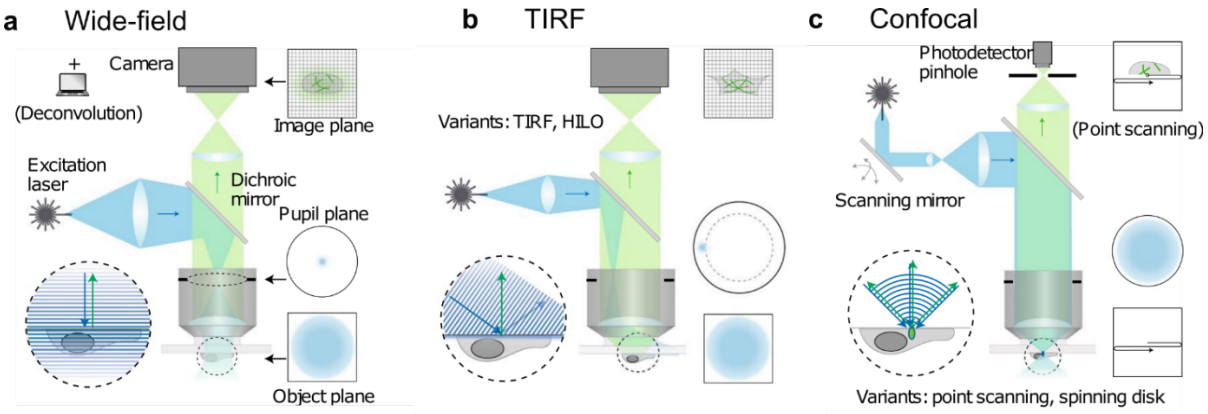

Figure 1.2 Schematic drawing of conventional imaging techniques. (a) Conventional fluorescence microscope with wide-field illumination. The excitation light is focused on a single spot in the center of the pupil plane, whereas the whole sample is exposed to the light source. (b) TIRF microscopy. In objective based TIRF, the source of light is focused on the side of a high-NA (larger than 1.45) objective, which allows an angle of incidence greater than the critical angle. In this total internal reflection stage, part of the incident light energy will pass through the interface and form an evanescent wave, which decays over depth of penetration and illuminates fluorophores near the surface (usually less than 100 nm) with high signal to noise ratio. (c) Confocal microscopy. Different from wide-field microscopy, the sample can be selectively illuminated and much of the out-of-focus or background signals can be excluded in this method, resulting in a higher signal to noise ratio. The images are further reconstructed using special algorithm to resolve sub-resolution structures. Image was adapted from (Schermelleh et al. 2019).

These techniques enhance the contrast of fluorescence-labelled biological samples and are lower photo-invasive than wide-field illumination, whereas they cannot meet

the needs of precisely detecting a few to tens of nanometer-sized sub-cellular molecules. To overcome the barrier of diffraction limit, different methodologies were developed and applied in biological researches in the past 20 years. Here I list three mainstream super-resolution microscopy techniques and briefly discuss their strength and weakness.

Super-resolution techniques

Single molecule localization microscopy (SMLM)

SMLM is a widely used super-resolution technique that has been shown to achieve a few nanometer resolution (Schlichthaerle et al. 2019; Sieben et al. 2018) (Fig.1.3 a). Although the PSF for an isolated single fluorophore emission is above 200 nm, the center position of the emission can be determined with much higher precision (less than 20 nm in lateral full-width-half-maximum (FWHM)) than its width (Mortensen et al. 2010; Thompson, Larson, and Webb 2002). By accumulating such precisely localized positions of single molecules, a sub-diffraction-limit image can be reconstructed. To utilize this technique, it is necessary to separate PSFs by keeping most of fluorophores temporally at a dark state while letting a few fluorophores stay at the emissive state and localizing them. The fluctuating emission of fluorophores that are capable of photo-switching between a bright to a dark state, is also termed as blinking.

Photoactivated localization microscopy (PALM) (Betzig et al. 2006; Shroff, White, and Betzig 2008), stochastic optical reconstruction microscopy (STORM) (Huang et al. 2008; Rust, Bates, and Zhuang 2006) and direct STORM (*d*STORM) (Heilemann et al. 2008, 2009) are variances of SMLM techniques using photoactivable or photo-switchable fluorescent proteins such as PA-GFP, EosFP, or organic dyes such as cy3-cy5 or Alexa Fluor® 647. To achieve optimized localization, choice of the fluorophores, the buffer condition which affects the blinking mechanism, labelling density and excitation illumination should all be considered.

Another variance of SMLM is DNA points accumulation for imaging in nanoscale topography (DNA-PAINT) (Agasti et al. 2017; Jungmann et al. 2010; Schnitzbauer et

al. 2017), where the blinking is generated via transient hybridization of a short (8 - 10 nucleotides long) fluorophore-conjugated single stranded DNA-oligomer and its complementary DNA-oligomer which is fixed to the biological target of interest. Since the blinking is not related directly to the photo chemistry of the fluorophores, multi-color DNA-PAINT is more straightforward via different DNA-oligomer strands.

SMLM requires a relatively long acquisition and analyzing time. For instance, the acquisition of 10,000-single molecules frames could take 10 – 20 minutes (Wegel et al. 2016). Spontaneously, the large data sets are extensively detected with automated imaging analysis algorithms during or after the acquisition (Sage et al. 2015, 2019), where the speed of the analysis also depends on the laboratory computer power. Besides, 3D SMLM is more difficult and time consuming in both imaging and image-processing than 2D SMLM, where the axial information of the image needs to be extract by measuring the changes in the shape of a PSF (Huang et al. 2008; Juette et al. 2008; Pavani et al. 2009).

In summary, SMLM can resolve sub- 20 nm structures routinely, but it remains challenging for users in labelling strategy, imaging and data analysis, especially in multi-color and 3D imaging.

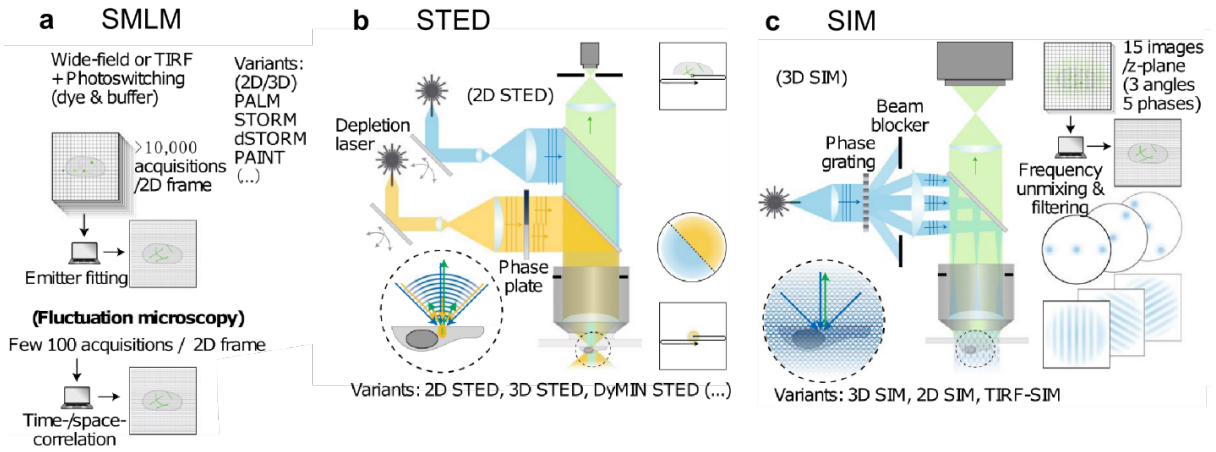

Figure 1.3 Schematic drawing of super-resolution techniques. (a) In SMLM, small subsets of fluorophores are stochastically activated such that individual molecules can be spatially resolved and their positions be determined from their single peaks. This process is then repeated many times until all molecules are localized and an image is rendered from all localized molecular positions. (b) STED microscopy is fabricated on a point scanning confocal microscopy with an extra depletion laser that compress the emission of an excited fluorophore to an effectively small region. (c) In SIM, a striped pattern of light is applied to the fluorescence-labelled sample. With the rotation and phase shift of the patterns, Moiré fringes that contains high frequency information appeared by the superimposition between the sample and the structured illumination. The images are further reconstructed using special algorithm to resolve sub-resolution structures. Image was adapted from (Schermelleh et al. 2019).

Stimulated emission depletion microscopy (STED)

Another option to enhance the resolution is achieved by reducing the effective PSF of the imaging. For instance, in STED microscopy (Hell and Wichmann 1994), a doughnut-shaped depletion laser, termed STED laser, is applied to a fluorescent sample illuminated by a laser scanning confocal microscope. On the diffraction limited fluorescence spot, the STED laser transiently turns off the fluorophores at the outer

rim of the spot through the process called stimulated emission (Klar et al. 2000). As a result, the effective PSF of STED microscopy is reduced to tens of nanometers by controlling the power of the STED laser (Westphal and Hell 2005). Meanwhile, by implementing another axial STED laser together with the spatial doughnut laser (3D STED), the axial resolution can also be enhanced up to 60 nm with some loss of the spatial resolution that is maximized to be less than 25 nm in 2D STED microscopy (Abberior GmbH; Wildanger et al. 2009). The tuning between the 2D and 3D STED imaging modes allows users to access to a balanced 3D resolution according to their needs (Fig. 1.3 b).

In comparison to SMLM, STED microscopy takes advantage of laser scanning microscopy. It takes less than a minute to scan a 50 x 50 μm^2 area. Furthermore, the image of STED microscopy is readily established without tedious post-imaging processing besides deconvolution, which makes STED microscopy widely known as a ‘seeing is believing’ technique (Bianchini et al. 2015).

For another, the employment of high-power STED laser also yields a severe photo-bleaching. Recent efforts have been put into adaptive STED microscopy. With the technique, termed dynamic intensity minimum (DyMIN) scanning, the STED laser is modulated dynamically during the imaging (Göttfert et al. 2017; Heine et al. 2017), and the minimum amount of doughnut laser is applied to the fluorescent sample, which greatly prohibits photo-bleaching and enhances the signal to noise ratio of the image.

Last, STED microscopy was not originally designed for large penetration depth imaging. A typical STED experiment is limited to 10 - 15 µm depth and when penetrating deeper, the distortion and defocusing of the depletion laser will increase, resulting in a blurred effective PSF. To overcome this problem, adaptive optics for aberration correction has been introduced to STED microscopy (Gould et al. 2012; Zdankowski et al. 2019), where the distortion of the excitation laser can be corrected using the programmable spatial light modulators (Gould et al. 2012) or a deformable mirror (Patton et al. 2016).

Structured illumination microscopy (SIM)

SIM (Fig.1.2 c) overcomes diffraction limit by taking advantage of Moiré fringes, which can be generated by applying a patterned illumination to a fluorescent sample. These Moiré fringes contain high frequency spatial information that would be elsewhere eliminated in conventional imaging techniques. After applying differently orientated structured excitations to the sample, computer algorithms are applied to extract the high frequency information and reconstruct a sub-resolution image.

Unlike the other two types of nanoscopic resolution techniques, SIM is limited to improve the lateral resolution by a factor of 2 from confocal microscopy (Gustafsson 2000). Nevertheless, this technique is favored by its fast 3D optical sectioning (Gustafsson et al. 2008), which can also be combined with adaptive optics units to achieve 3D imaging in thick tissues with less than 200 nm resolution (Turcotte et al. 2019). It should also be noted for the much broader choices of fluorophores that can be illuminated using SIM in comparison to STED and *d*STORM (Schermelleh, Heintzmann, and Leonhardt 2010).

Limitation of the current super-resolution techniques

The super-resolution techniques have been expanding at fast speed in the past 20 years. However, the employment of these techniques is still challenging in several aspects: 1) The samples need to be prepared with a preliminary knowledge of the fluorophores that are compatible with the methodology, especially when using STORM and STED microscopy; 2) Post-imaging analysis of SMLM and SIM requires some degrees of expertise from the users to eliminate artifacts (Fan et al. 2019; Sage et al. 2019); 3) Commercially available super-resolution techniques are still expensive; 4) Further improvements of resolution, i.e. applying adaptive optics or parallel laser excitation, requires changes in the optical path and can only be performed by specialists.

To pursue a simple, cost-effect super-resolution imaging, the technique called expansion microscopy was introduced to the field.

Expansion microscopy (ExM)

ExM was first proposed and demonstrated by Boyden's laboratory in 2015 (Chen, Tillberg, and Boyden 2015) and has rapidly developed since then. In the method, immunostained or fluorescence-tagged protein-expressed cells or tissues are physically enlarged by a procedure that starts with anchoring the fluorescent tag into a poly-acrylamide hydrogel. The original structure is then degraded by a protease and becomes expanded as the polymer matrix swells upon immersion in water. In this way, the position of the fluorescent tag is linked to the gel matrix instead of the original protein, and with an isotropically expanding hydrogel system, the signals would also be magnified isotropically. As a result, the distance between the fluorescent probes cross-linked to the hydrogel is physical enlarged, which allows previous optically inaccessible distances and effectively a higher spatial resolution to be resolved. The result is an effectively higher resolution achieved with standard microscopes through physical expansion of the sample.

Similar gel-embedding, digestion and magnification have been applied in some tissue clearing techniques such as clear lipid-exchanged acrylamide hybridized rigid imaging/ immunostaining/ *in situ*-hybridization-compatible tissue-hydrogel (CLARITY) (Chung and Deisseroth 2013; Tomer et al. 2014) before ExM. These clearing techniques employ different protocols using poly-acrylamide hydrogel system to increase the transparency of 100 µm to several centimeter-thick fixed biological samples, where refractive index of the sample is homogenized by removing, replacing and modifying some of its components (Ariel 2017). The reported isotropic deformation of cleared tissues varies from 0.5 to 2-fold in respect to the original structure (Richardson and Lichtman 2017).

Nevertheless, the focus in ExM has shifted conceptually from clearing tissue to allow imaging deep inside thick specimens through reduction of scattering to expanding the sample for higher resolution. And the task for the corresponding gel system was also changed from higher refractive index matching to isotropically large expansion. These

require more specific crosslinking of target molecules and a homogeneously expanded hydrogel.

In the first paper describing ExM, secondary antibodies conjugated with a single stranded DNA-oligomer coupled to a crosslinker called acrydite® was used, where the complementary ~ 30 nucleotide-long DNA-oligomer strand carrying dyes were used to deliver fluorescence to the gel (Chen et al. 2015). Besides, they added sodium acrylate, the monomer of a well-studied super absorber sodium polyacrylate, to the widely used passive tissue clearing hydrogel and verified its ability to expand cells or tissues to 4.5-fold bigger. The original protocol involves a days-long complicated protocol for antibody-DNA conjugation and DNA hybridization, and the number of fluorophores per secondary antibody is limited to 2. Although the paper opened the door for a new imaging method, the effective cost and complexity first prohibited a wide-spread application

In 2016, a next generation ExM method called protein retention ExM (proExM), was proposed by the Boyden's (Tillberg et al. 2016) and Vaughan's laboratory (Chozinski et al. 2016) independently (Fig. 1.4, Tab. 1). In the new protocol, N-hydroxysuccinimide (NHS) esters are used to carry the crosslinkable methacrylic (methacrylic acid N-hydroxysuccinimide ester (MA-NHS)) or acrylic moiety (Acryloyl-X, SE, 6-((acryloyl)amino) hexanoic acid, succinimidyl ester (AcX)) to primary amines on the exposed lysine of proteins. At the same time, Chong's lab combined the sodium acrylate containing gels with the CLARITY acrylamide-formaldehyde based crosslinking mechanism, establishing another method termed 'magnified analysis of the proteome (MAP)' (Ku et al. 2016), which drove the expansion methods back into the direction of tissue clearing. NHS ester-amide based crosslinking mechanism were more widely used in cellular level expansion, while MAP was also used in some whole-organ expansion researches.

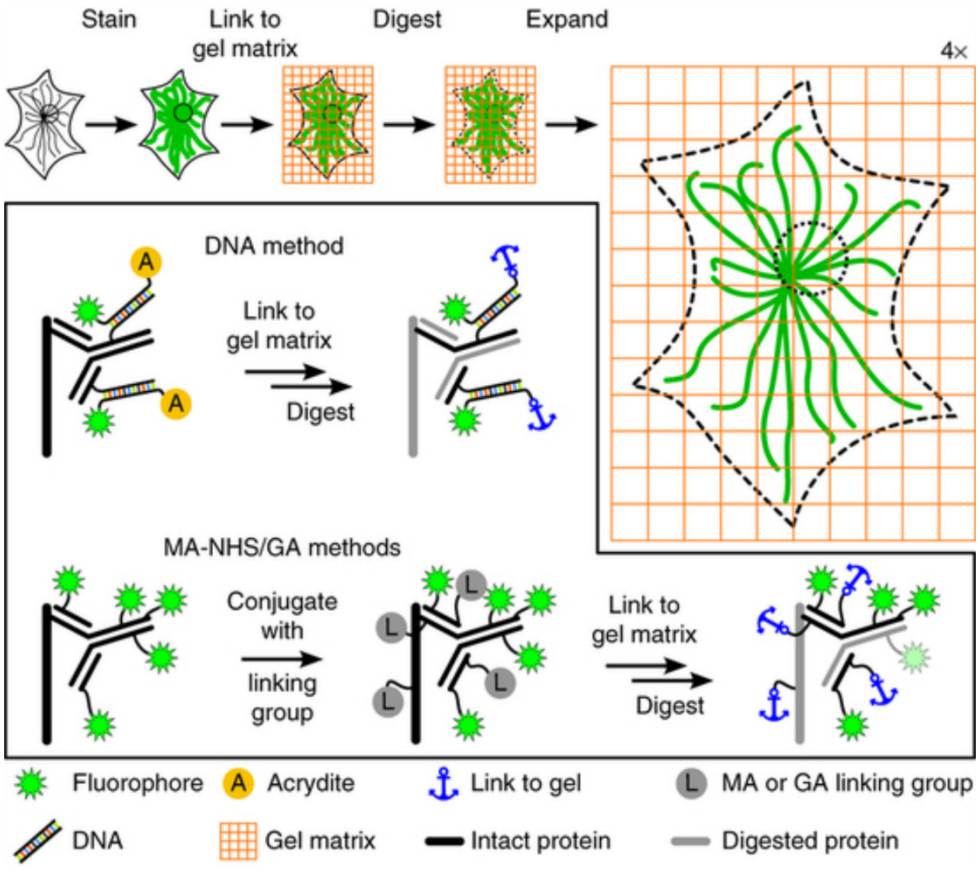

Figure 1.4 Workflows of ExM. In ExM, a cell is first immunostained, crosslinked into an acrylamide gel matrix, then digested using protease and finally expanded when soaked in water. Different linkers are used to attach the fluorophores on antibodies to the gel. In the DNA method, secondary antibodies are labelled with a DNA docking strand, and then hybridized with another complementary strand with acrydite® and fluorophores. Acrydite® serves as the anchor and after expansion the nucleotide with fluorophores will not be washed off from the relative position in gels. MA-NHS (MA) and glutaraldehyde (GA) are replacing cross-linkers which directly label the lysine and can be integrated into the polymer. After digestion, the peptide fragment with both linker and fluorescence can be preserved and be visible after expansion. Figure was adapted from (Chozinski et al. 2016).

In the last two years, efforts have been put into improvement, verification and applicability aspects of ExM (Chozinski et al. 2016; Freifeld et al. 2017; Jiang et al. 2018; Scheible and Tinnefeld 2018.; Zhao et al. 2017). On one hand, novel options of the hydrogel matrix polymer, especially in improvement of the swelling strength and more homogenous expansion, have been revealed in: 1) x10 M with up to 10-fold single step expansion (Truckenbrodt et al. 2018), 2) iterative ExM (iExM) with a two-step more than 20-fold expansion (Chang et al. 2017), and 3) Ultra-structure ExM (U-ExM) with an adjusted protocol to achieve an identical expansion factor in different cellular organelles (Gambarotto et al. 2019). On the other hand, combinations of ExM with super-resolution imaging modalities have been continuously attempted, and posed the important question: to what extent do the expanded cellular structures truly represent the native conformation in cells below the resolution limit? ExM samples with different size and origin have now been imaged on SIM (Cahoon et al. 2017; Halpern et al. 2017; Thevathasan et al. 2019; Wang et al. 2018), STED microscopy (Gambarotto et al. 2019; Gao et al. 2018; Kim et al. 2019; Li et al. 2018; Mahecic et al. 2019; Pesce et al. 2019; Unnersjö-Jess et al. 2018), SMLM (Shi et al. 2019; Tillberg et al. 2016; Tong et al. 2016), light sheet microscopy (Bürgers et al. 2019; Düring et al. 2019; Tsai et al. 2019) and lattice light sheet microscopy (Gao et al. 2019). Although the resolution stopped short of what can be routinely achieved in SMLM, especially DNA-PAINT, the appeal of ExM-based super-resolution that allows access to large volumetric imaging is still appealing.

The resolution given after ExM is greatly depended on the hydrogel swelling properties (Holback, Yeo, and Park 2011; Sadeghi and Hosseinzadeh 2010; Zohuriaan-Mehr, Mohammad and Kourosh 2008). The hydrogel system is based on homo- or co-polymers (Ahmed 2015; Maitra and Shukla 2014). For tissue-clearing applications, acrylamide-bis-acrylamide monomers were used as the substrate, the vinyl addition polymerization is initiated by a free radical generated from ammonium persulfate. Besides, tetramethylethylenediamine accelerates the process, which in turn catalyzes the polymerization (Chrambach 1985). Pore size of the hydrogel depends on both the

polymerization condition, e.g. pH, temperature (Zhou et al. 2003) and concentrations of monomers or catalyst (Rüchel and Brager 1975; Rüchel, Steere, and Erbe 1978). In ExM experiments, sodium acrylate is added to the acrylamide-bis-acrylamide monomer solution and polymerized in the same way. In MAP, the recipe is changed by increasing the acrylamide concentration to reach a denser and more robust system, where the swelling of the hydrogel in water decreases (Ku et al. 2016). While in U-ExM, the sodium acrylate concentration is maximized to ensure a more isotropic expansion (Gambarotto et al. 2019). Other monomers are also used to magnify the hydrogel expansion factor (Tab. 1). In iExM, a cleavable bis-acrylamide solution is used in the first expansion procedure and another non-cleavable bis-acrylamide is mixed in the second-round monomer solution to embed the first expanded gel. When immersed in alkaline solution, the first kind of bis-acrylamide is dissolved and the first polymer matrix collapses, whereas the second polymer matrix is preserved and can expand iteratively. This procedure involves several rounds of hybridization, signal magnification using DNA-oligomers (Chang et al. 2017). In comparison to iExM, x10 M reveals a 10-fold expansion with simplified crosslinking. In x10 M, the self-cross-linker N, N-dimethylacrylamide acid (DMAA) is introduced to replace acrylamide in the sodium acrylate containing monomer solution (Cipriano et al. 2014; Truckenbrodt et al. 2019). The polymerization is catalyzed with potassium peroxydisulfate in an oxygen-free environment. A similar hybrid DMAA-based hydrogel is used in absence of sodium acrylate, which resulted in a 7-fold expansion (Gao et al. 2019).

Table 1 Different compositions of ExM hydrogels for cultured cells

	ExM/ ProExM	7-fold ExM	X10 M	U-ExM	MAP	iExM
Monomer						
Acrylamide	2.5 %	-	-	10 %	20 %	2.5 %
N, N′-Methylenebisacrylamide	0.15 %	0.01 %	-	0.1 %	0.1 %	DHEBA/BAC*
Sodium Acrylate	8.6 %	-	6.4 %	19 %	7 %	8.6 %
DMAA	-	20 %	26.7 %	-	-	-
Potassium persulfate	-	0.17 %	0.36 %	-	-	-
Ammonium persulfate	0.15 %	-	-	0.5 %	0.5 %	0.2 %
Tetramethylethylenediamine	0.15 %	0.2 %	0.4 %	0.5 %	0.5 %	0.2 %
Buffer System	Phosphate-buffered saline (PBS)+ Sodium chloride	PBS	Water	PBS	PBS	PBS + Sodium chloride
Crosslinking	Acrydite®/ MA-NHS/ AcX / Glutaraldehyde	AcX	AcX/ MA-NHS	Formaldehyde + Acrylamide	Paraformaldehyde (PFA) + Acrylamide	Acrydite®
Disruption	Proteinse K	Proteinase K	Proteinase K	sodium dodecyl sulfate (SDS)	SDS	Proteinase K/ Sodium hydroxide
Expansion	4 - 4.2 x	7 x	9.6 - 11.5 x	4 - 4.5 x	3.3 - 3.5 x	18 – 53 x

* N, N′-(1,2-dihydroxyethylene) bisacrylamide (DHEBA)/ N, N'-Cystaminebisacrylamide (BAC)

Comparing to the complex optical setups used in super-resolution techniques e.g. SIM or STED microscopy, ExM is more like an ‘add-on’, that is easy to implement with simple optical systems in the hands of non-experts and experts. Without tedious work on optical setup or numerical calculation, the technique demands more from the sample preparation side, from fixation to gel mounting.

The biggest weakness of ExM is the loss of signal. Beginning from the fixation, a few organelles are reported to be tricky to preserve, leading to a defect in antibody labelling. During the gelation, inefficient crosslinking would result in a fragmented signal preservation in the hydrogel. Differential protease digestion or proteome dissociation can lead to up to 60 % loss of the original signal (Chozinski 2018). In a 4-fold linear expansion system, the volumetric expansion factor is 64. Therefore, taken aside all the artifacts resulting from each step, the final local fluorophore density is lowered by 64-fold by default. Without further retention or amplification of the signal, ExM might be limited in usage with conventional low-resolution techniques.

Thus, much work has been done to improve the signal at the point of imaging. A few groups reported the possibly of post-expansion staining: 1) by limited digestion or dissociation of the proteome: By using specific enzymatic reaction such as LysC which cleaves the C terminus of lysine (Tillberg 2016) or a strong detergent like sodium dodecyl sulfate (SDS) that denatures the protein, some epitopes can possibly be preserved and stained in the following gel-antibodies incubation (Gambarotto et al. 2019; Ku et al. 2016). 2) by using linkers that cannot be digested in the first place, such as nucleic acid or biotin: After the hydrogel is formed, the complementary DNA strands that carry fluorophores or fluorescence-labelled avidins will be exchanged into the gel, covalently bound to the DNA docking strain or biotin, reinforcing the loss of signal (Chozinski et al. 2016.; Kim et al. 2019; Lin et al. 2018). 3) Cryo-sectioning. Optical aberration causes a higher extinction of signals when imaging thick specimens. Some groups performed two subsequent sectioning steps in ExM imaging, one before the sample is immunostained and one after the gel is embedded (Cahoon et al. 2017; Gao et al. 2019). The former one ensures a complete labelling through the tissue, and the

latter one maximizes the volume that can be imaged. In this complicated process, delicate operation needs to be taken and a tedious stitching algorithm must be developed for this special purpose.

Aim of this work

In the beginning of my doctoral work, only three papers were published in ExM, where a similar expansion approach was implemented by the two groups, but different crosslinking reagents and homogeneity methods were proposed, which left several questions behind. In this work, the following questions were addressed:

- Which crosslinking procedure and which denaturation method is more efficient? How should one choose?

- Is protein crosslinking dependent on the chemical fixation procedure?

- Is the expansion technique compatible with smaller probes, e.g. Phalloidin, when imaging cytoskeleton structures?

- Is the expansion isotropic as reported?

- Can we combine ExM with other super-resolution techniques?

- By how much can we further enhance the resolution without much distortion?

- Can we use crosslink smaller probes into the hydrogel matrix?

Chapter II Optimization and validation of ExM treatment

Scientific background

A typical ExM experiment consists of fixation, staining, crosslinking and polymerization, protease digestion or denaturation, expansion and imaging. Changes in these procedures were partially shown to influence the final signal retentions in ExM (Asano et al. 2018; Truckenbrodt et al. 2019).

Here, we focused on different chemical fixatives (aldehydes and alcohols) and the two mainstream crosslinking reagents (AcX and MA-NHS). By changing the fixation and crosslinking conditions, we aimed to find out their influences on ExM results, which would be used to optimize ExM treatment for different organelles.

1) Fixation

Aldehydes are the most commonly used fixatives in ExM experiments, usually PFA and seldom glutaraldehyde are applied. It remains unclear that if chemical crosslinking by PFA on the proteins during fixation is a prerequisite for the later crosslinking step in ExM. To answer the question, we fixed samples using alcoholic-fixative methanol and performed ExM, where the proteins were denatured by methanol instead of being crosslinked. In this way, we will be able to show that if methanol, the widely used fixative in cytoskeleton-related super-resolution imaging, is also compatible with ExM. And if the polyformaldehyde played a crucial role in ExM-treatment.

2) Crosslinking

AcX and MA-NHS were introduced by two research groups independently (Chozinski et al. 2016; Tillberg et al. 2016) and have not yet been directly compared. The two components were different in the acid radical in that AcX is aminocaproic acid based, while MA-NHS is methacrylic acid based. The working concentrations of the two crosslinkers also vary a lot: AcX is used at 0.35 mM with more than 6 hours incubation while MA-NHS is mostly used at 25 mM for several minutes. And both chemical are used in more than 1000-fold excess to the amount used in acrydite®-crosslinked ExM

experiments (Chozinski et al. 2016; Tillberg et al. 2016). We hypothesized that the two crosslinkers are equivalent in anchoring target proteins into the hydrogels, but with minor difference in signal preservation due to the different acidic groups. To validify the hypothesis, we compared the two crosslinkers at the same concentration and labelling conditions.

Glutaraldehyde is another crosslinking reagent used in ExM. Different from the other two crosslinkers, it crosslinks amides on the epitopes with polymers and spontaneously forms Lys-Arg bridges between proteins. Purity (proportion of monomer) and pH greatly effects the crosslinking mechanism and penetration abilities of glutaraldehyde (Salem, Mauguen, and Prangé 2010). Besides, glutaraldehyde is also well-known for the strong auto-fluorescence, even in protease-digested hydrogels (Ma et al. 2016). Due to these limitations, glutaraldehyde will not be discussed in this work.

As a start, ExM variations were reproduced in this work. Fixation, crosslinking, proteolytic digestion and staining conditions were adjusted and compared to optimize an ExM protocol to visualize cytoskeletons. In the second part, we used the optimized protocol to conduct distortion analysis via 1) image registration between the expanded structure to the original structures and 2) comparison between the measured distances of spectrin rings in neurons using ExM and their known periodicity from other super-resolution techniques. With both techniques can we validify the homogeneity and reliably of our ExM experiments.

Fixation and crosslinking affect fluorescence retention in ExM

GFP-tagged proteins were shown to exhibit extraordinary stability to proteases (Chiang et al. 2001) despite several putative tryptic sites in loops that appear in the crystal structure to be exposed, e.g., Lys156, Lys158, and the dipeptide Lys214 – Arg215. It was also tested in ExM that GFP, CFP and RFP derivative fluorophores survived after limited digestion in ExM, e.g. 30 min proteinase K. In this way, GFP or mCherry were able to be used as a direct reporter for the crosslinking efficiency of AcX and MA-NHS (Chozinski et al. 2016; Tillberg et al. 2016).

Here we aimed to use GFP or mCherry as reporters to quantify how fixation methods, crosslinking reagents and duration of digestion would influence the retention of the fluorescence signals. To minimize the variance from transient over-expression, a stably transfected HeLa cell-line was used instead, where α-tubulin-GFP and H2B-mCherry were expressed. Here cells prepared on coverslips were termed pre-ExM samples, while the full-expanded structures were termed post-ExM samples.

Fixation

We started with four different fixation methods previously used in microtubule-related studies. The cells were cultured and fixed with 1) Cold methanol (M), 2) PFA and glutaraldehyde (PFAGA), 3) pre-permeabilization followed with PFA and glutaraldehyde (PFAGAT) or 4) pre-permeabilization followed with PFA (PFAT). After quenching and washing, GFP was immunostained to amplify the signals from α-tubulin-GFP. The sample was treated with ExM using MA-NHS and 1-hour proteinase K digestion (see Methods).

In pre-ExM samples, different fixation methods greatly influenced the preservation of α-tubulin-GFP (Fig. 2.1 d) and the corresponding anti-GFP-antibody signals (Fig. 2.1 e). We observed brightest microtubule signals in M from both GFP and the antibody channels (Fig. 2.1 b - c). Although PFAGA group also kept bright GFP signals, the corresponding antibody staining was less than the sample fixed with PFA. This indicate that glutaraldehyde influenced antigen-antibody binding here.

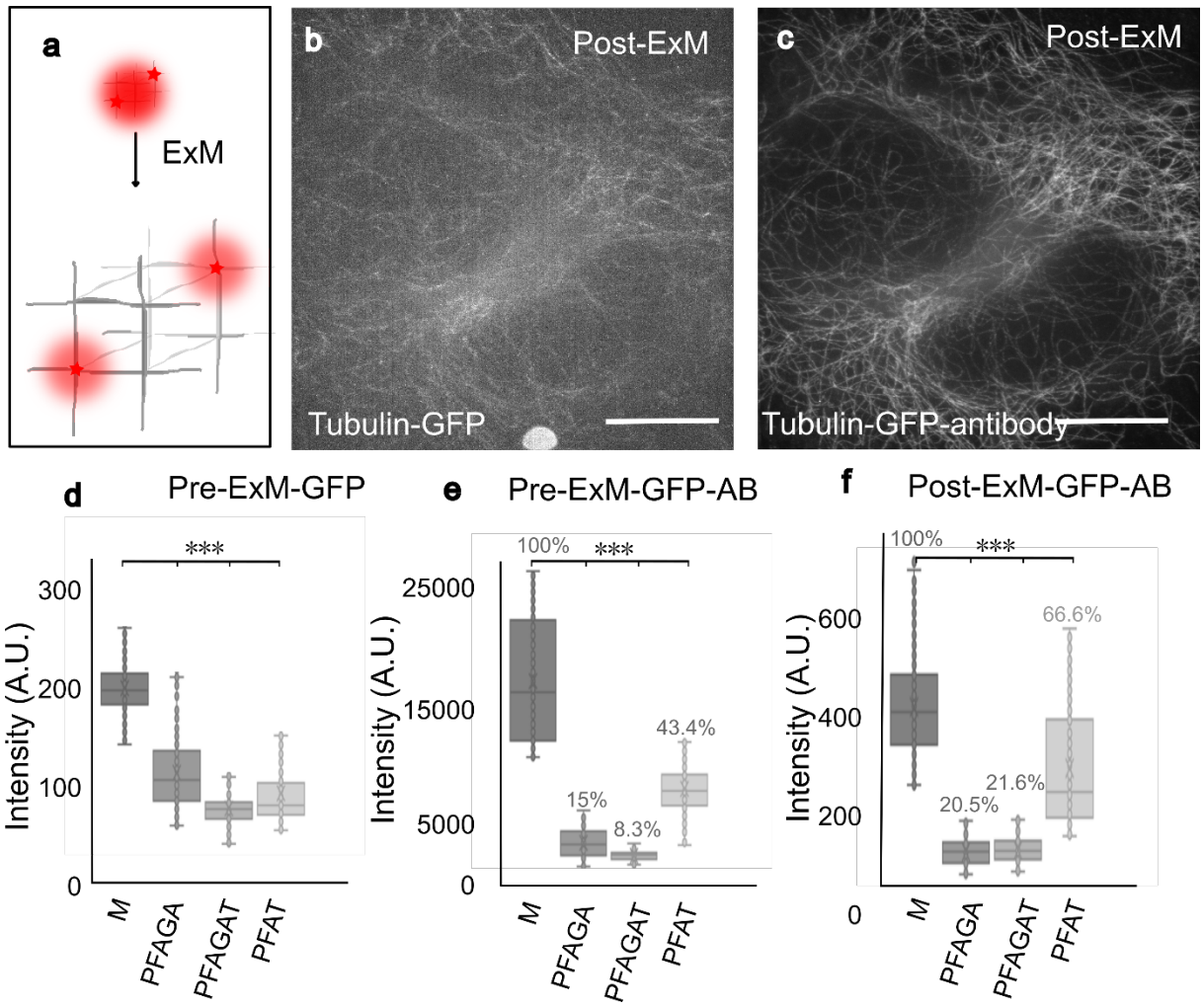

Figure 2.1 Different fixation methods applied in ExM. (a) Schematic of the expansion process. The red stars represent two dye molecules, the light red circle represents diffraction limit of light. After ExM-treatment, the distance between the dye molecules is increased due to the expansion of the hydrogel (grey matrix), so that the two dyes can be resolved individually. However, the brightness of each signal is lower than the combined signal before expansion. (b) Example of tubulin-GFP and (c) GFP antibody staining after expansion. A-tubulin-GFP-overexpressed HeLa cells were treated with four different fixation protocols (M, PFAT, PFAGAT, PFAT). (d) GFP and (e) antibodies were compared. (f) Antibody signals in post-ExM samples. Scale bar 10 µm. Boxes denote median values ± standard deviations, whiskers mark 1st and 3rd quarter of values of the distributions (n=3 – 5 coverslips or hydrogels, *** p<0.0001).

In post-ExM samples, the signal densities were lowered by at least ~4.2 x 4.2-fold from the pre-ExM case due to the expansion (Fig. 2.1 a). Thus, the remained α-tubulin-GFP signals were too low to be quantified (Fig. 2.1 b). The antibody signals were also much lower than the pre-ExM signals (Fig. 2.1 c). Nevertheless, the remaining fluorescence from the antibodies allowed a direct comparison between different fixation methods in post-ExM images (Fig. 2.1 f). We observed the same trend in post-ExM as in pre-ExM samples. M-fixaiton retained the most fluorescence, and PFAGAT kept the least. We compared the immunostaining signal retention level of the four groups by setting the average intensity of M group as 100%. The two groups with pre-permeabilization were then shown to be slightly superior to the M group in signal retention. However, the differences were not striking.

Here we concluded that ExM was compatible with all four fixation methods. When applying different fixatives or pre-treatments, different levels of chemical fixation-induced signal loss were observed. And different fixation methods also slightly changed the signal preservation after ExM-treatment.

Crosslinkers

Next, we included more parameters that may affect the ExM results. Here, we used the α-tubulin-GFP and H2B-mCherry signals as markers. The surface area of H2B gave a rough inference to the expansion factors. Besides two fixation methods (methanol and PFA), we also applied two crosslinkers to find out if different crosslinking reagent would influence the ExM result and if this influence is also relevant to fixation methods.

Cells were cultured and fixed using 1) cold methanol (M) or 2) pre-permeabilization followed with PFA (PFAT). Both fixation methods were competent to partially preserve α-tubulin-GFP signals after mild digestion. We incubated half of the samples with one crosslinking reagent MA-NHS (M), and the other half with AcX (A). Both crosslinkers were used at 1 mM and with overnight shaking (see Methods).

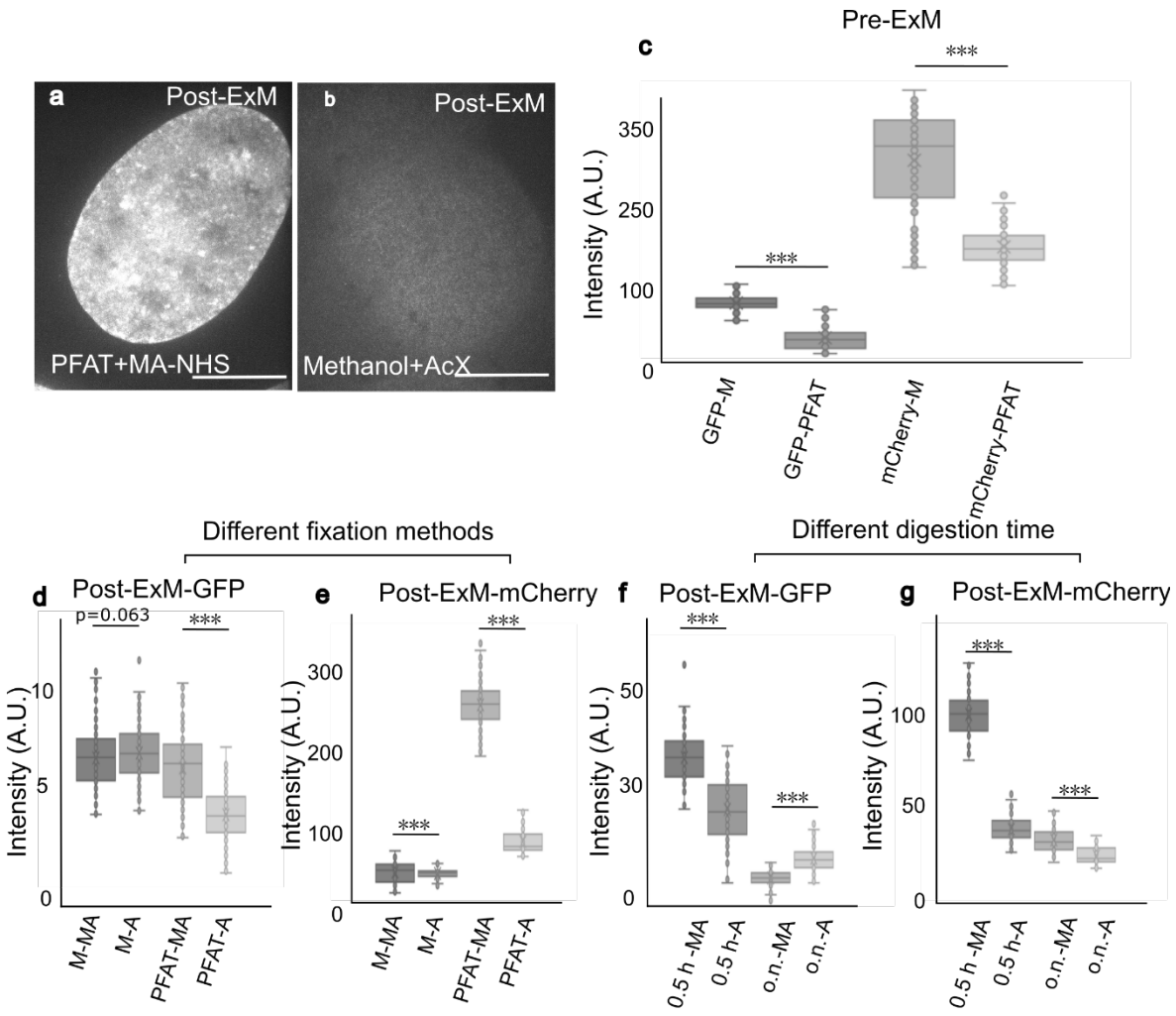

Figure 2.2 Comparison between different crosslinkers, fixation and protease digestion conditions in ExM. α-tubulin-GFP and H2B-mCherry-expressed HeLa cells were fixed with M or PFAT and crosslinked with MA or A in ExM. (a) The best and (b) the least signal retention methods for H2B-mCherry. (c) Samples were imaged and compared after fixation. (d - e) Differently fixed and crosslinked gels were digested for one hour and expanded. (f - g) M-fixed samples were crosslinked and digested differently. Scale bar 10 µm. Boxes denote median values ± standard deviations, whiskers mark 1st and 3rd quarter of values of the distributions (n=3 – 5 coverslips or hydrogels, *** p<0.0001).

Similar to the result from the last section, we did not observe significant relative signal variation in tubulin-GFP, in pre or post-ExM samples (Fig. 2.2 c - d). However, H2B-mCherry was greatly influenced by both fixation and crosslinking (Fig. 2.2 e). In the pre-ExM sample, mCherry signals were brighter in M group than PFAT group. Contrarily, after expansion, we observed stronger signal in PFAT group when crosslinked with either AcX or MA-NHS. The strongest signal difference appeared between the PFA-fixed, MA-NHS-crosslinked sample (Fig. 2.2 a) and the methanol-fixed, AcX-crosslinked group (Fig. 2.2 b), where the former one showed bright nucleus staining while the latter one did not preserve enough signals from the nucleus. Except for the extraordinarily bright group, MA-NHS and AcX did not show significant difference in signal retention.

In the next step, the third parameter was tuned, i.e. digestion time. We used cold methanol fixed, MA-NHS- or AcX-crosslinked cells to perform ExM.

Digestion duration

Previously described methanol-fixed, MA-NHS or AcX-crosslinked sample was split into two groups: One was digested for 30 minutes (mild digestion) and the other was digested overnight (strong digestion) with the same digestion buffer and temperature. Both samples were washed intensively and expanded before imaging.

After 30 minutes of digestion, GFP signal along microtubules were clearly observed in both MA-NHS and AcX-crosslinked samples, whereas after longer digestion, the signals were mostly lost (Fig. 2.2 f). As for H2B-mCherry, MA-NHS-crosslinked group preserved more signals than the AcX group when digesting for only 30 minutes. This difference was greatly shortened after longer digestion. With overnight digestion, both MA-NHS- and AcX-crosslinked gels remained similar intensity level. The main signal loss of H2B-mCherry happened between 30-minute to 1-hour digestion at 50 ºC when using methanol as the fixative and MA-NHS as the crosslinker.

As a result, when applying strong proteolytic digestion, MA-NHS and AcX crosslinking were equivalent. With shorter digestion time, some of the MA-NHS-crosslinked

samples showed stronger residual signals.

Taken together, fluorescent proteins are influenced by different fixation, crosslinking and protease disruption procedures in ExM. Labelling samples with appropriate fixation and immunostaining will also help to retain more signals in the ExM-treated samples. In terms of significant loss of signal, signal retention can be achieved via anti-fluorophore antibodies, where the signals from antibodies were also affected by fixation protocol but relatively less than that from fluorescent proteins.

Comparison between pre-ExM staining and post-ExM staining

After analysis of the fixation, crosslinking and digestion conditions for pre-ExM staining (pre-staining), we aimed to test the post-ExM staining (post-staining) protocols and check if the post-staining was generally better in preserving structures.

To do so, fixed samples were crosslinked with an acrylamide/ PFA mixture. During the hours-long incubation, the mixture spontaneously reacted with amides on proteins and the crosslinked amides were later directly polymerized into a hydrogel matrix. After gelation, the samples were disrupted using SDS containing denaturation buffer at 95 ºC. The staining was done after the gel is cleared and expanded. The protocol worked well in expanding sectioned brain tissues with GFP-labelled organelles (Fig. S2). The protocol was later optimized to achieve an equivalent expansion scale for the gel and the purified proteins conjugated to the gel (Gambarotto et al. 2019). Here we used this optimized protocol (U-ExM) to expand and visualize microtubules in cultured cells and compared the result to ExM-treated samples (see Methods and Appendix).

Microtubule-immunostained HeLa cells were used in the experiments. The cells were first cultured on coverslips and fixed. One coverslip was first immunostained and treated with ExM, while another coverslip was treated with U-ExM and expanded gel was immunostained. Here I used the identical polymerization conditions (U-ExM monomer solution, gelation temperature and duration) for both samples, so that the hydrogels expanded at the same scale.

In both pre- and post-staining samples, microtubule cytoskeletons were well-resolved.

The post-staining gel gave comparable continuous microtubule signals as the pre-staining gel but was with much speckled background (Fig. 2.3 a, c). Patterns of signals can be found at different depth of the hydrogel, intracellular and extracellular. Precipitation of crystals were also observed on the surface of hydrogel when leaving the gel in cool condition (lower than 8 ºC), which was likely caused by the remaining SDS in the hydrogel. The phenomena got sever in old denaturation buffers than freshly prepared ones, even though pH values of the buffers did not significantly change.

After 3 days of room-temperature or low-temperature storage, signals in the post-staining gel were lost, with fluorescent particles diffusing in the whole gel. While in the AcX-crosslinked, proteinase K-digested gel, after half year of dehydrated storage, the signals were also decreased but still visible (Fig. S5). The morphology of microtubule was slightly different (Fig. 2.3 b, d). Zig-zag shaped bending of microtubules can be found near the bottom in the post-staining gel, but not in the pre-ExM sample. We also observed similar damage in MAP treated cells, where the gel was also incubated in alkaline solution at near-boiling temperature (Fig. S6).

Cross-sections and longitudinal sections were measured along the microtubules (Fig. 2.3 e, f). FWHM of the cross-sections were similar in both cases. Along the microtubule, signal fluctuating was not significantly different, where antibody accessibility was limited by its physical size. And in the post-staining group, microtubules appeared dottier, suggesting that tubulins were physically stretched apart from each other at the point of immunostaining. We briefly measured the signal to noise ratio in each case, and ExM showed higher strength, but in the cost of more intensive blocking and staining.

The post-staining experiments were also performed with mild-digested ExM samples and pre-labelled MAP-treated sample (Fig. S7), where the post-staining was less continuous or with lower intensity than the corresponding pre-staining samples.

As a conclusion, both pre-staining and post-staining in ExM and U-ExM allowed access to brightly labelled microtubule cytoskeletons. But the denaturation and post-staining

in U-ExM also resulted in a higher background than pre-staining.

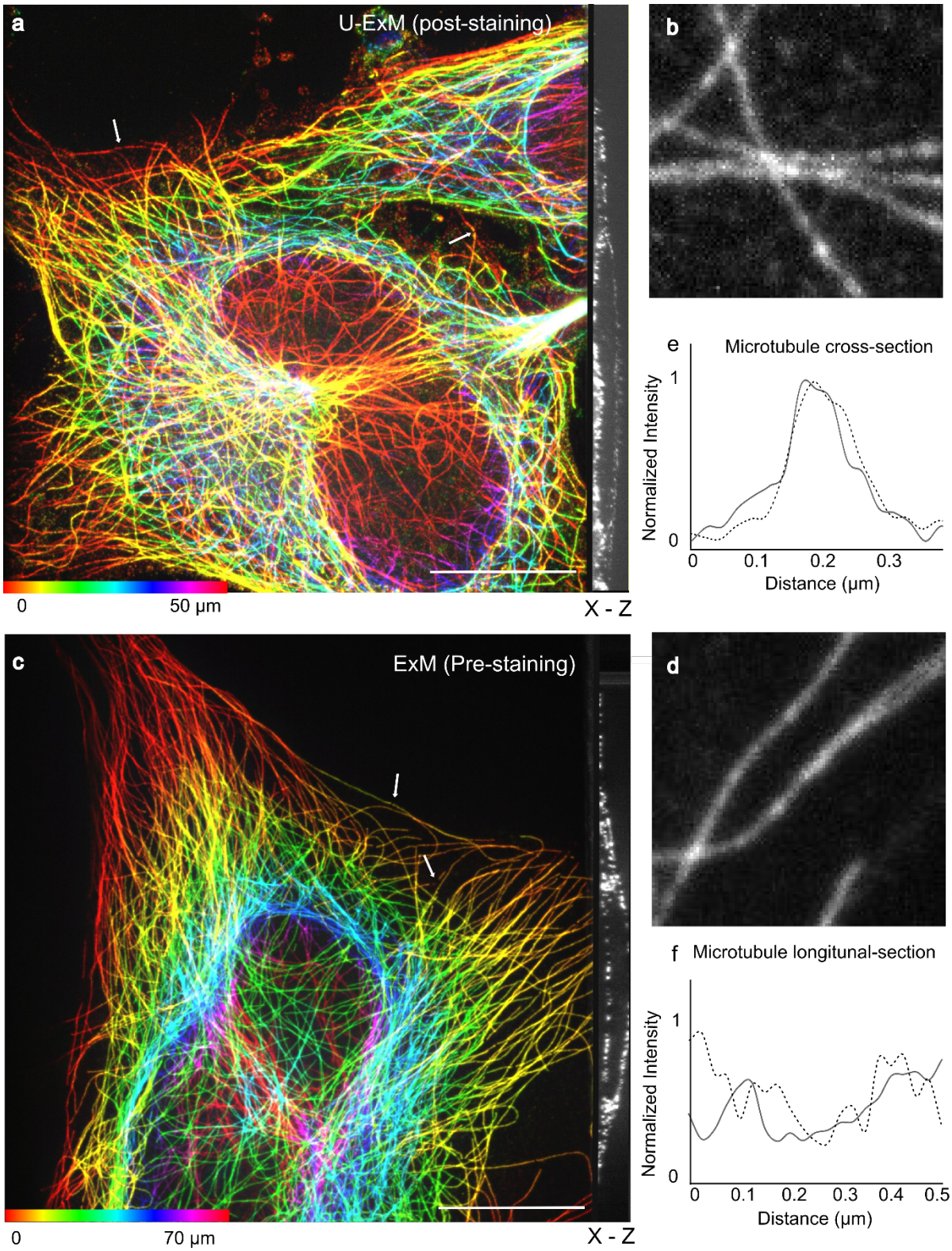

Figure 2.3 Comparison between pre- and post-staining. HeLa cells were fixed using methanol and proceeded with (a) U-ExM or (c) ExM using the same anti-tubulin antibodies. The expanded gels were imaged on a confocal microscope with 0.5 µm Z-

scanning step size. Z-projections were taken for (a) U-ExM and (c) ExM. (b) and (d) were the magnified region from single plane in (a) and (c) correspondingly. The side-view across the gel were shown on the right side of (a) and (c). (e) Line-scans were made perpendicular to a single microtubule, and the cross-section intensities were normalized (U-ExM in gray solid, ExM in dashed line). (f) Line-scans were taken along a single microtubule, with results representing the fluctuation of intensity in the expanded microtubules (U-ExM in gray solid, ExM in dashed line). White arrows indicated the non-continuous part of the microtubule. Scale bar 10 μm. (b) and (d) are in 10.8x10.8 μm^2 sized.

Validation of isotropy of ExM using microtubule cytoskeleton

By comparing different variants of ExM, we optimized our protocol to perform ExM-treatment on cytoskeleton structures, especially microtubules. Here, we used the morphology of microtubule cytoskeleton in cultured cells as a marker to compare the pre- and post-ExM. By rotating and resizing the post-ExM image, we overlay the post-ExM image to the pre-ExM image, where the distortion level was calculated.

In a typical microtubule-related experiment, Hela cells were immunostained with anti-α-tubulin antibody conjugated with Alexa Fluor® 488 and anti-β-tubulin antibody plus a secondary antibody conjugated with Alexa Fluor® 568 against the both primary antibodies. With this labelling strategy, we can use two different excitation lasers to image the pre-ExM and post-ExM samples, which preserved a better signal to noise ratio in the post-expansion image.

The immunostained coverslip was first imaged with spinning disk confocal microscopy in the green channel. A view in the center area of the coverslip was taken and a Z-scanning through a cell was done with 0.1 μm step size using a 60 x/ NA 1.42 oil-immersion objective (Fig. 2.4 a). The step size was chosen for the subsequent 3D reconstruction, whereas the axial resolution was higher than double of the axial

resolution in this case when measured with beads.

After that, a 20x air objective was used to capture an array of 3 x 3 field of view near the cell region for later identification. The sample was treated with the ExM protocol. After expansion, a picture was taken for the entire gel, and an approximately 15 x 15 mm region in the center of the gel was excised with the help of a gridding foil underneath. The gel was imaged again the confocal microscope in the green signal channel, using the 20x air objective. Cells with a prominent morphology such as dividing cells, cells of cuspidal shape or extraordinary large size were used as landmarks to identify the region imaged in the pre-ExM sample. It was immediately apparent, that the imaged cells exhibited much lower intensity in the green channel compared to the surroundings. When the cell was located, a Z-scanning was taken from the bottom to the top of the expanded cell with 561 nm laser and the corresponding red filter (Fig. 2.4 b). Although only 2D distortion analysis was performed until now, 3D distortion analysis algorithm is still in development. For a better 3D reconstruction, here a step size of 0.1 µm was taken to be equivalent to the physical spatial pixel size (~0.1 µm).

The expansion-induced distortion in x-y plane was measured using a MATLAB script written by Dr. Amin Zehtabian. A 3D comparison algorithm was not yet applied since the axial resolution in the pre-ExM case was relatively low (~1 µm). When using the script, regions for comparison was first manually selected in pre- and post-ExM images and cropped using ImageJ. Microtubules near the bottom of surface and at the edge of the cells were primarily selected due to their strongest fluorescence and more isolated structure. Both images were imported using the graphical user Interface (Fig. 2.4 c), and a partial differential equation-based denoising (Barbu 2013; You and Kaveh 2000) were applied. The pre-ExM image was used as a static reference, and the post-ExM image was transformed to reregister according to the reference, which was termed as ‘moving’. A non-rigid transformation algorithm including translation, rotation and resizing was applied to achieve the maximum likelihood between the two images, and the total distortion was measured radially from the center of the reference. The

pre- and post-ExM images were then presented in different colors and displaced as an overlay in one image, with another image indicating the relation between distortion along squared displacement.

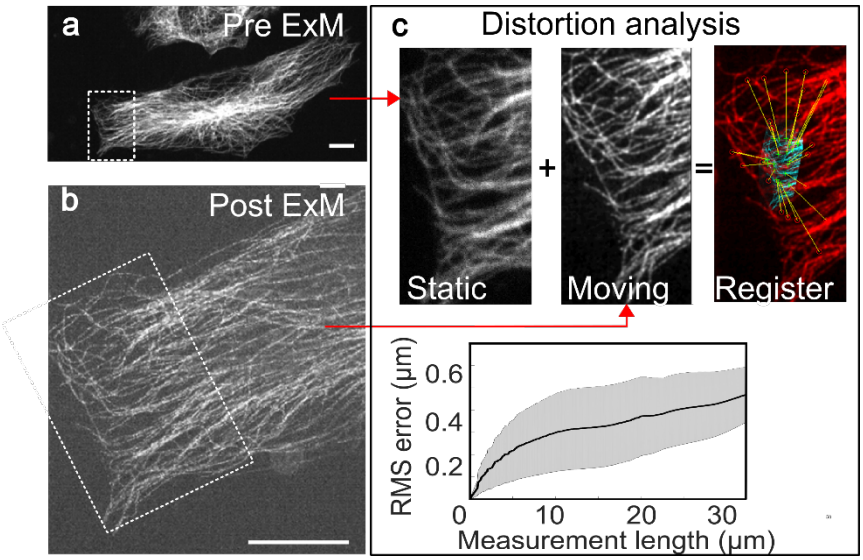

Figure 2.4 Distortion analysis of an expanded sample. (a) HeLa cells were immunostained against β-tubulins and (b) treated with ExM. (c) The pre- and post- ExM images were cropped and processed for distortion analysis. The pre-ExM image was used as ‘static’, while the post-ExM image was termed ‘moving’, which was later transformed to fit the size and orientation of the static image. The images were overlain to perform registration. Displacement between images were analysis from the center of the moving image towards the boundary of the structure. Root mean square (RMS) errors were measured. Scale bar 4 µm.

The overlay between pre- and post-ExM images allowed a direct comparison between pre- and post-ExM samples and quantitative analysis of the distortion level, which was less than 2 % for microtubule-immunostained cells.

With the direct comparison, both pre- and post-ExM images should be with high contrast and much effort had to be put to locate the same structures in a hydrogel. This,

however, can be simplified by using a known structure, where only post-ExM image was optimized and used to estimate the distortion, for instance, ~190 nm-spaced spectrin rings in neuron.

Validation of isotropy of ExM using periodic spectrin ring structures in cultured neurons

The β-II spectrin interconnects around 190 nm spaced actin rings that are found along the initial segment and over the entire axon in neuronal cells (Fig. 2.5 i). Since the C-terminal peptide recognized by the commercially available antibody is located exactly between the 190 nm spaced rings, a similarly 190 nm spaced repetitive structure is apparent in super-resolution microscopy of β-II spectrin along the axons. It was first shown in 2013 with STORM (Xu, Zhong, and Zhuang 2013) that actin formed ring like structures wrapping around the circumference of axons, with a spacing of 190 nm and has been widely studied with other super-resolution techniques e.g. STED (D'Este et al. 2017). By expanding spectrin ring structures, we were also access to sub-resolution arrangements of proteins. Here we aimed to show spectrin structures in neurons that are organized in a well-known periodic pattern can be used to calculate the distortion of ExM-treated samples.

We first imaged expanded neurons immunostained for β spectrins at several different *days in vitro* (DIV) and applied deconvolution on post-ExM images to further improve the visualization of the ring structure with spinning disk confocal microscopy. The DIV 7 and DIV 15 mouse hippocampal neuron cells were fixed and immunostained against β-II or -IV spectrins before ExM-treatment.

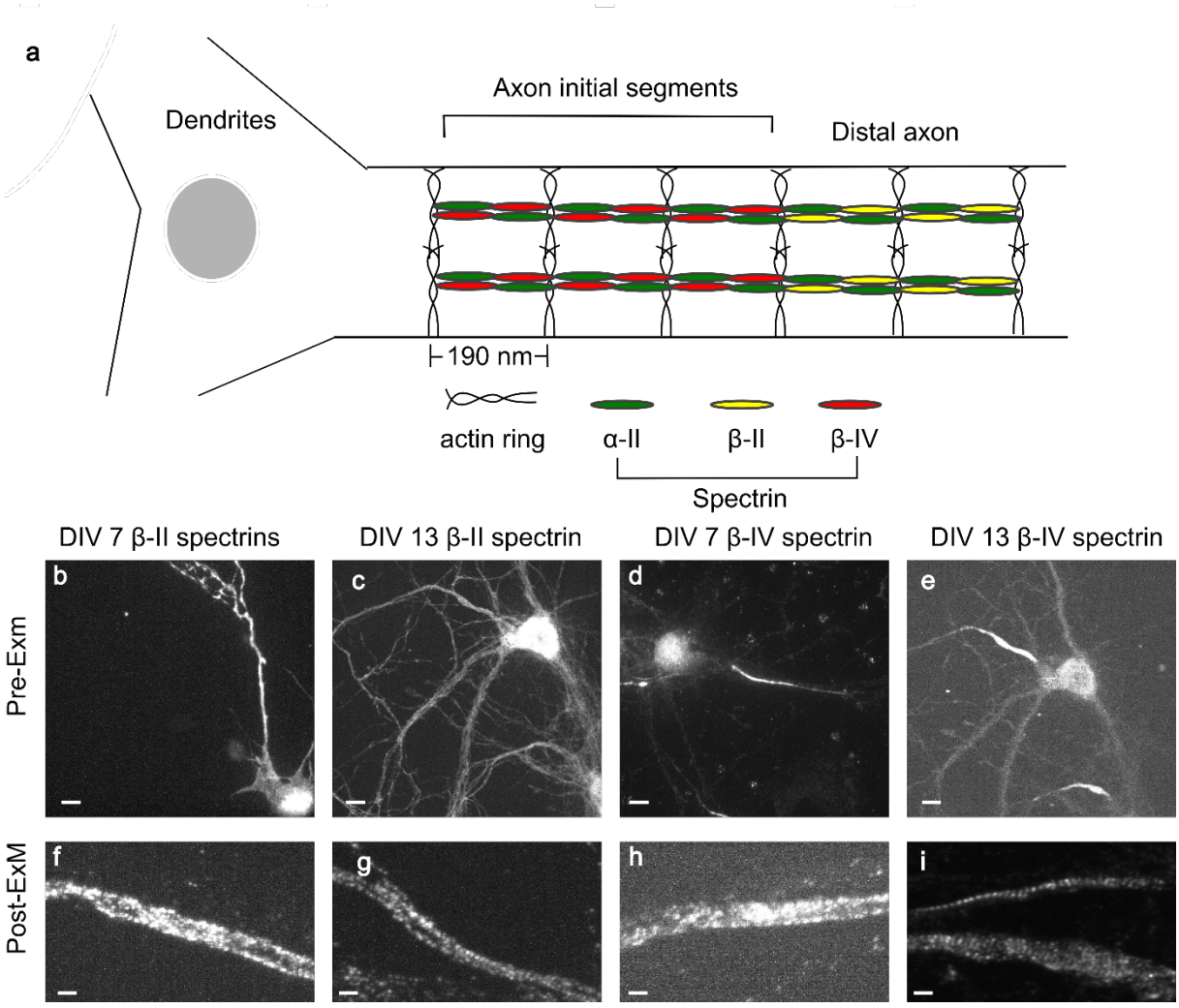

Figure 2.5 Pre- and post-ExM images of spectrin ring structure in neurons. (a) Diagrammatic sketch of spectrin tetramers along the axons and their bundling with actin rings. Figure was adapted from (Liu and Rasband 2019). (b - e) Immuno-fluorescence-labelled β-II (b - c) and -IV (d - e) spectrin structure in a primary mouse hippocampal neuron at (b, d) DIV 7 or (c, e) DIV 13. (f - i) Expanded axons. Only after ExM-treatment can these ring structures be resolved with a confocal microscope. Scale bar 4 µm in (b - e) and 1 µm in (f - i).

In pre-ExM samples, both anti-β-II and -IV spectrin antibodies accumulated in the soma, meanwhile β-II disperses over the whole neuron without special differences between axon or dendrites whereas β-IV was expressed specifically in the initial segment in the

axon (Fig. 2.5 a - d). After expansion, the unspecific bindings of antibodies in soma or on the surface decreased comparably, providing a closer look into the β spectrin ring structures. In DIV 7, both β-II and -IV spectrins wrapped in periodic structures along the axon with periodic dotted pattern along the initial segment (Fig. 2.5 e, g). At DIV 13, β-IV spectrin performed almost the same as DIV 7 group while β-II spectrin was recruited in a patterned form all over the neuron (Fig. 2.5 f, h). The periodic rings were not only visible occasional along the axon as in DIV 7, but also can be found in dendrites as previous reported (Leterrier et al. 2015).

The periodic structures in DIV 13 samples were further extracted from the images and line-scans were taken along the axon-direction in a single frame, which was usually the upper-surface of the axons. The line-scans were averaged and calculated with auto-correlation function to quantify the periodicity, where the distances were divided by the corresponding hydrogel expansion factors. In the expanded β-IV spectrin-stained DIV 13 neuron, complete and periodic ring structures were clearly observed (Fig. 2.6 a, b) and 185.1 ± 17.9 nm (mean ± standard deviation) spacing were calculated from the image. However, in the expanded β-II-stained sample, the background was relatively high, although ring structures were visible, quantification of the periodicity was difficult (Fig. 2.6 c). Thus, deconvolution was applied to subtract background and increase the signal to noise ratio near the ring structures (Fig. 2.6 d, e) using Huygens software. Periodic structures of β-II were quantified with the deconvoluted image, where a 189.7 ± 18 nm spacing was achieved.

With both β-II and -IV spectrins, we were able to resolve the ~190 nm periodicity with less than 10 % variance. And this periodicity was calculated with the hydrogel expansion factor, which indicated that the expansion factor of the spectrin structures along the axons were also ± 10 % from the hydrogel expansion factor. Besides, the spectrins analyzed from different gels made of same batch of monomer solution were similar, which proved the isotropic expansion of our ExM-treated samples in tens of nanometer range.

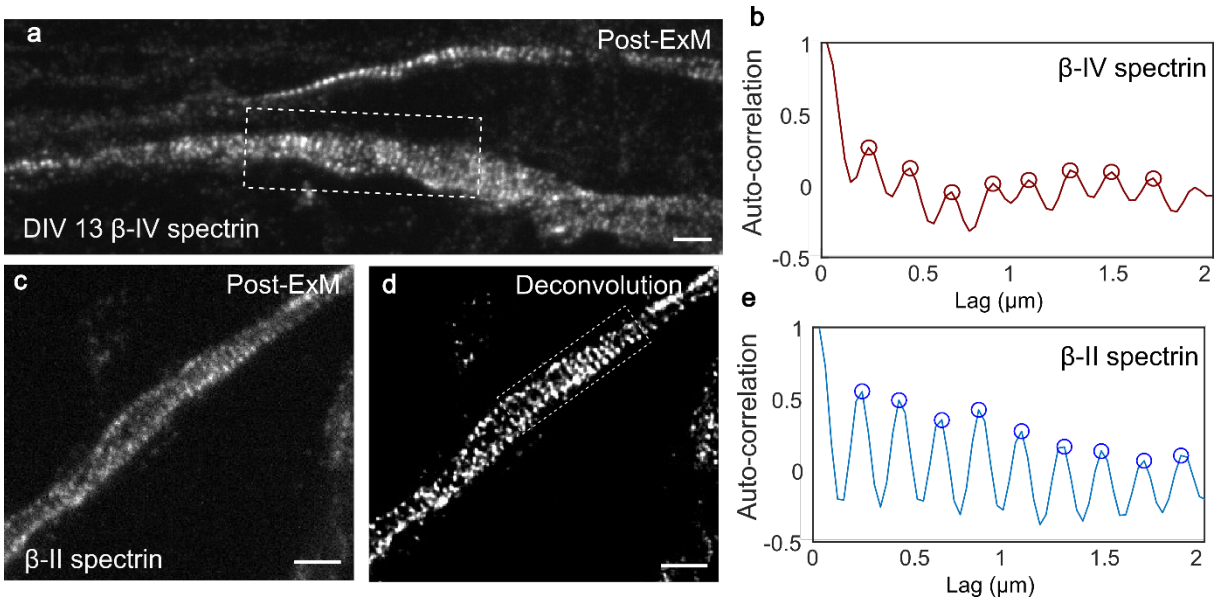

Figure 2.6 ExM images of spectrin ring structure in neurons. (a) Immuno-fluorescence-labelled β-IV spectrin structure in a primary mouse hippocampal neuron was expanded, where the periodic structures were marked with the box. (b) Averaged autocorrelation function of deconvoluted βIV spectrin for the chosen region (n=14, 2 gels). (c) β-II spectrin structure was expanded with ExM and the signal to noise ratio was relatively lower than β-IV. (d) The image was deconvoluted, resulting in a periodically patterned structure with higher signal to noise ratio. (e) Averaged autocorrelation function of deconvoluted βII spectrin for the chosen region (n=18, 2 gels). The images were taken with spinning disk confocal microscopy. Scale bars are 1 μm.

In conclusion, here we established direct imaging of sub-resolution β spectrin structures on spinning disk confocal microscopy in combination with ExM. We utilized the sub-resolution structures observed in ExM and the structure resolved from other super-resolution techniques to calculate the distortion along the axons.

Discussion

Fixation and crosslinkers

Different fixation methods, i.e. methanol, PFA, in supplementary with pre-permeabilization or glutaraldehyde, were tested in this work with ExM. We did not observe any failure of ExM due to the fixation process until now. However, it was also shown in this work that different fixatives affected signal preservations after ExM and this influence varied between proteins, for instance tubulin-GFP and H2B-mCherry.

In the experiments, we also observed differences in AcX- and MA-NHS-crosslinked ExM treated samples. And it remained unclear why MA-NHS-crosslinked samples continuously lose fluorescence over longer digestion times, while AcX achieved the digested state faster, or in other words, the signals were rapidly lost in a short time and subsequently remained at a lower level for longer digestions with proteinase. It could also be that AcX-crosslinked to less targets in the beginning. Another guess is that MA-NHS can form some protective matrix like structure on the epitopes, and in short-time prevents the fluorescent tag from digestion, and with longer incubation, the protection is loosened with the protein slowly exposed to the protease.

Here we did not exclude the possible DNA-protein interactions, where the binding of H2B to DNA may lead to its transient resistant to proteinase K digestion. Future experiment should be carried out with supplemented deoxyribonuclease.

Pre- and post-staining

Regarding the labelling procedure, a pre-staining protocol is superior compared to the post-staining in most applications. First, the reproducibility of U-ExM in cultured cells is lower than for ExM. In the several attempts, I observed some inhomogeneous staining when using different primary antibodies. This may result from the harsh denaturation condition, and maybe the antibody recognition site was lost in the unfolding of the antigens. In both cases, antibody staining, or the denaturation conditions need to be tested carefully before the real experiments. Besides, the 3-hour primary antibody incubation time proposed from the original paper (Gambarotto et al.

2019) did not work in my hand when using less than 2 ml of total staining buffer solution. Thus, a large number of antibodies needs to be applied to the post-staining. Secondly, the U-ExM protocol was proposed to ‘calibrate’ expansion for proteins and gave a better access to compact structures. In studying microtubule cytoskeletons of cultured cells, the epitopes are usually well exposed before expansion, and the expansion of the massive skeleton is closer to the expansion of the hydrogel than that of a small isolated structure. Finally, SDS solution is known to precipitate in hydrogels, increasing the laser scattering and prompts a significant background. To avoid the problem, at least 2-day-long washing of the hydrogel was recommended in tissue clearing protocols. In cultured cell experiments, we shortened it to hours, which speeded up the whole preparation but increased the background as well.

Nevertheless, in pre-staining samples, cyanine dyes, e.g. Alexa Fluor® 647 or cy3, interact with other monomers in the polymerization thus lost fluorescence after gelation (Asano et al. 2018). In comparison, in post-staining experiments, these dyes are added after polymer matrix was formed and preserved fluorescence in the expanded samples. In the future, with the photo-switchable cyanine dye-stained hydrogels, we will be accessed to perform SMLM on expanded samples.

Distortion measurements

In microtubule labelling, we occasionally observed a concave deformation underneath the nucleus which was not seen in the pre-ExM system. It indicated that the nuclei acid or lipid in the compact nuclei prohibit the outward movement along with the hydrogel expansion. This phenomenon might be easily corrected by using nuclease (DNAse or RNAse) or an increase in the protease digestion time and emphasizes that a careful distortion measurement must be performed to confirm the correction factor for each measurement.

Microtubules are the most widely used landmark for the distortion analysis. The pre- and post-ExM image registration gave simple and direct information on the expansion-induced distortion. However, to calculate distortions at tens of nanometer scale, sub-

resolution images of pre- and post-ExM samples are both required, where the target structures should be also bright and integrated. Thus, we used another indirect way to show the distortion level, by comparing the measured distances using ExM to the known structures achieved by electron microscopy or other super-resolution techniques.

We showed here that the sub-resolution periodic β-spectrin rings can be used to calculate distortions. Nevertheless, other indicators this calculation are still necessary for non-neuronal cells. A ~200 nm sized spherical-shaped structure with accessibility to intensively labelling is ideal. The structure should also be rigid against commonly used fixation and permeabilization methods. With the help of these expansion rulers, ExM-treatment will be higher credibility and accurate.

Workflow of ExM when using a new construct

Taking fixation, crosslinking and staining into account, we proposed a workflow to optimize ExM protocol for a target protein. When imaging a new construct using ExM, existing fixation and fluorescent labelling protocols should be examined beforehand (Fig. 2.7). If none of these are available, it is easier to start with the overexpression of fluorescent protein-tagged structure and image using anti-fluorophore antibody. PFA-fixation and MA-NHS mild digestion, which were shown in this work to maintain the most signals. If one variance of ExM-treatment does not work, other fixative, crosslinking, post-staining should be applied. At this step, signal retention is more important than expansion. However, after the protocol is optimized, and shows expanded fluorescent structures, optimization should be carried on ensuring a full digestion, full expansion and low distortion level.

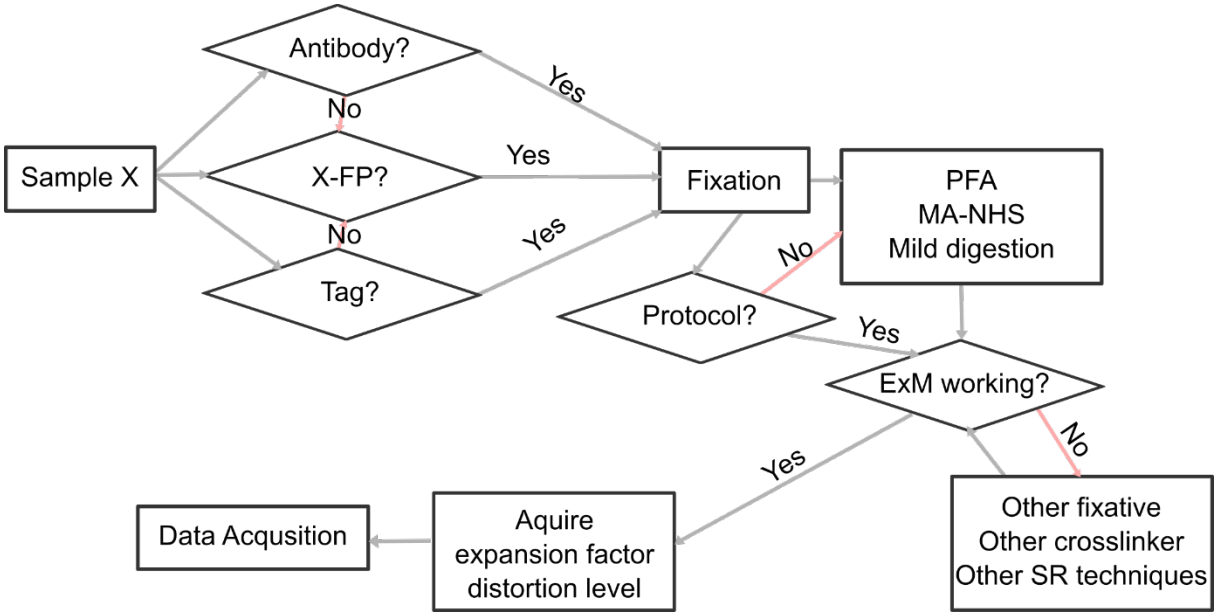

Figure 2.7 Workflow to perform ExM. When imaging a structure 'X' with ExM for the first time, labelling should be well prepared via either antibody immunostaining or a crosslinkable fluorescent tag, when either was not yet available, overexpression of fluorescent protein-tagged construct (X-FP) can be used in combination with an anti-FP antibody to perform ExM. In the case where the fixation/ expansion protocol is not well-established, start with 4 % PFA with 1 - 25 mM MA-NHS as crosslinker, followed with mild protease digestion (such as Proteinase K at 50 ºC for half hour or SDS containing denaturation buffer at 37 ºC for 1 - 2 hours). If the expanded signal is not optimal, adjust fixation, crosslinking procedure accordingly, and check the original sample with other super-resolution techniques. If the expansion is successful, change the digestion condition to adjust the expansion factor, and compare the pre- and post-ExM images to calculate expansion factor (EF) and distortion level (may not be applicable). Finally, the ExM assay is established and ready for data acquisition.

Outlook

With the concept of expansion, other forms of physical enlargement can probably be introduced. Polymers used in the electronic engineering field can deform uniformly in

1D or 2D when applying external stretching. If a cell is embedded in the gel and partially cross-linked to the matrix, the external deformation and internal reaction of different components of the structure may be used to identify cellular interactions. And by stretching a gel in 2D or 1D, one can resolve the structure selectively in one direction with the loss of 3D information. In using purified proteins, such as the study of kinesin microtubule interaction, the axial information can probably be sacrificed to gain the expanded 2D binding site information.

Finally, the 3D expanding gel also needs an update in many properties. The effects of varying monomer substances were well studied and applied in different ExM protocols. While the effects of thermal-resistant, absorption and polymerization conditions such as pH values and temperatures were not yet established in ExM. Besides, in ExM, the hydrogels were usually expanded in distilled water, whereas in tissue clearing techniques, refractive index-correcting solutions (with refractive index higher than 1.40) were used to immerse the gels, which also resulted in a maximum 2-fold expansion of the gels. Taken together, the combination of refractive index-correction and 7 - 25-fold expanded gels may result in a 3 - 10-fold expanded gel with higher refractive index but have not yet been established.

Conclusion

In this chapter, different ExM derivative protocols were presented and compared. We discussed the effects by different crosslinking reagent, different digestion, pre- and post-ExM immunostaining. By tuning these parameters, we established ExM at ~100 nm resolution and verified the homogenous expansion of ExM-treated microtubule cytoskeleton in cultured cells and spectrin ring structures in neurons. With the help of these two structures, we were able to calculate the distortion of our ExM experiments accurately down to tens of nanometers.

Chapter III Expansion stimulated depletion (ExSTED) microscopy

Scientific background

In comparison to conventional fluorescence microscopy, we hypothesized that the combination of ExM with one of the by now well-established super-resolution microscopy techniques such as STED microscopy or SIM could yield even higher resolution and answer one of the most important questions in the evaluation of this technique: if the expansion is indeed isotropic also at the nanometer scale. Since ExM is based on modifications of the sample, it can be used as an add-on to existing techniques without further adjustment on the setups.

In this chapter, an effort was made to establish a protocol for STED imaging of ExM-treated sample. Three cellular organelles (the centriole, the cilium and microtubules) were imaged with ExSTED, which were well-studied using electron microscopy and were also shown to have a defined diameter or distribution. These structures were also imaged with other super-resolution techniques such as SMLM or SIM, where the structures were proven to be robust against certain chemical fixation/ permeabilization treatments.

The aim was to resolve structures previously only accessible to electron microscopy or high quality SMLM microscopy, which would allow us to examine the isotropy of ExM in nanometer range.

ExM experiments were carried out independently. ExSTED and STED experiments were conducted in the Max-Plank-Institute of Molecular Cell Biology and Genetics with Dr. Alf Honigmann. Samples were prepared by me, and the imaging/ data analysis were performed together with Dr. Honigmann.

The result in this section is reproduced in part with permission from Mengfei Gao, Riccardo Maraspini, Oliver Beutel, Amin Zehtabian, Britta Eickholt, Alf Honigmann, and Helge Ewers. 2018. ‘Expansion Stimulated Emission Depletion Microscopy (ExSTED)’. *ACS Nano*. DOI: 10.1021/acsnano.8b00776.

ExSTED applied to identify CEP152 ring-like structure around the centriole

The centriole (Fig. 3.1 a) is a symmetric cylindrical structure presented in most eukaryotic cells, which plays important roles in ciliogenesis and cell division (Bettencourt-Dias and Glover 2007). One centriole is built of nine triplet microtubules and is ~200 nm in diameter and ~400 nm in length. In centrosome, a pair of centrioles, the mother and the daughter centriole, shows orthogonal orientation towards each other. Both centrioles are surrounded by dense protein matrix, the pericentriolar material. Regulated by these proteins, the two centrioles duplicate precisely per cell cycle during mitosis (Holland, Lan, and Cleveland 2010).

We chose CEP152 as a marker in the experiment, which distributes in ring-like structure around the circumference of a centriole. In the past, immuno-electron microscopy (Sonnen et al. 2013) and SIM (Lawo et al. 2012; Park et al. 2014) experiments have shown that CEP152 signals are confined to the proximal halves of mother centrioles, also at the interface between mother and growing daughter centriole (Sonnen 2012), with an ring diameter of 300 - 400 nm in mammalian cells.

In the experiment, African green monkey kidney fibroblast (CV-1) cells were cultured on coverslips, fixed with cold methanol and immunostained against CEP152. The sample were imaged with spinning disk confocal microscopy pre- and post-ExM.

Only after ExM treatment, the ring like structure of CEP152 can be resolved with confocal microscopy. In the pre-ExM sample, CEP152 was identified as a single bright dot (Fig. 3.1 b) near the aster formed by microtubules or a pair of dots at the poles of a bipolar spindle. After expansion, the CEP152 were more than 15 µm away from the coverslip and the mother centriole was identified as a ring with optimal signal to noise ratio (Fig. 3.1 c). Most of the CEP152 rings were captured as single ring ~300 nm, whereas some appeared as a pair of duplicating ring structure, with one brighter ring and another different orientated structure. The complete ring structures were cropped and averaged for calculation of an average diameter of 325.3 ± 35.9 nm. Deconvolution was later applied to single image-series but did not further increase the resolution to

reveal sub-structures in the centriole.

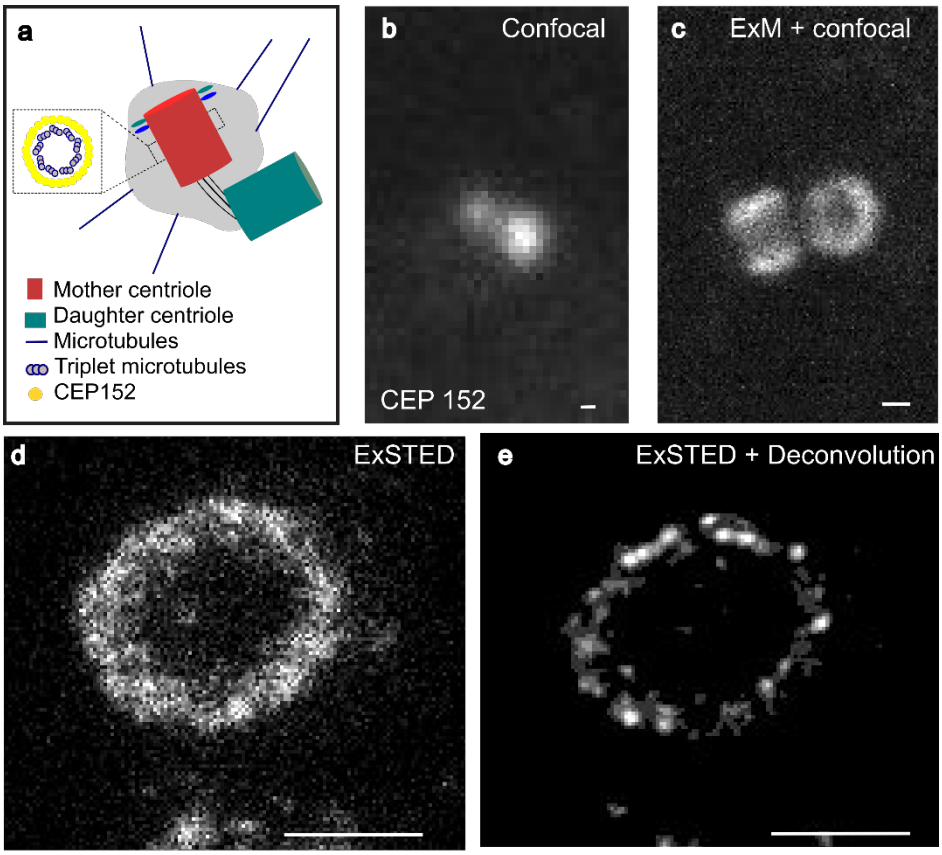

Figure 3.1 ExSTED of the centrioles. (a) Model of a pair of mother (red) and daughter centriole (green). The centriole consists of nine triplet microtubules and is surrounded by a protein matrix, the pericentriolar material (gray). CEP152 forms a ring-like structure outside the centriole. (b) Confocal image of two centriole in a CV-1 cell. (c) Confocal image of two expanded centrioles in CEP152 immunostained CV-1 cell, the mother centriole was clearly presented as a ring structure. (d) ExSTED of CEP152 immunostained cells. (e) Deconvoluted image of ExSTED CEP152 immunostained cell. All scale bars 200 nm.

Finally, the gels were imaged with STED microscopy using a water-immersion objective and a 3D STED laser. With the STED depletion laser and deconvolution, we

observed the centriole with 298.9 ± 19.5 nm in diameter (Fig. 3.1 d - e). The signal to noise ratio was not sufficient for finer identification of the sub-structures within the centriole. Low labelling density of the CEP152 was the main reason. As a replacement, we chose another organelle with similar symmetric structure but more abundant targeting protein, the primary cilium.

ExSTED applied to resolve 9-fold microtubule doublets in the primary cilium

The cilium is also a confined rootlet-like structure, assembled from nine doublet microtubules (Fig. 3.2 c - d) (Seeley and Nachury 2010). It is an organelle found on all eukaryotic cells and typically serves as a sensory organelle or provides motility (Reiter and Leroux 2017; Seeley and Nachury 2010; Singla and Reiter 2006). The inner-structure of the primary cilium has been resolved using electron microscopy (Rhodin and Dalhamn 1956), whereas super-resolution techniques are mainly applied to study the morphology, i.e. the heterogeneity of membrane shape of the cilium (Tony Yang et al. 2015; Yang, Chong, and Liao 2016; Yoon et al. 2019). By applying ExSTED on cilia, we aimed to resolve the nine microtubule doublet structures in the cross-sections of cilia.

In this experiment, we first tested the primary cilium in retinal pigmented epithelial (RPE) and Madin-Darby canine kidney (MDCK) (Kukic, Rivera-Molina, and Toomre 2016; Mirvis, Stearns, and James Nelson 2018; Ott and Lippincott-Schwartz 2012) cells, where usually one cilium occurs per cell. The cells were serum-starved to grow cilia and imaged with confocal microscopy to check if the labelling and orientation of the cilia would be appropriate for STED microscopy.

Both RPE and MDCK cells were first cultured on coverslips until they reached approximately 90 % confluency. Then the coverslips were changed to spare wells containing low serum (0.5 % fetal bovine serum) growth medium and starved for 3 to 14 days. The cells were carefully washed with PBS and fixed using PFA. After quenching and blocking, a trick was performed by quickly rubbing another coverslip over the sample, which helped the perpendicularly growing cilia to fall down to the top

of the cell layer. In this way, cilia showed two orientations, perpendicular and parallel to the coverslip surface and allowed us to track both the cross-section and profile of the cilia. Anti-α-tubulin antibody or anti-acetylated-tubulin antibody and Abberior Star Red-labelled secondary antibodies were used to immunostain the cilia. The cells were first imaged with spinning disk confocal microscopy (Fig. 3.2 a, b).

We observed expanded cilia in both samples. The protrusion location (in Z direction) was estimated by counting Z-stacks from the surface to the root of the cilia. RPE cells were averaged to be 8.2 ± 4.2 µm and MDCK cells were 11.4 ± 6 µm thick. Nevertheless, RPE cells were less compacted as MDCK cells with the same starvation time and with only some patches of cells growing cilia.

The length of cilia was estimated only in 2D by taking maximum projections of isolated cilia and tracking manually. RPE cilia were on average 6.3 ± 2.8 µm in pre-ExM samples, 5.2 ± 2.3 µm in post-ExM samples, while MDCK cilia were on average 12.6 ± 3.9 µm in pre-ExM samples and 11.8 ± 4.6 µm after expansion.

Although RPE cilia were closer to the coverslip surface, these shorter cilia cannot bend much and lay on the top of the cells as the MDCK cilia. Thus, we continued in the ExSTED experiments using one-week starved MDCK cells. The upper tip of the cilium could reach up to 50 µm from the surface of the coverslip after expansion, so we used a water-immersion objective in the experiments to eliminate refractive index mismatching induced aberration.

In the ExSTED experiments, the MDCK cilium was labelled using anti-α-tubulin antibody plus Abberior Star Red secondary antibody, and an anti-ARL13B (a membrane associated GTPase) antibody plus the STED imaging compatible dye Alexa Fluor® 594 conjugated secondary antibody. In the cross-section view, not only the dual color staining was successfully established, but also the detailed microtubule doublets resolved (Fig. 3.2 e - g). However, the ‘9 + 0’ system cannot be quantified in the profile image along the cilium, probably because of the mass of microtubule antibody labelling and the poorer resolution with a water-immersion objective.

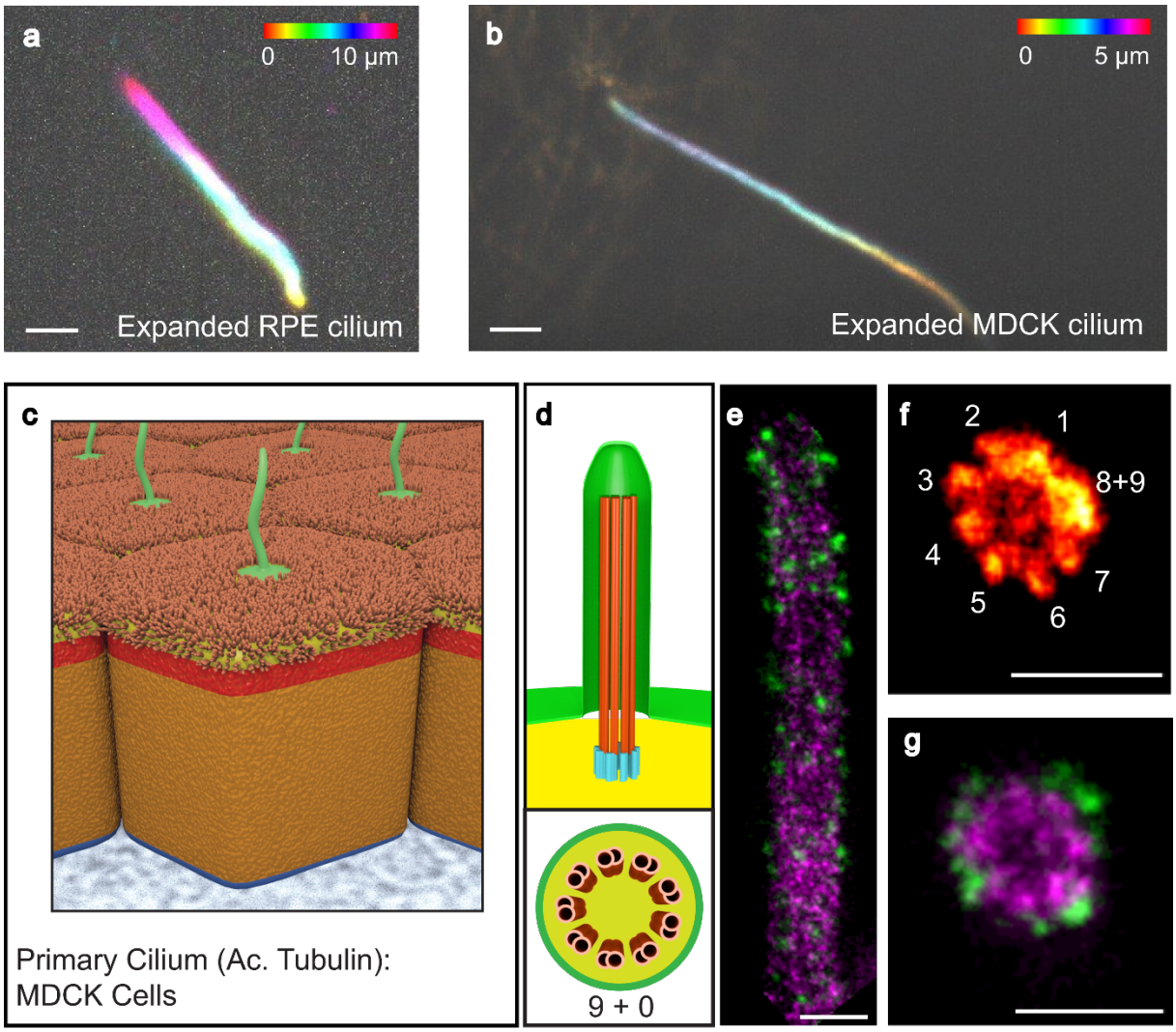

Figure 3.2 ExSTED of the primary cilia. (a) Expanded RPE cell immunostained against acetylated (ac.) tubulin imaged with spinning disk confocal microscopy. (b) Expanded MDCK cell immunostained against acetylated (ac.) tubulin was imaged with spinning disk confocal microscopy. Both images were maximum projected in Z direction into a single plane with color maps indicating depth. (c) Model of mammalian epithelial MDCK cells with primary cilia at the apical side. (d) Model of the primary cilium showing the nine doublet microtubule structures, with ac. tubulin in orange and the cilia membrane protein Arl13b in green. Lower panel shows a model of the cross section through the cilium. (e) Two-color ExSTED on ac. tubulin (magenta) and Arl13b (green) shows a cilium cut on the long axis. (f) Single color image of ac. tubulin in cross-section view. (g) Two color images as in (e) in cross-section view. Scale bars are 1 µm in (a, b), 200 nm in (e - g).

In brief, with abundant tubulin staining in cilium, we achieved relatively high labelling density, but the final resolution was greatly limited by the over 40 μm axial imaging distance and the 1.2 NA water-immersion objective. It failed in identifying single doublets in the longitudinal view along the cilium. Thus, we turned back to a simpler biological structure, microtubules, and put effort in the optimization of signal retention after expansion.

ExSTED applied to achieve ultra-resolution microtubules

Microtubules is one of the cytoskeleton filaments. One microtubule usually consists of 13 protofilaments (Díaz et al. 1998; Tilney et al. 1973), polymerized by dimers of globular protein, α- and β-tubulins (Nogales, Wolf, and Downing 1998). Microtubules are usually observed as long, dynamic filamentous structures (Howard and Hyman 2007). Only when using electron microscopy, the hollow tube structure of the microtubule with an outer diameter of 24 nm and an inner diameter of 12 nm (Löwe et al. 2001; Mandelkow, Mandelkow, and Milligan 1991) can be resolved. Microtubule can also be densely labelled via immunofluorescence and other small probes, e.g. paclitaxel (Schiff, Fant and Horwitz 1979) or 4',6-Diamidino-2-phenylindole (Bonnes et al. 1985), hence it is also commonly used as a benchmark target for the super-resolution techniques (Jimenez, Friedl, and Leterrier 2019; Lukinavičius et al. 2014). Here we aim to achieve sub-microtubule resolution, where the protofilaments or tubulins can be revealed.

To resolve microtubules with ExSTED, we first improved the immuno-fluorescence labelling density. In the cilium experiments, we were able to resolve the “9+0” structure via doublet microtubule labelling, where the labelling was enhanced due to the larger surface of the epitopes. We adapted a similar strategy in the microtubule labelling.

As shown in the last chapter, immuno-fluorescence labelling against GFP can improve the signal intensity after expansion. Here we extended the labelling degree by a combination of over-expression of tubulin-GFP, a cocktail of anti-GFP, anti-α-tubulin, and anti-β-tubulin antibodies and a dye-conjugated secondary antibody against all

primary antibodies conjugated with the same dye. With the optimized labelling method, we aimed to resolve the sub-structure of microtubules and the entire microtubule cytoskeleton in cultured cells.

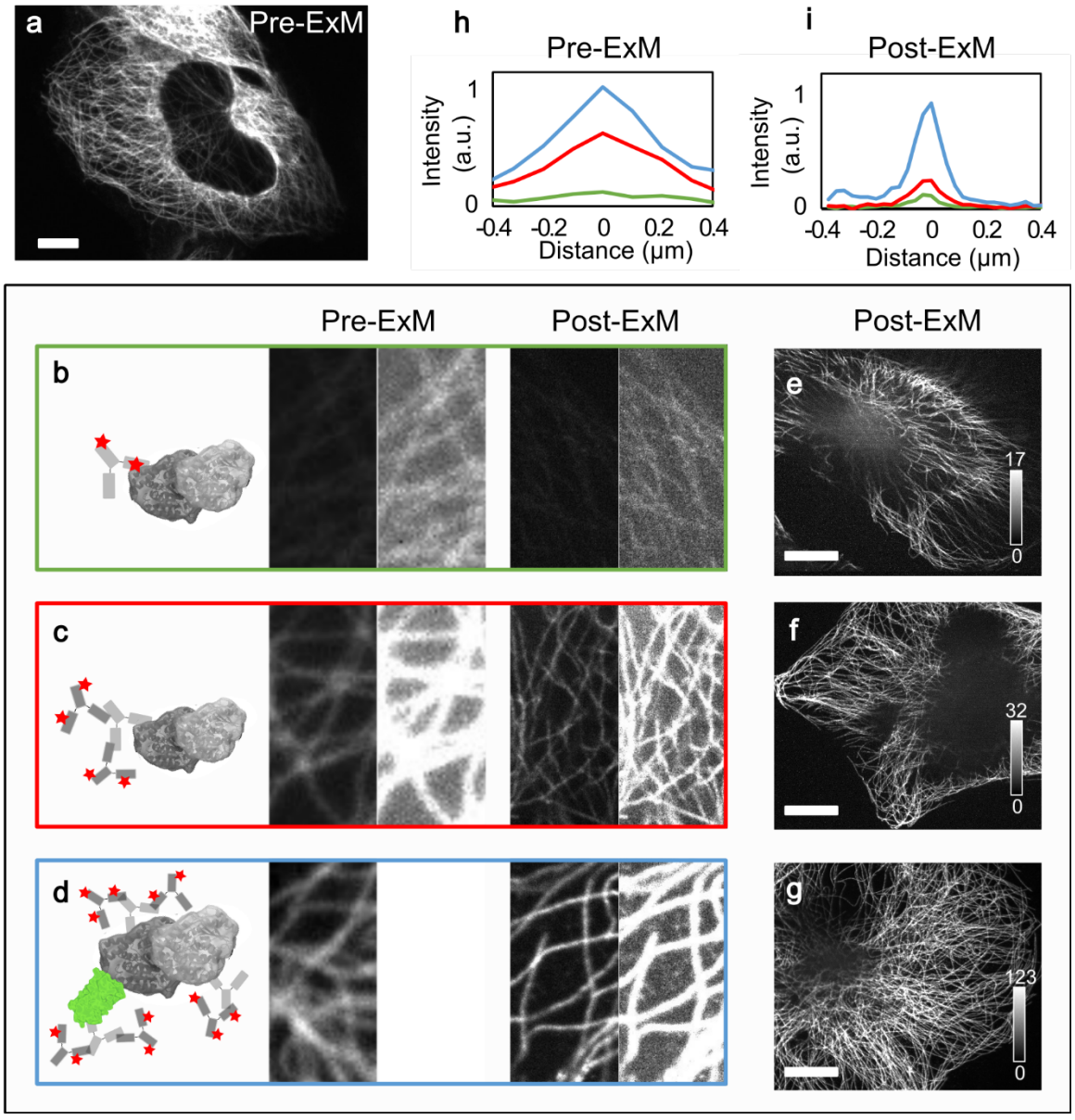

Figure 3.3: Improved labelling of microtubules for ExM. (a) HeLa cells were immunostained with anti-α-tubulin antibody. (b – d) HeLa cells immunostained by different protocols and imaged before and after the ExM treatment. Shown are fluorescence micrographs with two different intensity scaling (left and right, scaling identical from (b – d)) to emphasize the relative intensity. (b) HeLa cells were immunostained with an Alexa Fluor® 488 labelled anti-α-tubulin antibody. (c) HeLa cells

were immunostained with anti-α-tubulin antibody and an Alexa Fluor® 488 labelled secondary antibody. (d) α-tubulin-GFP-expressed HeLa cells were immunostained with anti-α-tubulin, anti-β-tubulin and anti-GFP antibodies and Alexa Fluor® 488 labelled secondary antibody. (h, i) Line scans across microtubules before (h) and after (i) expansion using protocol (b, blue), (c, red) or (d, green). (e - g) Maximum projection of 3D fluorescence micrographs with different intensity scaling, demonstrating a ~4-fold increase of signal using the multi-epitope labelling shown in (b - d). All images were taken with spinning disk confocal microscopy. Scale bar 4 µm in (a, e - g) and the sizes of the figures in (b - d) 4.32 µm x 8.64 µm.

The enhancement of the signal greatly depended on the competitive binding between primary antibodies, thus the contribution of single antibody was partially measured by direct labelling of the primary antibody with different fluorescent dyes. In the confocal imaging experiments, Alexa Fluor® 488 was used for the universal staining with the GFP signal also being partially persevered and visible in the same channel, whereas in the STED imaging, Abberior Star Red, the far-red dye, was used instead.

By this GFP and antibody combined staining, the microtubule cytoskeleton showed an increase of signal by more than 10-fold in the pre-ExM coverslips and ~ 4-fold in the post-ExM samples by comparing the intensively labelled microtubule to only primary antibody-labelled microtubule (Fig. 3.3). The intensively labelled cells were imaged before and after expansion using 500 ms exposure time and the maximum laser power (491 nm, Coherent, 100 mW) with spinning disk confocal microscopy. Z scanning was taken through the expanded cell and repeated 10 times, and the illuminated region was greatly bleached. However, with adjusted brightness and contrast, continuous microtubule structures were observed in the bleached area (Fig. 3.4). The fluorescent samples were also continuously being illuminated on the microscope for minutes at single Z position, and complete microtubule structures were still resolvable (Fig. 3.5).

The expanded sample was then proven to be sufficient for the ultra-high laser power in STED imaging.

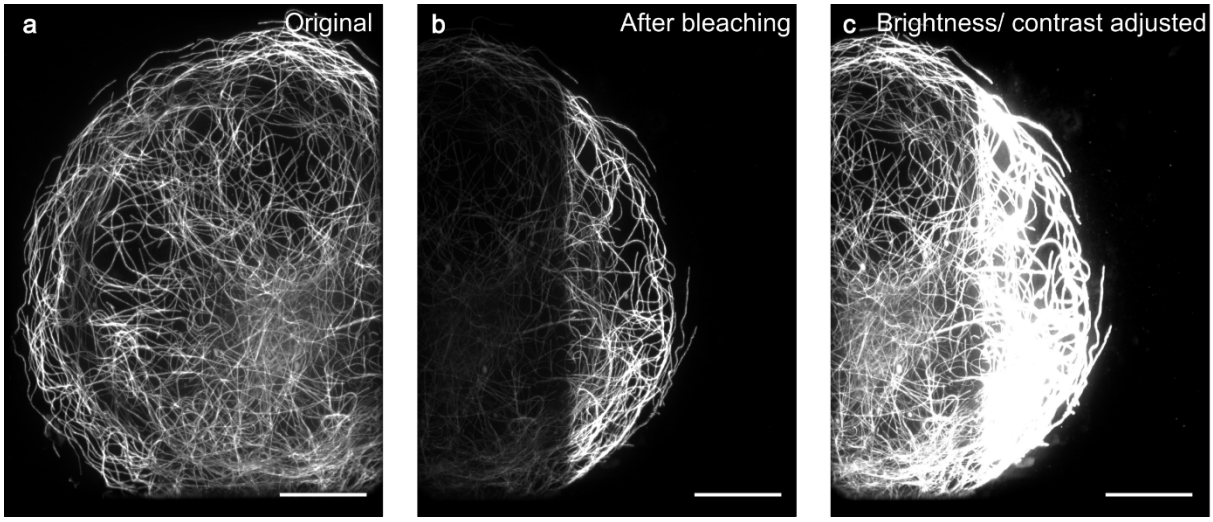

Figure 3.4 Intensively labelled microtubules. (a - c) Expanded HeLa cell overexpressed tubulin-GFP and intensively labelled using anti-α-tubulin, anti-β-tubulin and anti-GFP antibodies, respectively, together with a secondary antibody conjugated to Alexa Fluor® 488. The sample was imaged on a confocal microscope. The field of view in (a) was bleached by taking stacks through the entire cell at 0.5 µm sectioning on the spinning disk confocal microscope with the 491 nm laser beam (Coherent, 100 mW) at full power for 10 times with 500 ms exposure time. Afterwards, the field of view was moved to contain an unbleached part of the sample. (b) and (c) are intensity-scaled for the non-bleached part or the bleached part respectively, to allow the reader to appreciate the extent of photo-bleached and remaining signal. Scale bar 10 µm.

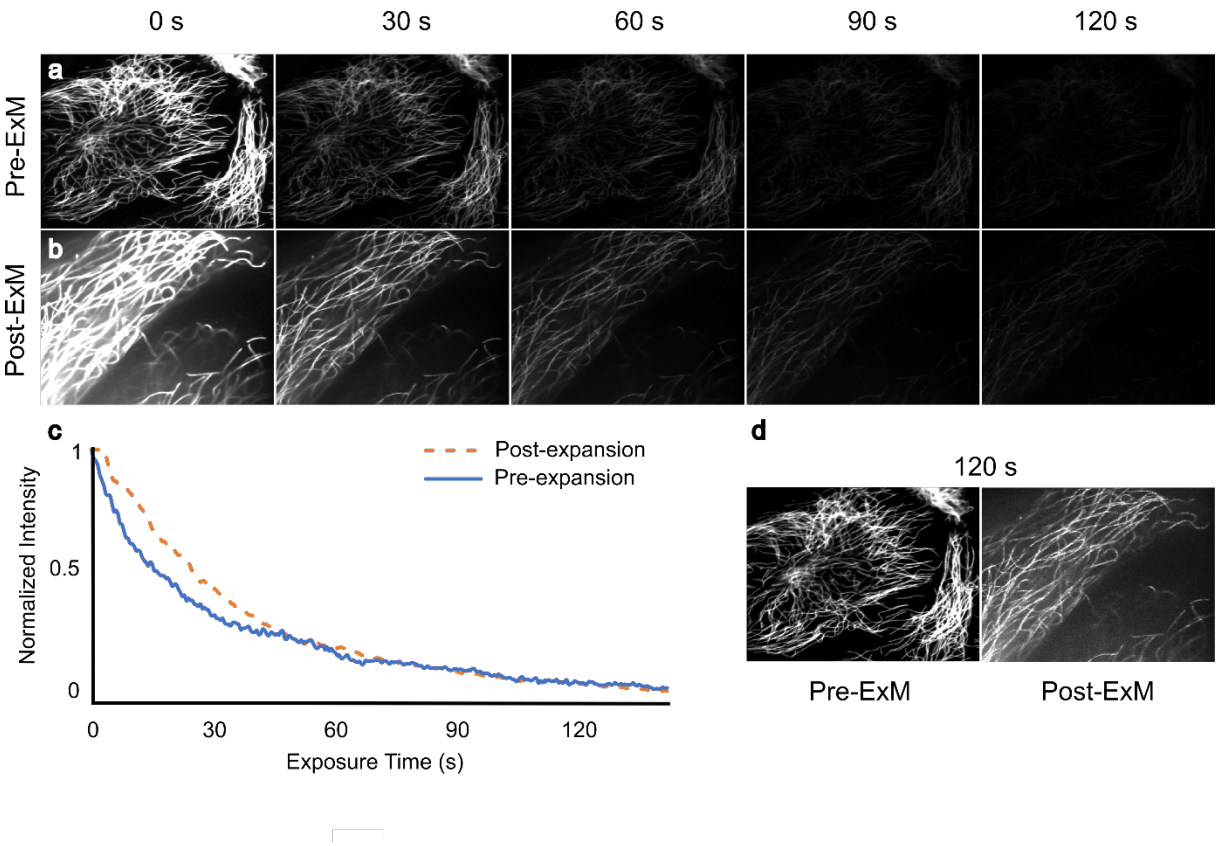

Figure 3.5 Photo-bleaching of the intensively labelled microtubules. (a) Intensively labelled fixed HeLa cells were imaged on the microscope with 500 ms exposure time and 100 mW 491 laser. (b) Another intensively labelled sample were proceeded with ExM and the expanded gel was imaged with the same microscope settings. Shown were 0, 30, 60, 90, 120 s of exposure. A single microtubule was taken from each sample and the intensity decay was plotted in (c). The bleaching speed of post-ExM samples was slightly faster than pre-ExM in the first minute but without obvious difference after 60 s. (d) Bleached pre- and post-ExM sample after 120 s of exposure with brightness/ contrast adjusted.

Isolated microtubules at the bottom of the cells with straight outward extension was chosen for the first model. Different laser power and camera settings were tested in the experiment to pursue the best resolution without great signal loss. We observed the pair of parallelly aligned substructure in the continuous microtubule with 38.6 ± 11.9

nm peak to peak separation, comparable to the diameter of immunostained microtubules imaged using SMLM (Auer et al. 2018; Olivier et al. 2013). The effective resolution of the expanded microtubules was measured using a 1D Gaussian line scan through the microtubule and a 2D Gaussian for an isolated single spot. Both approaches gave a resolution in XY of 8 ± 1.4 nm (Fig. 3.6 a - b).

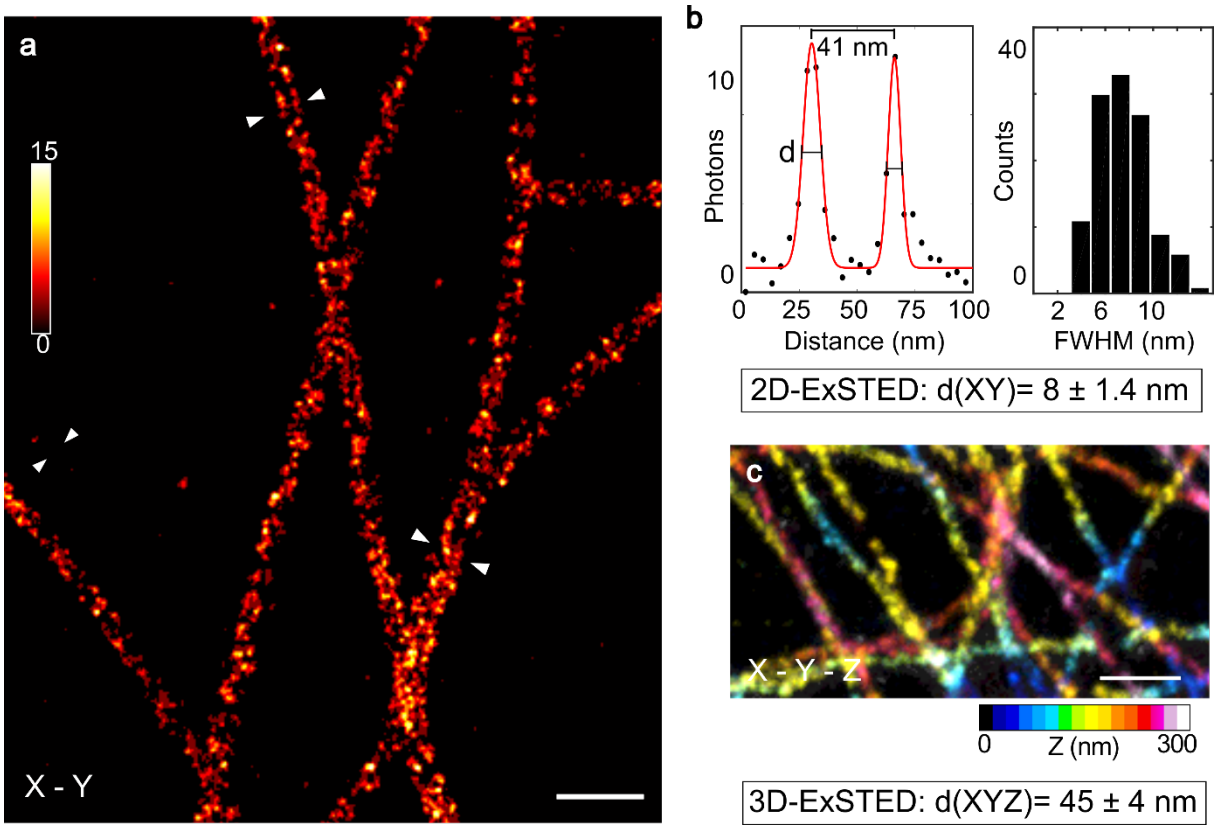

Figure 3.6 2D ExSTED of microtubules imaged with high-NA objectives. (a) 2D STED of expanded tubulin staining using an 100x oil immersion lens imaging closing to the cover glass surface. Note that the resolution allows to clearly distinguish antibodies on opposite sides of a single tubuli. (b) Left panel: Quantification of the apparent diameter of microtubules including primary and secondary antibodies. Right panel: Quantification of the 2D resolution in (a). (c) 3D STED of expanded immunostained tubulin using an oil-immersion objective near the surface. The Z position is indicated by the color coding. Scale bar is 100 nm in (b) 100 nm in (c).

To investigate the magnified volumetric imaging, we imaged the microtubules closing to the coverslip surface using the 3D mode in STED microscopy, and the 3D STED laser was calibrated for an oil-immersion objective. Although the hollow shape of the microtubules was not resolved, these microtubules gave an isotropic FWHM of ~ 45 ± 4 nm, compared to the measured 3D STED resolution of ~ 100 nm (Fig. 3.6 c). Unfortunately, the resolution decayed fast when imaging deep inside the hydrogels limiting volumetric imaging greatly.

To overcome the refractive index mismatching-induced aberration, a water-immersion objective was recalibrated for the system and used for the whole-cytoskeleton imaging. The stability of the gel challenged the quality of the 3D image. Firstly, the gel drifted. This was reduced by placing it on a poly-L-lysine-coated surface, which strongly inhibited lateral sliding of the gel. Cross-correlation was also used in image analysis to correct for the drift. Secondly, the gel shrank in 3D during the hours long imaging due to evaporation. This problem was overcome by carefully sealing the gel in an imaging chamber using two-component silicon glue. After these optimizations, we were able to perform an 8-hour long 3D STED imaging with a water-immersion objective, and yielded a complete microtubule cytoskeleton with excellent signal to noise ratio and isotropic resolution of 70 nm even in the compact area near the nucleus (Fig. 3.7 a - c).

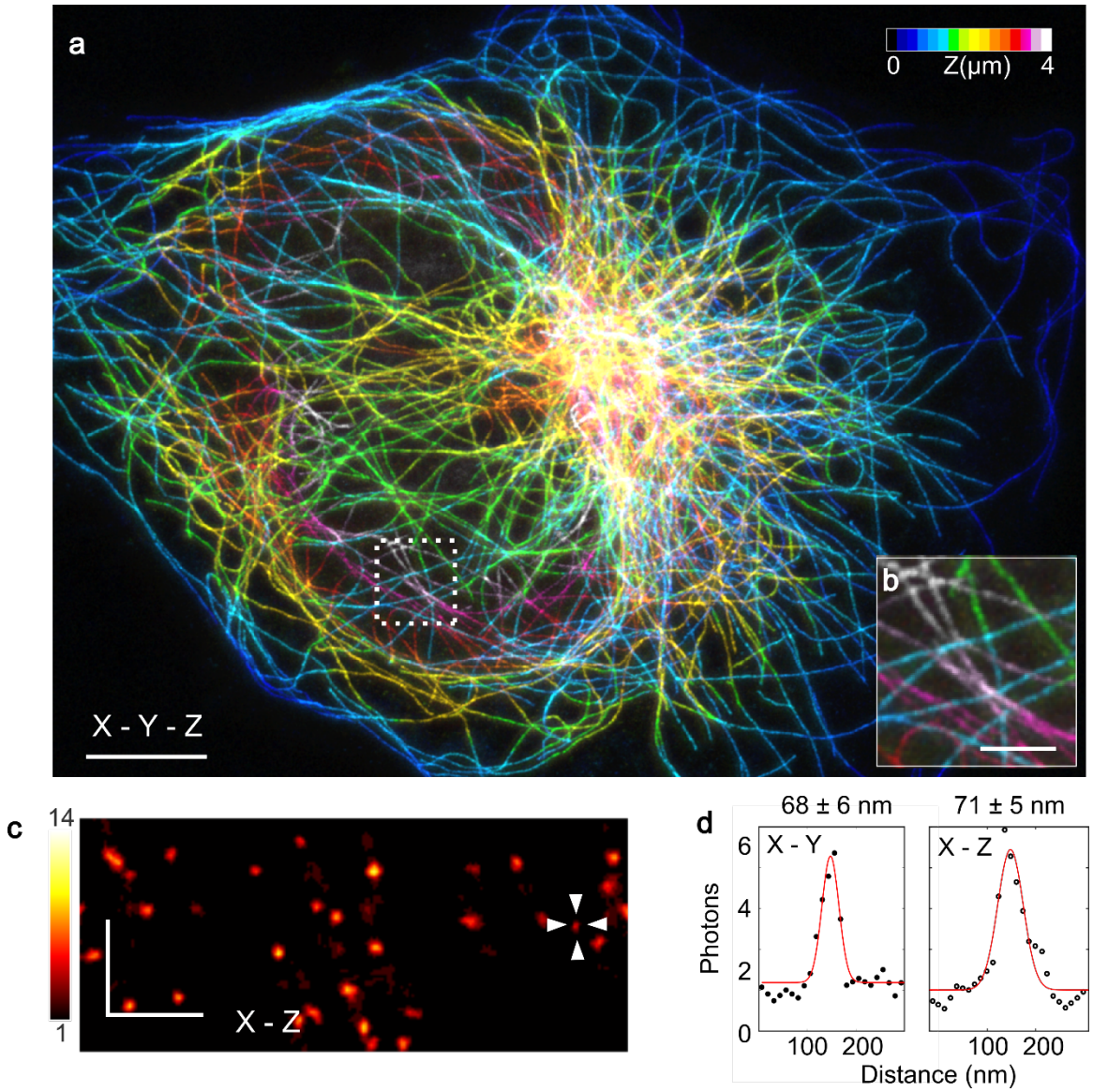

Figure 3.7 3D ExSTED of microtubule cytoskeleton with a water objective. (a) Whole cell 3D ExSTED using a 60x water immersion objective to enable greater depth penetration. (b) Close up of a dense region in 3D. (c) XZ cross-section of from (a), note the isotropic shape of the PSF. (d) Exemplary XY and Z profiles indicated an isotropic resolution of ~ 70 nm. Scale bar is 4 µm in (a) and 1 µm in (b, c).

Discussion

Here three different systems were imaged with ExSTED, 1) an isolated structure with limited labelling; 2) an abundant system with high-density labelling; 3) an isolated structure with high-density labelling. In all three samples, the enhanced resolution was less than direct resolution calculated by dividing the STED imaging resolution with the expansion factor, which should be 5 nm in 2D and 18 nm in 3D mode. The 2D resolution was slightly limited from the bleaching or insufficient immunostaining of the sample, and greatly affected by optical aberration when focusing into the gel. To overcome the mismatching of refractive index between hydrogel (n=1.33) and immersion oil (n=1.42), a low NA water-immersion objective was used, which contributed to the reduced resolution in 2D or 3D mode.

2D ExSTED achieved super-resolution more than 10-fold faster comparing to SMLM. Besides, the fast scanning mode of STED microscopy restricted the local drift to a negligible level. Conversely, 3D ExSTED took 64-fold of the STED/ confocal imaging with spontaneous shrinking and lateral sliding from the hydrogel. In comparison to SIM, which can achieve 100 nm resolution in 3D with a non-expanded sample in short time period, 3D ExSTED showed a low cost-effective performance. Further improvements, from the STED microscopy side such as DyMIN (Heine et al. 2017) or STED microscopy with adaptive optics units (Patton et al. 2016), however, may help to increase the resolution and shorten the acquisition time.

The other limitations in the ExSTED imaging are the signal density on the targets and the relevant distance between probe and targets. At the sub-10 nm resolution, the approximately 7.5 nm long primary and secondary antibody pair may not be appropriate for precise nanoscale imaging. Smaller probes such as the SNAP- (Keppler et al. 2003) or Halo-tag (Los et al. 2008), nanobodies (Mikhaylova et al. 2015; Ries et al. 2012) and affimers (Opazo et al. 2012; Tiede et al. 2014) may be used for more specific delivery of the fluorescent probes, however without the multi-conjugation of dyes on antibodies, a decrease in the local labelling density remains a challenge.

Conclusion

In this chapter, 2D and 3D ExSTED study of CEP152, primary cilium and microtubule were established. The result confirmed the improvement of STED microscopy by combining it with ExM, and up to 30-fold increase in resolution compared to conventional microscopy. Besides that, the labelling was optimized by overexpression and a cocktail of different antibodies, which was robust in the ExSTED imaging. Via this labelling strategy, we were able to resolve sub-10 nm structure in 2D and sub-50 nm in 3D. The optimized mounting of gels also allowed the sub-100 nm 3D imaging of an intact expanded microtubule cytoskeleton.

Chapter IV ExM in combination with other super-resolution techniques or smaller probes

Expansion structured illumination microscopy (ExSIM)

As described in the last chapter, ExSTED can easily enhance the resolution in 2D at lower temporal cost, however the strength by this combination was weakened in hours-long 3D whole-sample imaging. Here we hypothesized that the fast-optical sectioning in 3D SIM would allow a more efficiently enhanced resolution of the expanded sample, however the experiment was limited by technique obstacles.

In the SIM experiment, HeLa cells were extensively labelled with antibodies against tubulin as described in the ExSTED-microtubule experiment. The gel was prepared using both ExM and MAP protocol, where the cells were first imaged on spinning disk confocal microscopy. Similar to the high demand of intensive labelling in STED microscopy, 3D SIM microscopy requires 15 exposures per focal plane. During the acquisition, a faster scanning, or shorter exposure time, was required to ensure less photo-bleaching. Thus, the intensive fluorescence labelling was also prepared in the SIM experiment.

With the GE OMX SIM setup, coverslips with non-expanded coverslips and expanded gels were imaged first on a deconvolution microscopy with 3 x 3 or 5 x 5 fields of view, in which the targeted cells were selected and recorded in the system. Then the sample was transferred to another identical microscope with SIM unit, and the saved locations of the cells were used to find the samples. Both setups were calibrated with 100-nm beads shortly before the imaging. Unfortunately, the set up cannot be calibrated for water immersion objective, instead 60x 1.42 NA oil-immersion objective was used. The mismatching of refractive index limited the imaging section to less than 15 µm from the surface.

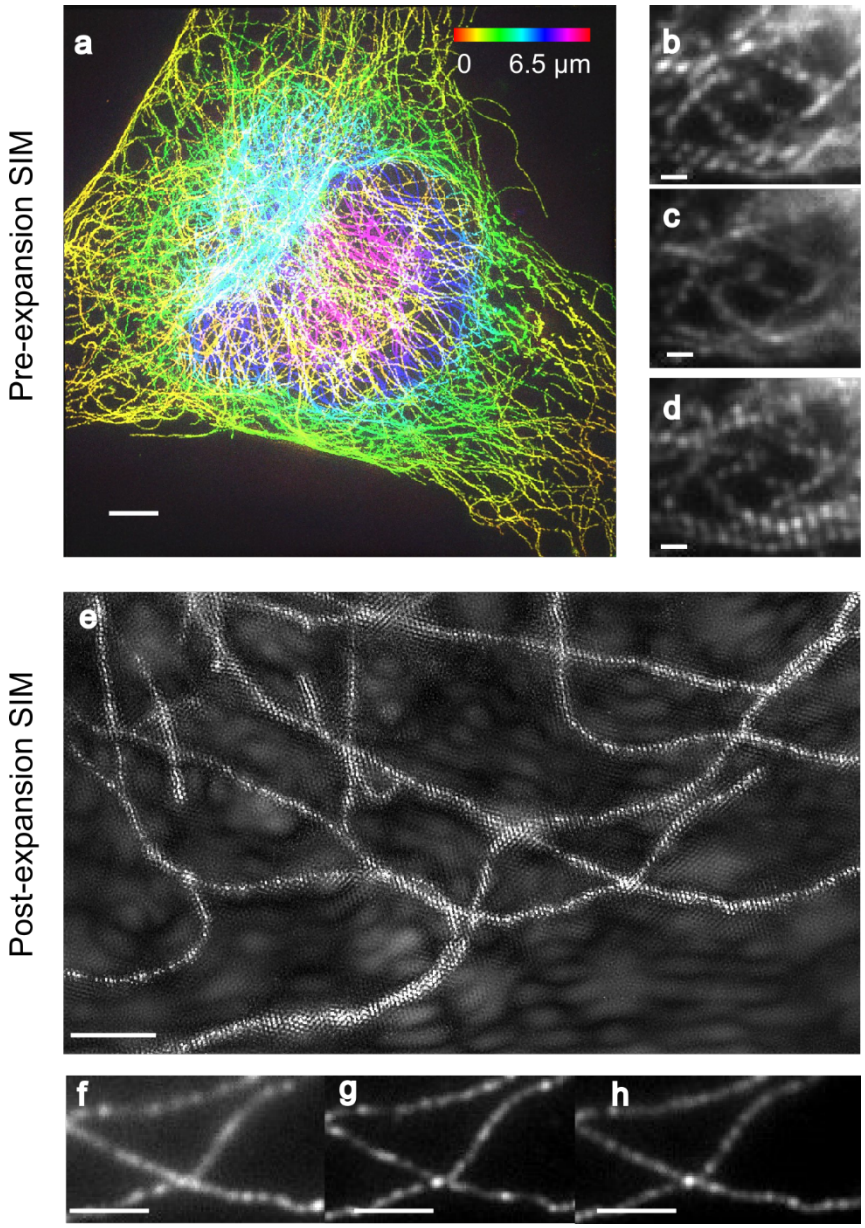

Figure 4.1 Combination of ExM with SIM. (a) 3D SIM of non-expanded HeLa cell with tubulin immunostained. Z depth shown in colormap. (b - d) Structured illumination patterns during the three rounds of imaging. (e) 3D SIM of an expanded HeLa cell with tubulin immunostained. (f - h) Diffraction patterns appeared during the three rounds of imaging. No clear patterns observed during the imaging and sample bleached fast after 900 frames of scanning. Scale bars are 1 μm.

In the pre-ExM sample, the microtubule cytoskeleton was easily captured and quickly scanned, with a resolution of ~ 120 nm (Fig. 4.1 a - d). However, in the post-expansion sample, structured illumination seemed to lose its power. In comparison to the patterns in the cultured cells, where stripes were straight, easily identified and all over the field of view, the stripes in the expanded sample were hard to locate and the orientations varied even in one scanning mode (Fig. 4.1 e - h). We tried to run the SIM algorithm for image reconstruction, however, severely compromised result was established. The resolution of microtubules was not enhanced, a patterned noisy background was present, and an extraordinarily fast photo-bleaching was also observed in the sample (Fig. 4.1 e - h). As a result, with the ‘ghost’ patterns, we were not able to isolate microtubule structures from the background and did not observe an improvement in resolution without strong artifacts.

ExM with smaller probes

Most of the ExM experiments were based on either fluorescent protein expression or immuno-fluorescence labelling. The former provides only limit photon emission after expansion, while the latter showed 10 – 20 nm of linkage error, which represents the distance from fluorophores on the antibody to the real position of the antigen. To minimize the linkage error with relatively higher signal than directly using fluorescent protein, we chose several small probes that are either smaller in size such as nanobody (2 nm long) or tags that can be specifically labelled like SNAP-tag.

Experiments were first conducted using nanobodies, where cells were first fixed and stained with anti-tubulin nanobody and proceeded with ExM. As a result, majority of the anti-tubulin nanobody signals were lost after digestion while anti-tubulin nanobody was detectable but sparse. Big clusters of signals were also observed after ExM using nanobodies (Fig. 4.2 a - b). Post-staining was also performed (Fig. 4.2 c - d), where the clusters were still visible and the signal to noise ratio was not sufficient to isolate the microtubule structures. Both experiments were repeated for a few times, however, the clusters were always severe. And only with freshly prepared nanobodies can some continuous microtubules being observed. With longer storage time, the nanobodies

were more observed as big clusters after ExM. We concluded that the most widely used anti-tubulin nanobody (Mikhaylova et al. 2015) dissociated from the epitopes during the protease or SDS incubation.

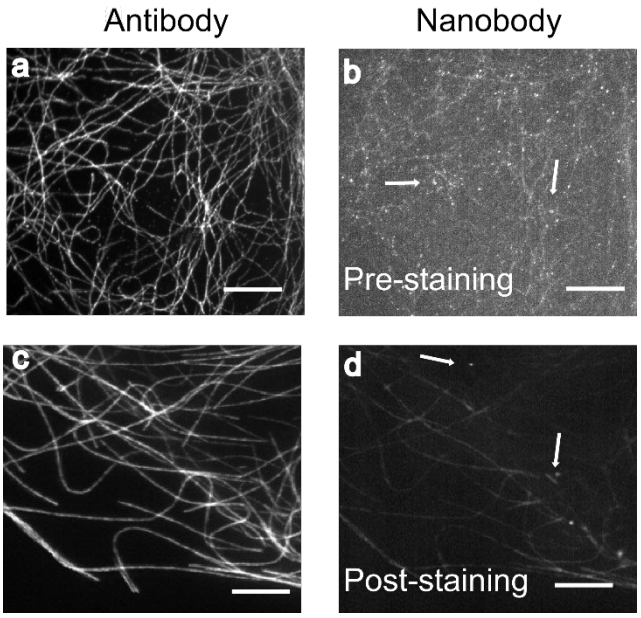

Figure 4.2 Applying nanobody in ExM. (a, c) HeLa cells were fixed and immunostained using anti-tubulin-antibody. (b)The sample was costained using anti-tubulin nanobody. Nanobody signals were observed in pre-staining sample, but highly clustered (white arrows) and the labelling along microtubules was very low. (d) Another hydrogel was prepared directly from the tubulin-immunostained HeLa cells using antibodies and anti-tubulin-nanobody was applied to stain the digested and washed gel. In the post-expansion sample, the nanobodies clustered less, whereas the labelling density along the microtubules was also very low. Scale bars are 2 µm.

Direct labelling of SNAP tag via crosslinkable benzyl-guanine (BG) structures

Thus, we changed to the SNAP-tag, a 19.4 kDa enzyme based self-labelling protein that can be specifically and covalently tagged with benzyl-guanine (BG) carrying a dye (Juillerat et al. 2003; Keppler et al. 2003; Sun et al. 2011). SNAP-tag is genomic coded together with the targeted protein and expressed in cells, while BG-dye can be used

to stain the SNAP tag in live or fixed cells, depending on the polarity of the dye. To use the SNAP-tag in ExM, several crosslinking mechanism can be applied, 1) As a conserved protein, AcX- or MA-NHS-crosslinked SNAP-tag may be also resistant to proteinase K digestion. By pre-staining SNAP with BG-dye, the signals of the dye might be preserved in the gel after ExM-treatment. 2) BG-dye can be modified into a crosslinker form, BG-dye-aa, where aa represents the acrylic or methacrylic acid moiety on the dye. Since BG is not influenced by proteinase K, the tri-functional dye is expected to be crosslinked into the gel via the aa group and retained fluorescent even after expansion. 3) BG-dye can also be modified into aa-BG-dye form, where the acrylic group binds to the BG. However, modification on the benzyl ring has been shown to inhibit SNAP-BG binding kinetics (Sun et al. 2011). By the end, the combination of 1) and 2) are expected to be used to preserve SNAP-BG-dye.

SNAP-tag preserved from protease digestion

MA-NHS-crosslinked SNAP-tag was imaged using ExM. NUP96-SNAP clustered regularly interspaced short palindromic repeats (CRISPR) -edited human bone osteosarcoma epithelial U2OS cell line was given by Dr. Jonas Ries from EMBL as a gift and the specificity of the SNAP-tagged nuclear pore constructs were examined via other super-resolution techniques (Schlichthaerle et al. 2019; Thevathasan et al. 2019). A control experiment was first performed using SNAP-Surface 647 and *d*STORM (Fig. 4.3). Different fixation, blocking and staining conditions were tested and optimized to achieve a nuclear pore ring structure with ~ 100 nm in diameter.

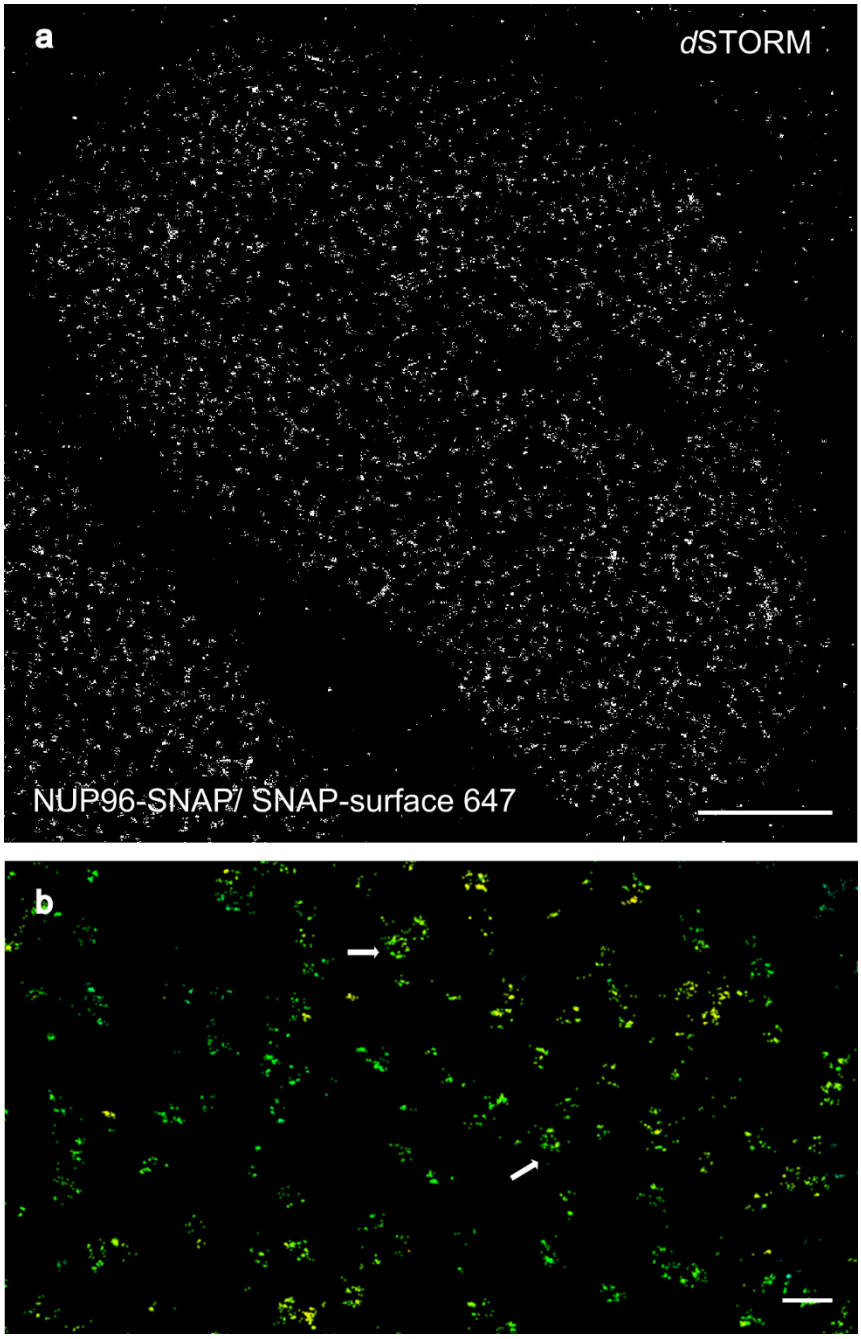

Figure 4.3 NUP96-SNAP-expressed U2OS cells imaged with *d*STORM using SNAP-surface 647. (a) U2OS cells were fixed using the SNAP-tag fixation protocol and stained with SNAP-surface 647. The sample was imaged with Vutara 352 SMLM. (b) Magnified NUP structures, where the white arrows were pointed to the rings of nuclear pore complexes. Scale bars are 3 μm in (a) and 300 nm in (b).

Then the optimized protocol was applied to the NUP96-SNAP cells with Janelia Fluor 646 or NUP153-GFP cells with GFP immunostaining. Both samples were imaged on spinning disk confocal microscopy and proceeded for ExM (Fig 4.4).

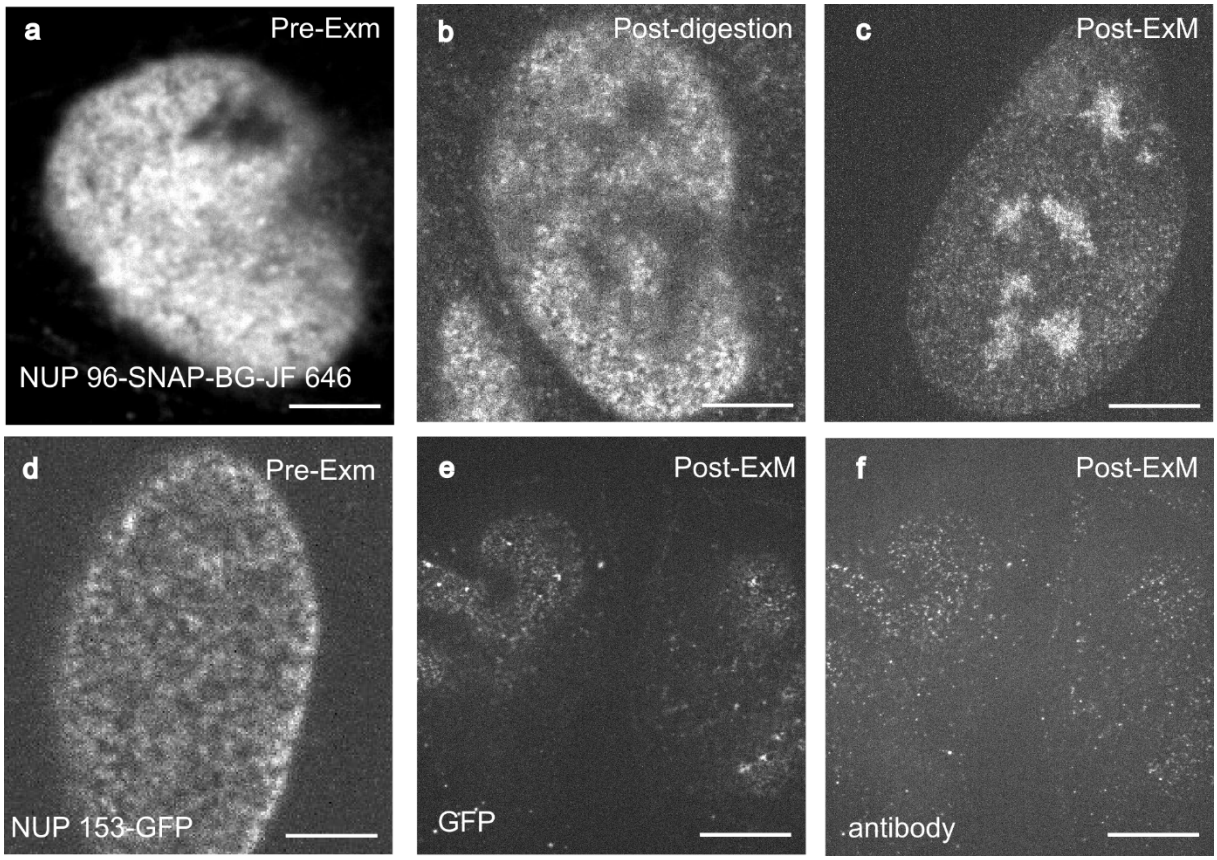

Figure 4.4 Nuclear pore complex imaged using ExM via SNAP-BG or GFP-antibody. NUP96-SNAP-expressed U2OS cell line was first cultured, fixed and stained with BG-Janelia Fluor 646. The sample was imaged with (a) spinning disk confocal microscopy and proceeded for ExM using mild digestion. (b) Digested and (c) expanded sample were imaged again using confocal microcopy. NUP153-3xGFP-expressed U2OS cell line was first cultured, fixed and stained with anti-GFP antibody and Alexa Fluor® 568 conjugated secondary antibody. The sample was imaged with (d) spinning disk confocal microscopy and proceeded for ExM using mild digestion. (e) GFP signal and (f) anti-GFP antibody signal were both preserved after expansion. Scale bars are 1 μm in (a, d), 2.2 μm in (b, e) and 4.5 μm in (c, f) without subtracting the expansion factor.

Surprisingly, SNAP-BG-Janelia Fluor 646 preserved more signals in the nucleus region than GFP alone. Nuclei were well stained before expansion, after digestion and can still be clearly visible after expansion. Next we want to eliminate the background by either increase BG-dye signal preservation in the expanded sample or decrease the background caused by improper digestion of SNAP tag.

Synthesis and test of BG-dye-aa

The experiment was designed to directly anchor the BG-dye molecules into the hydrogel. Chemical was designed together with Isabelle Henig-Becker from Prof. Haag' s group at Freie Universität Berlin under the direct supervision of Dr. Kai Licha. The synthesis and purification of BG-dye-aa was done by Isabelle Henig-Becker. Cellular staining and test of the dye was carried out by me.

We hypothesized that the rhodamines may be the most suitable fluorescent dyes to bifunctionally conjugate BG and aa. Rhodamine dyes are widely used as fluorescent probes, for instance Alexa Fluor® 488, 568, Atto 488, 647N and Janelia Fluor 646 are all rhodamine-derivatives. Besides their high absorption coefficient, broad fluorescence spectrum, high fluorescence quantum yield and photostability (Beija, Afonso, and Martinho 2009), rhodamines are also competent to be combined with other super-resolution techniques, e.g. silicon-rhodamine for STED (Lukinavičius et al. 2013) and photo-activatable Janelia Fluor 646 for SMLM (Grimm et al. 2017). Although different modifications have been made to the derivatives, a general bi-functional synthesis to add the BG and the aa moiety to the rhodamine may still apply.

Here we used two simple versions of rhodamines, rhodamine B (RhoB) and tetramethylrhodamine (TMR) (Fig. 4.5 a) to examine: 1) if the rhodamine can be bi-functionalized and conjugated with BG and aa at the same time; 2) if the current synthesis strategy inhibit the binding of the SNAP-BG; 3) if aa can be successfully incorporated into the hydrogel matrix via polymerization; 4) if the signal of the rhodamine can be magnified after digestion and expansion. When the labelling strategy fulfill all the criteria, we aimed to further exploit it to silicon rhodamine

conjugation and perform ExSTED microscopy to do quantitative imaging of the nuclear pore complexes.

The NUP96-SNAP cell-line was prepared on coverslips and stained with BG-RhoB-aa or BG-TMR-aa in the same way as descried in the last section, except for that the working concentration of BG-dye-aa was 0.1 μM, 1 μM and 10 μM in the first experiments. The coverslips were imaged after BG-dye-aa staining to check for background staining and BG-SNAP labelling. After incubated directly with monomer solution without extra crosslinking reagents, the coverslips were embedded into hydrogels. After gelation, digestion and expansion, the hydrogels were mounted and imaged again with spinning disk confocal microscopy to check if the aa-crosslinked dye was anchored into the polymer matrix.

By directly applying the BG-dye-aa constructs with NUP96-SNAP-expressed U2OS cells, we observed fluorescent nuclei but also massive background staining. In the RhoB group, the staining covered the whole cell, although the boundary of the nucleus was slightly brighter than the other regions, the intensity from the center of the nucleus was not obviously higher than other cytosolic regions (Fig. 4.5 b). In the TMR group, much less background was observed, and the brightness of the nuclei was comparably higher than the cytosol, whereas the background staining was mostly located in the endoplasmic reticulum (Fig. 4.5 e).

I was informed about the impurity and the possible self-crosslinking-induced quenching of the rhodamine dyes (source: Isabelle Henig-Becker).Considering the background staining may be a result from the impurity of the BG-dye-aa construct, which was mainly the residues from the dye or the intermediate product BG-dye. We hypothesized that some of the background staining were not crosslinkable to the hydrogel, thus, with gelation and protease digestion, these background signals can be reduced.

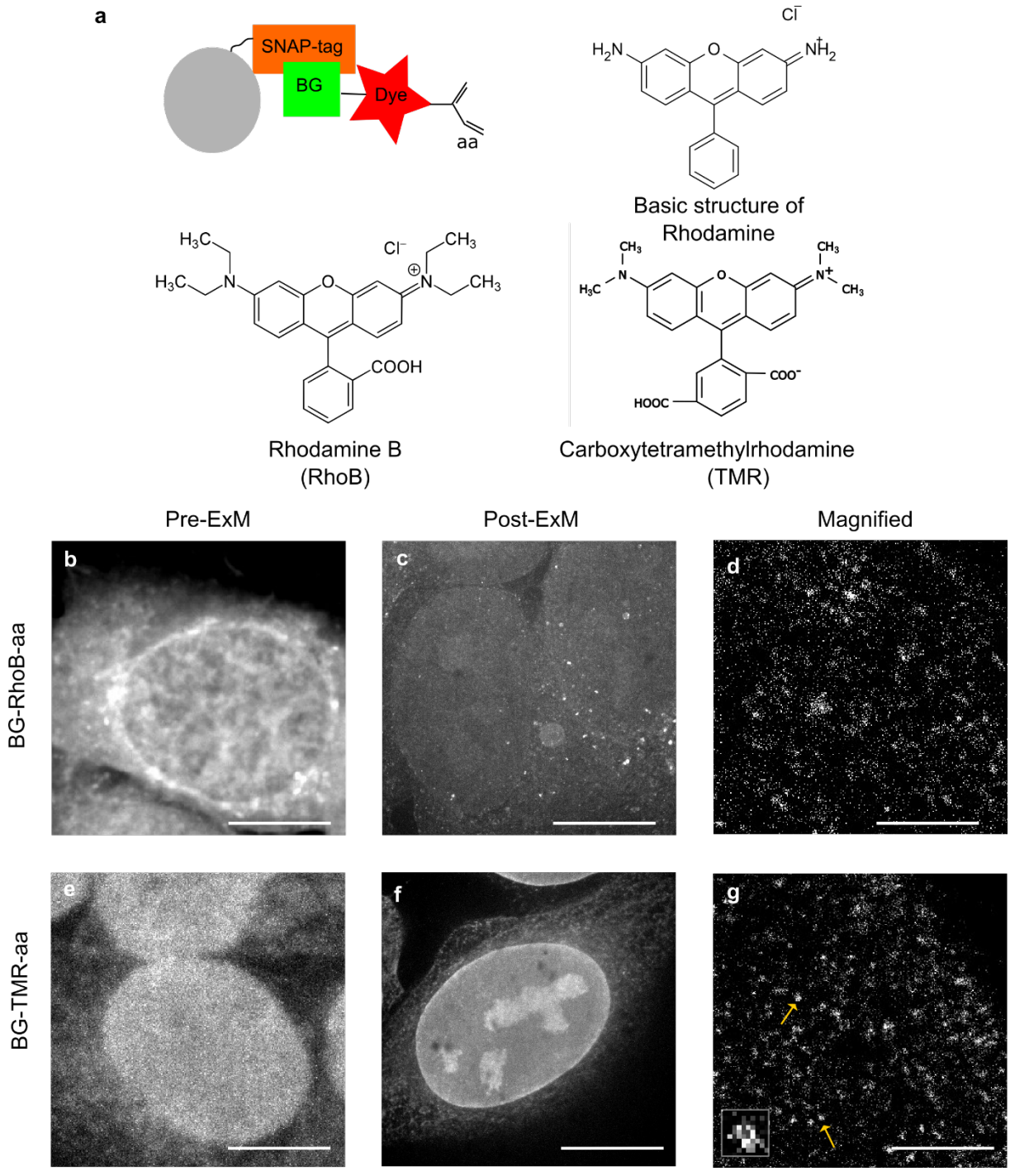

Figure 4.5 Nuclear pore complex imaged using ExM via BG-RhoB-aa or BG-TMR-aa. (a) Design of the BG-dye-aa construct and the chemical structures of rhodamine dyes. A SNAP-tagged target protein (gray) is overexpressed in cells and two rhodamine dyes (RhoB and TMR) were synthesized to carry both BG- and aa- group, which allows its binding to SNAP-tag and crosslinking into an acrylamide hydrogel. NUP96-SNAP-expressed U2OS cell line was first cultured, fixed and stained with (b) BG-RhoB-aa (e) BG-TMR-aa and imaged with spinning disk confocal microscopy. The coverslips were

directly polymerized together with the monomer solution for ExM. After a mild digestion, the expanded hydrogels for (c) BG-RhoB-aa and (f) BG-TMR-aa group were imaged again. The magnified images (d, g) were sharpened using ImageJ, and the yellow arrows indicated the nuclear pore complexes. The magnified nuclear pore was shown at the left corner of (g), where the pixel size was ~27 nm. (b, c, e, f) were maximum projected from a 3D image stacks. Scale bars are 1 μm in (a, d), 2.2 μm in (b, e) and 4.5 μm in (c, f) without subtracting the expansion factor.

Both BG-RhoB-aa and BG-TMR-aa were competent to preserve and expand nuclei in ExM. After protease digestion, we observed the signal preservation and signal loss at the same time, indicating the aa group were crosslinkable in poly-acrylamide-acylate polymerization reaction. And with further expansion in water, the size nuclei were magnified, and the background staining decreased especially in the TMR group. For the RhoB construct, the nuclei to cytosol intensity ratio was not improved and some clusters of fluorescence signals were clearly seen in the expanded cytosol (Fig. 4.5 c, f). We further sharpened the images and in the magnified view (Fig 4.5. d, g), nuclear pore complexes with slightly higher intensities were distinguishable. Nevertheless, the ring structures were less than 4-pixel size in diameter. Different orientations of the rings cannot be determined with the current resolution.

As a conclusion, we successfully established a rhodamine dye, BG-TMR-aa, which can recognize SNAP-tagged protein in cells and can retain the fluorescence in ExM. More work will be done in improving the quality of the tri-functional rhodamine dye.

Discussion

SIM

A lateral 30 nm resolution was previously reported in ExSIM imaging with the Drosophila ovary synaptonemal complex (Wang et al. 2018) and protozoan Giardia

lamblia (Halpern et al. 2017), nevertheless, spherical aberrations were mentioned in both case that limited the resolution in deep imaging (more than 15 µm from the surface). In the former case, hydrogels were cryo-sectioned to 8 - 10 µm before expansion, while the latter focused only in a narrow region closing to the surface.

During the time of the ExSIM experiment, poly-L-lysine coated glass was not yet used in prohibiting the drifting of the hydrogels. When locating the surface using an ultimate focus system with the 785 nm laser, a minimum 5 µm difference from the gel to the surface was measured. The imperfect sample mounting greatly influenced the following imaging quality. Regretfully, the experiments were not repeated with SIM after the correction of sample mounting or change of fluorophores.

Differences between RhoB and TMR

In this experiments, two different rhodamine derivatives were used. BG-RhoB-aa was limited by the unspecific binding mechanism of RhoB. When incubating the sample with RhoB or the intermediate product BG-RhoB, we observed signals all over the cells. This signal can be partially washed off in RhoB-stained samples after ExM, however, the remained bright background introduced strong interference for nuclear pore isolation in the following experiments.

By replacing RhoB with TMR, a probe that have been shown with high specificity, we improved the experiments, and established an expanded BG-TMR-aa-stained nucleus in cell. Whereas, the labelling strategy of this probe was still limited by the self-quenching of the rhodamine, i.e. the construct can interact with SNAP-tag and acrylamide group but does not emit light. In terms of the 9-fold NUP96-SNAP construct, if all the SNAP-tag are coupled to the BG-dye-aa construct, only half or less of the fluorescent signal will be seen if the quenching happens at 50 % rate. To illustrate the complete ring structure, we will further improve the stability of the probe by adding more inhibitor groups.

Loss of signal

In routine NHS-ester-amide-based antibody-dye conjugation reactions, the final labelling is feasible to reach 8 - 10 dyes per secondary antibody. And most of the commercially available dyes are ~ 3 - 6 dyes per secondary antibody. The NHS ester-based crosslinking reagent were based on the same mechanism; thus, the estimated crosslinking sites for ExM is less than 5 per commercial antibody. In our BG-dye-aa experiments, the averaged labelling on SNAP-tag is less than one dye, resulting in low fluorescence labelling after ExM. To further improve the performance of the dye, the staining efficiency of the BG-dye-aa to the SNAP-tag should also be enhanced, where hydrophilic groups may be introduced into the structure to promote the binding.

Crosslinking of the probe

In the current structure, only acrylic acid group was used to crosslink the probe to the hydrogel. The simple design was based on the previously established comparison between AcX and MA-NHS, where different acidic group were not shown to greatly affect the anchoring and polymerization. However, to eliminate background staining, we used much less concentrated (0.1 % - 1 %) probes than routine MA-NHS concentration. We aim to obtain the compound at higher purity and to reduce background staining. Then higher concentration or longer incubation with the monomer solution can be tested with the probe to optimize the crosslinking.

Outlook

In the next step, we will further exploit chromatography to quantify the potion of the closed-ring rhodamine. Besides, by applying ExSTED, we will estimate the nuclear pore complex diameter and the effective expansion factors. Improvements will be carried out on improving the current chemical purification protocol, adding inhibiting groups to block the self-crosslinking mechanism of TMR and applying different blocking reagents to the fixed samples to lower the unspecific binding.

Another application of the probe will be as a tri-functionalized linker for iExM. Currently, only DNA-oligomers were used in iExM. Similarly, an expanded gel can be stained using the probe, where SNAP-tagged proteins are labelled. After the crosslinked

structure being anchored via -aa moiety into the second polymer matrix, the first hydrogel can be disrupted. Finally, with the second gel swelling, the probes will expand, and the signals will be enlarged.

Conclusion

In this chapter, an effort was made in vain to establish ExSIM in simple cultured cells with antibody-labelled microtubules. Artifacts due to the refractive index mismatching were observed, and clear scattering from the hydrogels were also observed. With the current labelling and setup, a mixture of scattering patterns and the targeting protein were achieved and not isolatable. Further improvement should be made in the sample slicing and refractive index matching.

A new version crosslinkable BG, BG-dye-aa construct, was also introduced here, where two different organic rhodamine-derivatives were tested. We observed binding between the SNAP-BG, crosslinking by the aa and expanded nuclei when using these two constructs. However, the impurity of the constructs led to a massive background staining and further improvement will be done from the chemical clean-up of the construct and intensive blocking of the cells.

Chapter V Summary

The aim of the work was to improve the current resolution achieved by ExM and use the ultra-high resolution to verify if the expansion stayed isotropy even at nanometer scales.

In the beginning of the work, sample preparations in ExM were optimized to enhance preserve complete structures, the retaining of signals, lower the background. To do so, we conducted direct comparison between methanol- and PFA-fixation, MA-NHS- and AcX- crosslinking, pre- and post-ExM treatment staining and different proteolytic digestion. These results were quantified using fluorescent proteins or fluorescence labelled antibodies. As a result, we did not observe striking differences between fixatives and crosslinkers applied to image microtubules. However, when using H2B-mCherry as the marker, an extraordinary signal preservation was observed in PFA-fixed group with short digestion time, which indicated the influence of fixation for some organelles, e.g. nucleus.

As the second part of the work, ExM protocols were optimized for certain biological samples and a combination of STED microscopy with ExM was established. From the distributed cells (10 - 200 μm), the microtubule cytoskeleton in cells (1 - 20 μm), the centriole protein CEP152 (250 – 350 nm), the cilia cross-section (100 - 200 nm), spectrin rings in neurons (190 nm) to antibodies-labelled microtubules (~40 nm), we were able to enhance the resolution of ExM from ~ 100 nm in 2D to sub-10 nm in 2D and isotropically 50 nm in 3D. With this ultra-high resolution, we were able to show the isotropic expansion of ExM-treated microtubules at a few nanometers.

Future work on ExM will focus on further improvement of the resolution. Different methods to conjugate photo-switchable dyes were introduced in the work, which may be later used in the combination of ExM and SMLM. A tri-functional probe that can directly interact with SNAP-tag and be crosslinked into hydrogels was also designed and tested here. Efforts will be put in to improve the purity, stability and brightness of

the probe. And by applying the probe in ExSTED, we aim to achieve a nanometer ranged verification of the homogeneity of ExM.

Chapter VI Methods

Cell Culture, Fixation and Immunostaining

All cultured cells were maintained in a 37 ºC humidified 5 % carbon dioxide-controlled incubator and passaged every 3 - 5 days. Fixation buffers and washing buffers were warmed up to 37 ºC except for the methanol fixation (room-temperature PBS). Quenching, blocking, permeabilization, immunostaining and the following washing steps were carried out at room temperature without special notice. PFA for fixation was freshly taken from the commercial 16 % sealed glass bottle, or from the pre-aliquoted frozen stocks.

Primary mouse neuron

Fixed primary mouse hippocampal neurons were gifts from Prof. Brita Eickholt's lab at Charité - Universitätsmedizin Berlin. In short, neurons were plated on poly-L-lysine coated coverslips, grown for 7 - 15 DIV, and fixed with 4 % PFA plus 4 % sucrose in PBS. The neurons were subsequently permeabilized with 0.2 % Triton X-100 in PBS, blocked first with Image-IT FX® and then with neuron blocking buffer (3 % bovine serum albumin/ 0.1 % Triton X-100 in PBS) for 30 minutes. Antibodies were diluted in the neuron blocking buffer and incubated with the coverslips at room temperature for 1 hour.

The DIV 7 and DIV 15 mouse hippocampal neuron cells were fixed and immunostained with anti-β-II or -IV spectrin antibodies and the corresponding secondary antibodies (Alexa Fluor® 488-conjugated anti-mouse antibody against anti-β-II spectrin antibody and Alexa Fluor® 594-conjugated 594 anti-rabbit antibody against anti-β-IV spectrin antibody). The cells were proceeded with ExM protocols (with different monomer solutions) using AcX and 1-hour digestion.

HeLa and CV-1

HeLa and CV-1 cells were cultured in the medium with 10 % fetal bovine serum (FBS) and 1 % glutamax™ in Dulbecco's modified Eagle medium (DMEM) and then

transfected with either Neon® transfection system or Lipofectamine® 3000 reagent according to the manufacturer's instructions. With electroporation, the transfected cells were plated on 12 or 18 mm #1.5 coverslips for 48−72 hours in the same growth medium. With lipofectamine, the cells were first seeded on coverslips with 70 % confluency and grown for 24 hours. The cells were then changed to FBS-free Opti-MEM® media and the lipofectamine reagent was applied. The cells were changed back to the growth medium mentioned above after 4 hours and incubated for another 72 hours with every 24 hours refreshing of medium until fixation.

Microtubules were visualized by fixing with either methanol or pre-permeabilization-fixation protocol. In the methanol group, the coverslips were briefly washed with PBS for 3 times and moved to a Petri dish with -20 º C-cold methanol, then incubated at -22 º C for 5 minutes. The cells were followed by 5 times PBS washing before blocking. With pre-permeabilization fixation, the coverslips were pre-permeabilized for 60 seconds with pre-permeabilization buffer (0.2 % Triton X-100, 1 mM ethylenediaminetetraacetic acid in BRB80 (80 mM PIPES, 1 mM magnesium chloride and 1 mM ethylene glycol tetraacetic acid)) and quickly changed to freshly prepared microtubule-fixation buffer (4 % PFA and 0.1 % glutaraldehyde in BRB80), incubated for 10 minutes. The coverslips were then changed to freshly prepared 10 mM sodium borohydride, incubated for 5 minutes, then followed with 3 times PBS washing before blocking. CEP152 structure was also harvested with the pre-permeabilization-fixation protocol. All samples were blocked with Image-IT FX® and then blocking buffer (4 % Horse serum, 1 % bovine serum albumin and 0.1 % Triton X-100 in PBS) for 30 minutes. Antibodies were diluted in the blocking buffer and incubated with the coverslips at room temperature for 1 hour or 8 ºC overnight.

CEP152 was visualized by fixing with methanol. The coverslips were incubated with -20 ºC-cold methanol for 10 minutes, followed by twice ice-cold PBS washing. The coverslips were blocked with Image IT and 3 % bovine serum albumin separately. A polyclonal antibody produced against the C-terminus of human CEP152 protein was applied to immunostained CV-1 cells. Abberior Star Red conjugated secondary

antibody was chosen to be compatible with STED imaging and α-tubulin was co-immunostained with Alexa Fluor® 488.

NUP96-U2OS

U2OS cells were cultured in medium with 10 % FBS, 1 % L-glutamine, 1 % non-essential amino acid and 1 % penicillin-streptomycin. The cells were plated on coverslips or 8-well glass-bottom ibidi chamber® for 24 hours before fixation. Cells were first pre-fixed with 2.4 % PFA in PBS for 30 seconds, then quickly changed to 0.4 % Trition X-100 in PBS for 3 minute-pre-permeabilization, finally fixed with 2.4 % PFA in PBS for 30 minutes. 100 mM ammonium chloride was followed, and 3 times PBS washing were applied. The cells were incubated with Image-IT FX® for 30 minutes, and then incubate for 50 minutes with the SNAP-staining solution, which contains 1 mM BG-dye, 1 mM dithiothreitol, 1 % bovine serum albumin in PBS.

MDCKII and RPE

MDCKII cells were cultured for 2 weeks in minimum essential medium (MEM) supplemented with 110 mg/L sodium pyruvate, 2 mM non-essential amino acid, and 5 % FBS and fixed with 4 % PFA in PBS. The fixed cells were washed intensively with PBS, blocked, and then immunostained in the same buffer as HeLa. To get the cilia closer to the surface, a poly-L-lysine coated coverslip was applied on the coverslip with cultured MDCK II cells, and quickly lifted.

RPE cells were cultured in DMEM-F12, supplied with 10 % FBS, 2 mM sodium pyruvate and 0.01 % hygromycin B and plated on coverslips. To harvest cilia, the cells were grown to near 70 % confluency and changed to a starvation medium that have similar medium except with 0.5 % FBS. After 48 hours, the average cilium length was ~ 5 µm.

Blocking and antibody staining for cilium was done with the same procedure as HeLa and with more gentle pipetting.

Antibody/ Nanobody preparation and immunostaining

Nanobodies were produced in house with the protocol mentioned in (Mikhaylova et al. 2015; Platonova, Winterflood, and Ewers 2015). Most of the secondary antibodies were purchased in the form with fluorescent dye conjugation. Partially of the secondary antibodies, tubulin antibodies and nanobodies were labelled with fluorescent dyes in house. With NHS ester-amide reaction, 80 µg or 1.3 mg/ml antibody was first buffer exchanged to 0.2 M sodium hydrogen carbonate using Zeba® desalting column with 40 KDa cutoff, and then mixed with 5- or 10-fold molar excess of NHS ester-fluorescent dyes to achieve 3 dyes per antibody or 6 - 8 dyes per antibody labelling efficiency. The sample was briefly mixed by vortex, wrapped with Aluminum foil and placed into a rotator. After 1-hour rotating, 1/10 volume of 1 M Tris-hydrochloride (pH 8) was added to terminate the reaction. The sample was centrifuged with table centrifuge for 30 seconds then proceeded to 3 times Zeba® column desalting. Nanobodies were labelled in a similar procedure, with less than 250 µl and 0.4 mg/ml starting material, 10-fold molar excess of dyes and 7 kDa cutoff Zeba® columns. The product concentration was measured with Nanodrop 1000 with UV-Vis mode then sodium azide was added to the concentration of 0.01 %.

In *d*STORM and post-expansion staining experiments, primary antibodies, secondary antibodies and nanobodies were used at concentrations of 1 – 5 µg/ml, 2 µg/ml and 4 µg/ml correspondingly. In the pre-staining experiments, primary antibodies, secondary antibodies and nanobodies were used at concentrations of 5 – 20 µg/ml, 10 µg/ml and 20 µg/ml correspondingly.

ExM, MAP & U-ExM

The monomer solution (different in the three protocols) was prepared from 40 % Acrylamide solution, 2 % N,N′- methylene-bis-(acrylamide) except for MAP protocol where the acrylamide was prepared from powder. Monomer solution, tetramethylethylenediamine (10 % in water), ammonium persulfate (10 % in water),

crosslinking reagent (1 M MA-NHS in DMSO or 10 mg/ml AcX in DMSO) digestion buffer (50 mM Tris-hydrochloride, 1 mM ethylenediaminetetraacetic acid, 0.1 % Triton X-100, 0.8 M guanidine-hydrochloride, and pH 8.0) were aliquoted, stored at -20 ºC and thawed on ice every time before use. The monomer solution was heated at 50 ºC for short time and put back in ice when crystals visible in the solution.

ExM

The immunostained coverslips were first incubated with crosslinking reagent diluted in PBS (10 minutes to 1 hour with 25 mM MA-NHS, 3 - 12 hours with 0.1 mg/ml AcX or 10 minutes with 0.25 % glutaraldehyde) then briefly rinsed with PBS for 3 times before changed to monomer solution for 1 - 10 minutes' incubation. Meanwhile the gelation chamber was pre-cooled on ice. Hydrogels were formed by adding a final concentration of 0.15 % tetramethylethylenediamine and 0.15 % ammonium persulfate to the monomer solution (8.625 % sodium acrylate, 2.5 % acrylamide, 0.15 % N, N'-methylenebisacrylamide in PBS, 2 M NaCl or 8.625 % sodium acrylate, 10 % acrylamide, 0.1 % N, N'- methylenebisacrylamide, 1 M NaCl in PBS), mixing by vortex and putting the coverslip upside down to the drop of the solution. Gelation took place on ice for 5 minutes and in a humidity incubator at 37 ºC for 1 - 2 hours. Proteinase K was diluted to 8 U/ml in the digestion buffer and applied to the sample 50 ºC for 2 hours or 37 ºC overnight. Digested gels were transferred to dishes with Milli-Q® water for further expansion. Water was exchanged every 30 minutes 3 − 5 times until the gel spread out in all dimensions.

MAP

The coverslips with cultured cells were fixed in PFA-/ glutaraldehyde-/ methanol containing buffers according to specific applications, then change to 4 % PFA and 30 % acrylamide in PBS without washing. After 4 - 5 hours of incubation at 37 ºC, the coverslips proceeded directly to gelation with 7 % sodium acrylate, 20 % acrylamide, 0.1 % N, N'- methylenebisacrylamide in PBS as a monomer solution and 0.5 % of tetramethylethylenediamine and 0.5 % ammonium persulfate as accelerator and

initiator. The reaction was carried on ice for 1 minute then transferred to 37 ºC for another 1-hour incubation. The gels were further transferred to a Petri dish containing room-temperature denaturation buffer (200 mM SDS, 200 mM sodium chloride in 50 mM Tris-hydrochloride, pH 9.0) for 15 minutes, then to a falcon containing 95 ºC denaturation buffer. After shaking at 95 ºC for 1 hour, the gels were briefly washed with distilled water in a beaker, then expanded twice with water for 30 minutes each and twice for PBS for 15 minutes each. In the preparation for pre-staining in MAP-treated samples, the coverslips were washed several times with PBS after 4 % PFA and 30 % acrylamide incubation. Then the antibodies were used for the immunostaining in the blocking buffer. After a few times of PBS washing, the coverslips were proceeded to gelation. In the post-expansion staining experiments, the gel was cut into appropriate size for the following overnight primary antibody staining (diluted in 2 % bovine serum albumin in PBS) at room temperature. After three times of 10 minutes PBST (0.1 % tween-20 in PBS) washing, the gel was changed to secondary antibody staining solution (diluted in 2 % bovine serum albumin in PBS) and shake again at room temperature for 6 hours, followed with three times PBST washing. The gel was expanded in water for twice, 30 minutes of each then left in water at 8 ºC before imaging.

U-ExM

The coverslips with cultured cells were fixed according to the applications, then changed to freshly prepared 0.7 % formaldehyde and 1 % acrylamide in PBS. After 5 hours of incubation, the gel was formed with monomer solution (19 % sodium acrylate, 10 % acrylamide, 0.1 % N, N'- methylenebisacrylamide in PBS) and 0.5 % of tetramethylethylenediamine and 0.5 % ammonium persulfate. Gelation took place on ice for 5 minutes, then was carried out at 37 ºC for 1 hour. Denaturation, washing and staining was performed as mentioned in MAP, except that the secondary antibody staining was carried out at 37 ºC for 3 hours.

Comparison between AcX and MA-NHS with different digestion time

Cells were cultured on a coverslip, incubated for 24 hours before imaged with spinning disk confocal microscopy using relatively low intensity (1 – 5 % 100 mW 491 nm or 561 nm lasers) and exposure time (50 – 100 ms). I first checked the signals of microtubules and nuclei in live cells and then applied different fixation methods to the coverslips: 1) 7 minutes incubation with -20 ºC-cold methanol, followed up with 5 times (at 0, 1, 5, 15, 30 minutes after the fixation) washing in PBS at room temperature; 2) Pre-permeabilization for 30 seconds using 0.1 % Triton X-100 in PBS, followed by 15 minutes 37 ºC 4 % paraformaldehyde (PFA) in PBS. Followed by 5 minutes of 50 mM ammonium chloride quenching, the coverslips were washed several times with PBS. Both samples were carefully blocked for one hour using 4 % horse serum and 1 % fetal bovine serum in 0.2 % Triton X-100 containing PBS solution. The coverslips were imaged using identical exposure times and laser intensities with spinning disk confocal microscopy and then incubated with AcX or MA-NHS in PBS overnight. Here 1 mM final concentration was applied for both crosslinkers. After gelation, all samples were incubated with a digestion solution containing proteinase K at 50 ºC with shaking for 30 minutes to 15 hours. Gels were expanded in distilled water before imaging. To quantify the result, 10 x 10 pixel areas on microtubules and on H2B were taken and averaged. The experiment was conducted twice with 2 gels of each group, and 3 cells selected from each gel.

Comparison between fixation methods

Cells were cultured, fixed using 1) methanol, 2) 3.2 % PFA with 0.1 % glutaraldehyde 3) Pre-permeabilization followed with 3.2 % PFA with 0.1 % glutaraldehyde or 4) Pre-permeabilization with 0.1 % triton followed with 3.2 % PFA and blocked as describe above. A mixture of two mono-clonal anti-GFP antibody was applied to the coverslips, and later washed and exchanged to Atto 655-conjugated secondary antibody. The coverslips were imaged first then crosslinked using MA-NHS and 1-hour 50 ºC digestion with proteinase K containing solution. After expansion of the gels, images were taken in both GFP channel and the corresponding

Comparison between pre- and post-staining

HeLa cells were first cultured onto coverslips and fixed using -20 ºC cold methanol. After PBS washing, one coverslip was immunostained with anti-β-tubulin and Abberior Star Red conjugated secondary antibodies, treated with the AcX-based ExM protocol mentioned in the last section except for that the U-ExM monomer solution was used instead of ExM monomer solution to be consistent with the post-staining group. Another coverslip was first incubated with 0.7 % formaldehyde and 1 % acrylamide overnight and then incubated with the U-ExM monomer solution. Polymerization was performed in the same way as described in AcX-based ExM protocol. Denaturation was done at 95 ºC for half an hour in a falcon fulfilled with SDS containing denaturation buffer. The expanded gel was washed in water and PBS before it was cut into small pieces. One small piece of the gel was incubated overnight with anti-β-tubulin antibody in bovine serum albumin contained solution. After intensively washing, the gel was incubated again with an Abberior Star Red conjugated secondary antibody in bovine serum albumin contained solution for another 3 hours. After washing with PBS, the gel was re-expanded in water and imaged together with the ExM sample on aconfocal microscope.

Nanobody labelling

HeLa cells were fixed and immunostained using anti-tubulin-antibody and Alexa Fluor® 568-conjugated secondary antibody. In pre-staining group, the sample was stained with Atto 488-conjugated anti-tubulin-nanobody (Mikhaylova et al. 2015) and proceeded with ExM. In post-staining group, the MAP-treated hydrogel was prepared directly from the tubulin-immunostained HeLa cells using antibodies and a CF® 680-conjugated anti-tubulin-nanobody was applied to stain the digested and washed gel.

SNAP-tag labelling

The BG-dyes were first tested with SNAP-expressed live cells with 1 - 10 µM dilution in growing medium or PBS for 30 minutes to 2 hours, then changed to fresh PBS for 3 times, 30 minutes each. The cells were imaged then fixed, finally expanded. Intensity

of each steps were compared.

Microscopy and image Analysis

Sample mounting

The coverslip for imaging was first plasma cleaned, then incubated with poly-L-lysine, and finally air-dried after removal of liquid. Gels that were imaged for more than 1 hour were further fixed using picodent twinsil® (Fig. 6.1). The expansion factor was calculated by overlapping the air−water boundary in original and swollen gels or by the distances between landmarks in the pre- and post-ExM cells. Thickness of the gel was calculated from the volume of the gelation solution and the surface area for pre-swelling gel and measured by a Vernier caliper for the post-expanded gel.

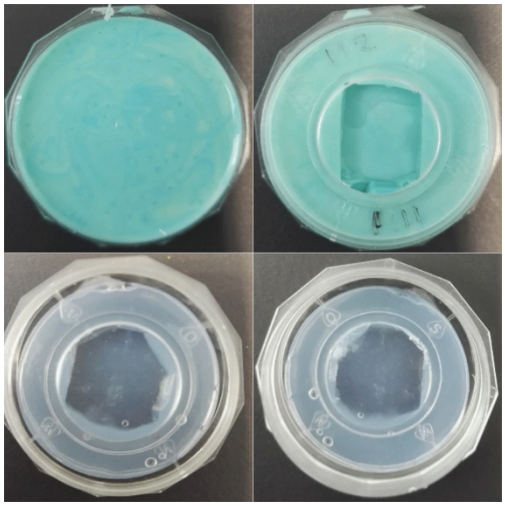

Figure 6.1 Example of hydrogel mounting. Both picodent twinsil® (upper) and 2 % low-melting agarose (bottom) can seal the expanded hydrogel without large air bubble. Shown are the top- (left) and bottom-(right) view of the sealed hydrogel. The sealing materials were applied first at the hydrogel boundaries carefully to prevent its embedding underneath the hydrogel. After the sealing materials were solidified, more should be applied to cover the whole upper surface of the hydrogel to prevent water evaporating from the hydrogel.

Confocal microscopy

Standard fluorescence microscopy was performed on an inverted Olympus IX71

microscope equipped with a CSU-X1 spinning disk (Yokogawa). 100x/1.4 NA oil- (MPLAPON), 60x/1.49 NA oil- (ApoN), 60×/1.42 NA oil- (Plapon), 60x/1.2 NA water- (UPlanSApo), 40x/1.3 NA oil- (UPlanFLN), 20x/ 0.75 NA air- (UPlanSApo) immersion objective from Olympus was used together with a 491 (100 mW; Cobolt), 561 (100 mW; Cobolt), and 645 nm (500 mW; Melles Griot) laser. A quad-edge dichroic beam splitter (446/523/600/677 nm; Semrock) was used to separate the fluorescence emission from the excitation light, and final images were taken with CMOS camera (C11440, ORCA-Flash4.0 V2 Hamamatsu) or CCD camera (cool SNAP HQ2 photometrics) or EMCCD camera(C9100, ImageEM X2 Hamamatsu). Z-scanning were taken with piezo control (E-665 Amplifier/ Servo controller, Physik Instrumente) PSF of the setup was measured with 100 nm tetra speck® beads on coverslips.

SIM

SIM imaging was performed using a DelataVision® OMX SR imaging system (GE life sciences) in the core facility AMBIO, Charité - Universitätsmedizin Berlin with a 60x/1.42 NA oil-immersion objective and #18 immersion oil. 0.08 x 0.08 x 0.125 μm^3 voxel-size was used and 50 ms exposure was applied to both pre- and post-ExM samples. Samples were first imaged on a deconvolution microscopy with same objective to track the exact position of single cell, then moved to the SIM setup to take ultra-resolution images. Further analysis was performed with the OMX SR visualization software.

STED microscopy

STED imaging was performed using a custom designed Abberior 775 3D-2 Color-STED system in Dr. Alf Honigmann's group at MPI-CBG, Dresden with 60×/ 1.2 NA water-immersion and 100×/ 1.4 NA oil-immersion Olympus objectives. Alexa Fluor® 594 was imaged with a pulsed laser at 560 nm, and excitation of Abberior Star Red was performed at 640 nm. The depletion laser for both colors was a Katana 775 nm pulsed laser. To reduce high frequency noise, STED images were filtered with a 2D or 3D Gaussian with a sigma of 0.8 pixels. Deconvolution was done with a MATLAB script

with simulated PSF information.

STORM

STORM imaging was performed using Vutara 352 super-resolution microscope (Bruker) with 60x/ 1.49 NA oil-immersion Olympus objective and a Hamamatsu ORCA Flash 4.0 sCMOS camera. Localization and data analysis were performed using Vutara SRX software.

FWHM and average radius measurements

The images were analyzed using MATLAB and Fiji (Schindelin et al. 2012). Line profiles perpendicular to microtubules were Gaussian-fitted to calculate the FHWM and average intensity.

Expansion distortion measurements

Distortion levels were estimated using the same scenario described before (Chen et al. 2015). In brief, by applying a smoothing step based on the anisotropic partial differential equation, the pre- and post-ExM images were first smoothed and then fed into a non-rigid registration technique based on a B-spline transformation model. Finally, the root-mean-square error between the pre-ExM image and the registered version of the post-expansion image was calculated using the technique suggested in references (Chen et al. 2015; Chozinski et al. 2016; Tillberg et al. 2016) and plotted as a curve. The programming was done in MATLAB with a GUI interface, mainly coded by Dr. Amin Zehtabian from Prof. Helge Ewers' lab (Fig. 6.2).

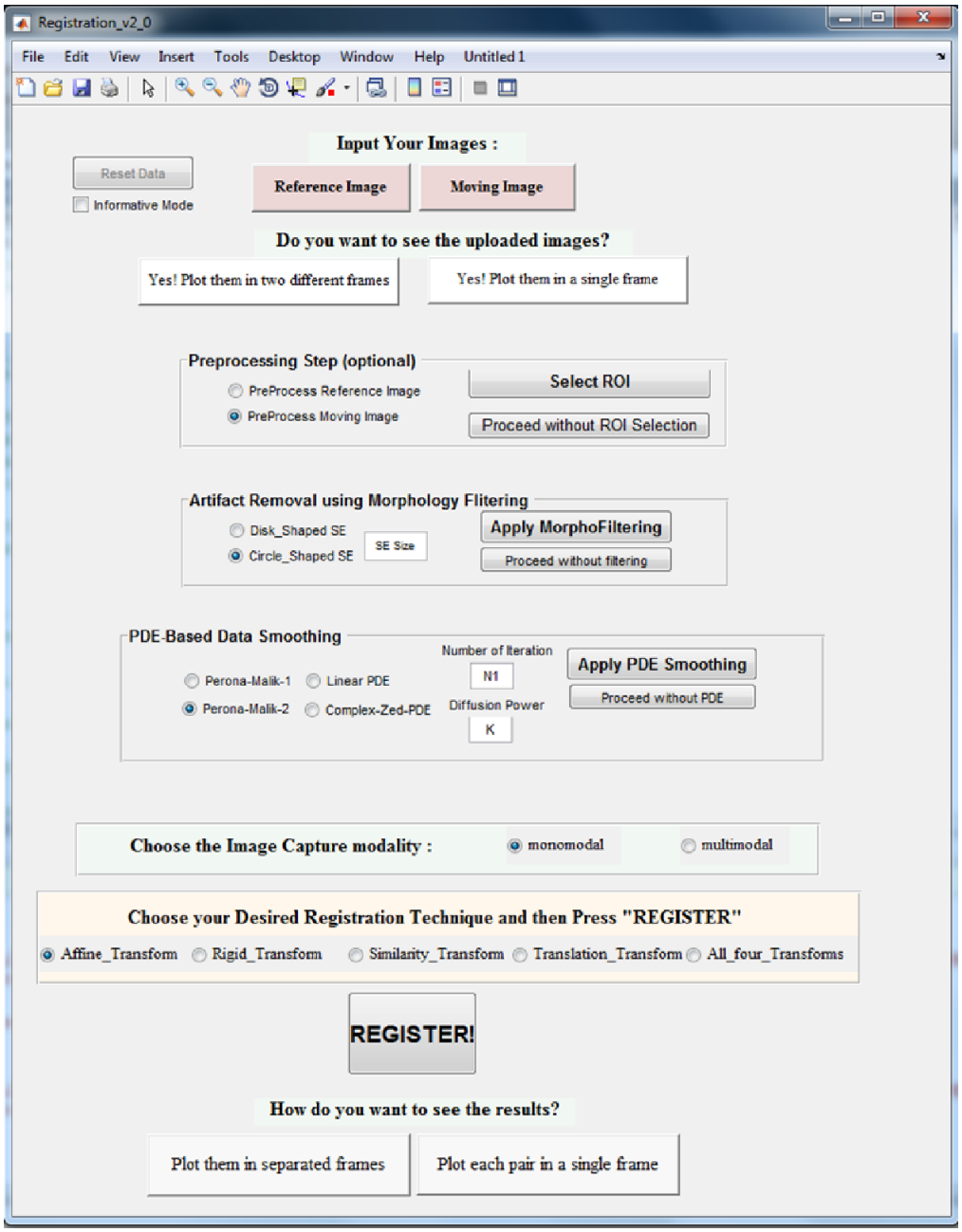

Figure 6.2 Graphical user interface (GUI) interface for the reregistration and distortion analysis.

Appendix

Visualization of actin filaments using ExM

In many super-resolution publications, phalloidin (Xu, Babcock, and Zhuang 2012) and the phalloidin-derivative SIR-actin dyes (Melak, Plessner, and Grosse 2017) were used to probe actin fibers at nanometer scale precision. The small actin-binding probe has been shown to be competent in live- and fixed- cell imaging. However, the ExM protocols for actin were not yet well-established. We applied ExM phalloidin stained cells using AcX or MA-NHS-based protocols, but the signal did not retrieve after digestion.

As a replacement, we used anther GFP-tagged actin binders to visualize actin filaments, lifeact-GFP. In the past studies, lifeact has been utilized in visualizing F-actin cytoskeleton without harsh impact on its dynamics however it was also known to identify G-actin, which gave a higher cytosolic background than phalloidin. Here lifeact-GFP transient transfected cells were incubated and imaged in live cell experiments. After 24 hours of expression, lifeact-GFP was abundant in cells, mostly binding to actin cytoskeleton but also existing in the cytosol. The cells were fixed with 4 % PFA, blocked and immunostained with anti-GFP antibody and Alexa Fluor® 568-conjugated secondary antibody. Finally, ExM was applied to the coverslips and images were taken with both coverslips (Fig. S1 a - c) and expanded gels (Fig. S1 e - g, i - k).

As a result, an expanded actin structure was observed with both lifeact-GFP and the GFP antibodies, which indicated that the binding mechanism of lifeact were not greatly influenced by the ExM protocol as phalloidin. Directly comparison between the lifeact-GFP and GFP antibody staining was carried out in the cortex and stress fiber region. Similar to tubulin-GFP, antibody staining showed a comparably high signal to noise and high signal preservation for the signals. A high background was still observed in the GFP channel, which may be contributed by the non-specific binding of GFP residues or the dissociation of lifeact-GFP during the early fixation step.

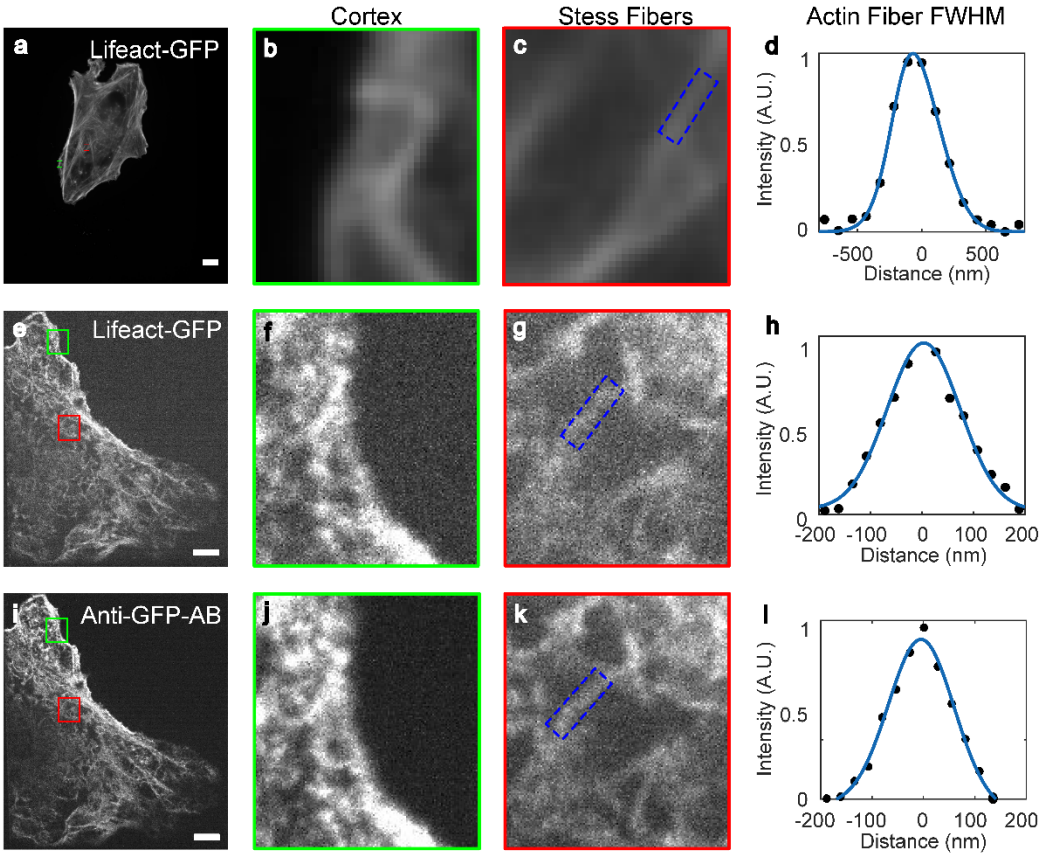

Figure S1 Actin and actin binding proteins identified with lifeact-GFP and antibodies. (a) Lifeact-GFP overexpressed cells imaged using spinning disk confocal microscopy. The cell was further labelled using anti-GFP antibody and expanded. Post-expansion GFP (e) and GFP antibody (i) signals were compared. (b, f, j) Magnified (40-fold in pre-ExM and 10-fold in Post-expansion) cortex from the green-square marked regions in (a, e, j). (c, g, k) Magnified (40-fold in pre-ExM and 10-fold in post-ExM) stress fibers from the red-square marked regions in (a, e, j). (d, h, l) Individual actin fibers (examples circled in blue in c, d, k) were manually selected and the cross-section brightness profiles were plotted and fitted using Gaussian distribution. Scale bar 1 µm.

Small, thin actin fibers were imaged before and after expansion, the cross-sections of the filaments were fitted with a Gaussian distribution and calculated for the FWHM. In pre-ExM images, the bundles of actin were not separable, which resulted in a FWHM

466.4 nm for lifeact-GFP. After expansion, the measured FWHM shrunk to 166.9 nm for GFP channel and 149.4 nm for the antibody staining channel. The result was still much higher compare to the actin visualization ~ 30 - 40 nm using routine STORM microscopy but opened the door for observing F-actin associated protein with ExM.

MAP applied to tissues

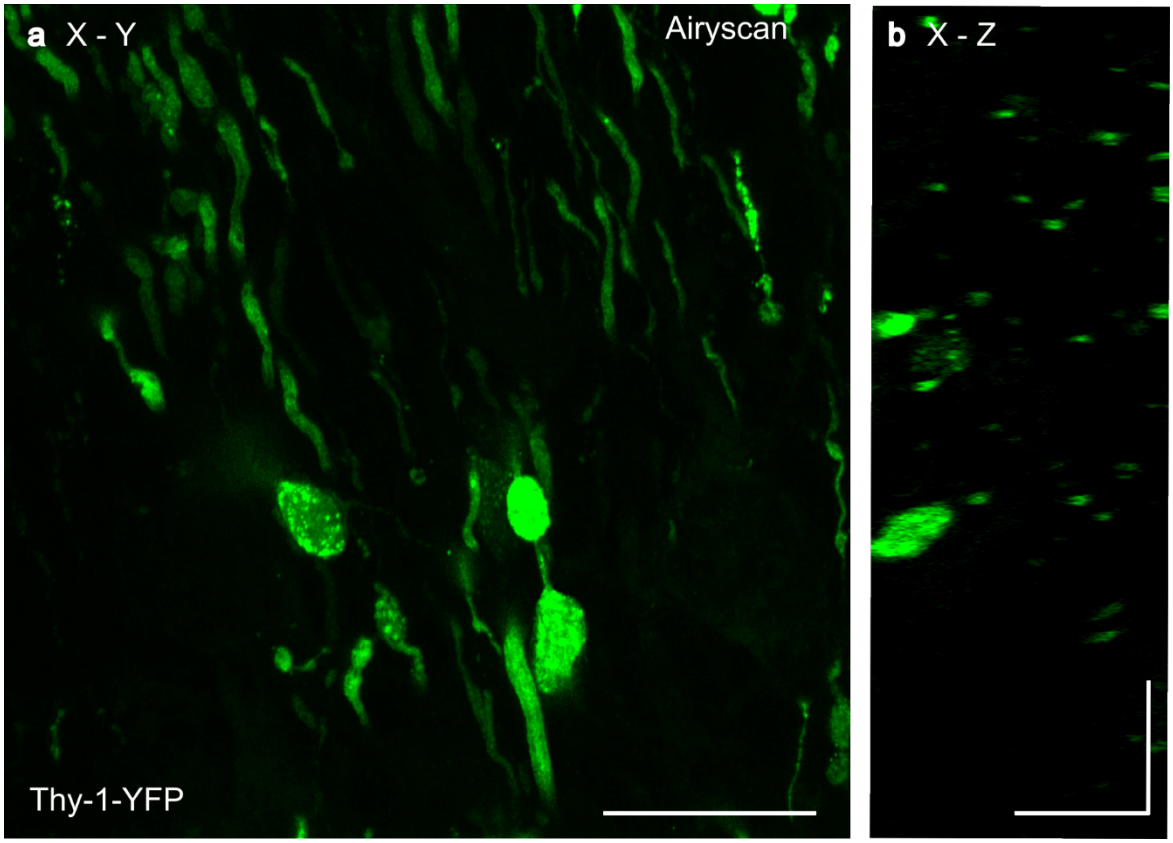

Figure S2 Thy-1-YFP-expressed mouse brain tissue expanded using MAP protocol without immunostaining. The expanded sample was imaged using Zeiss Airyscan confocal microscope plus a 25 x/ 0.8 NA oil-/ water-/ glycerol-immersion objective. The (a) X-Y plane and (b) X-Z plane were taken with water immersion. MAP method maintained YFP signal in the expanded tissue and shown were near isotropic 3D resolution. Scale bar 5 µm.

Comparing different crosslinkers and digestion conditions using spectrins in neurons

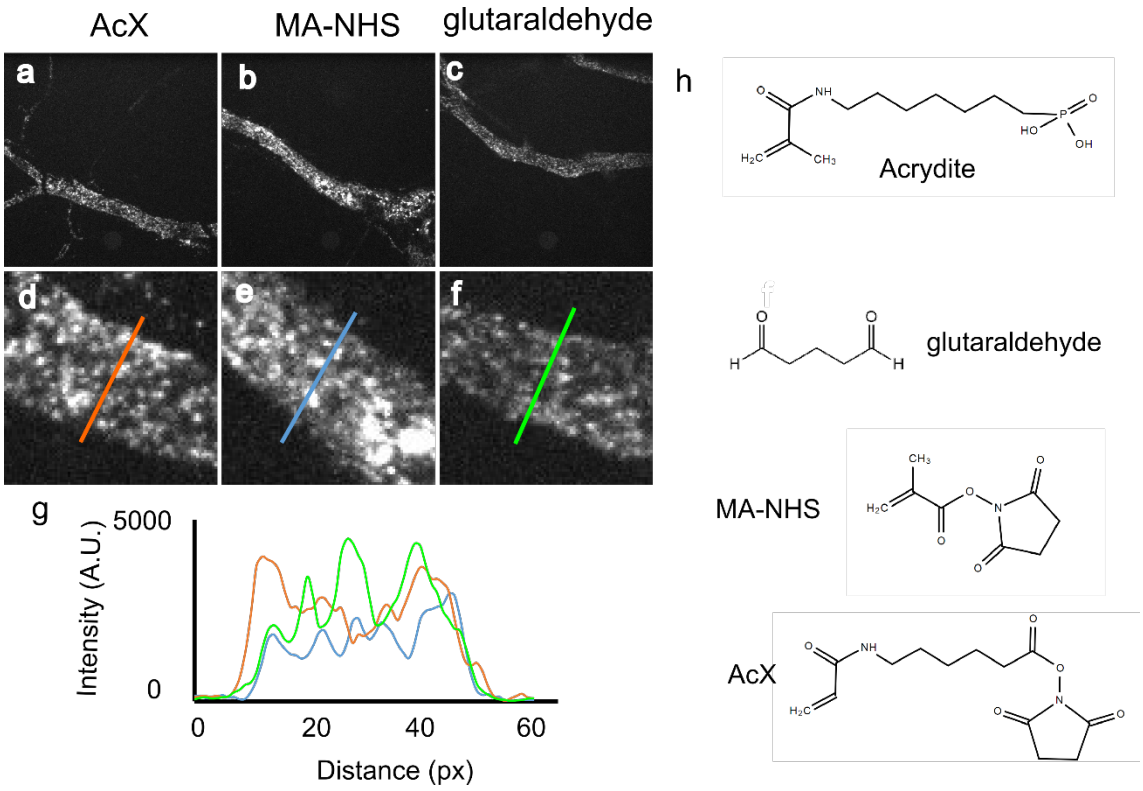

Figure S3 Comparison between different crosslinking reagents (AcX, MA-NHS, glutaraldehyde) in ExM. Mouse hippocampal neurons were plated on a coverslip and immunostained against β-II spectrin. The coverslip was broken into 4 small pieces using a diamond knife. The broken coverslip was place in a 12-well cell culture plate incubated with the following solution: (a) overnight 0.1 mg/ ml (0.35 mM) AcX in PBS; (b) 1 hour 25 mM MA-NHS in PBS; (c) 10 minutes 0.5 % (50 mM) glutaraldehyde in PBS. After ExM treatment, the gels were fully expanded and imaged using a spinning disk confocal microscope with an EMCCD camera. Structure were shown at the same brightness scaling. (d - f) were the magnified from the brightest area in (a - c) correspondingly. Line-scans were taken perpendicular to the axon direction, and the intensity vs distance was plot in (g) with AcX in orange, MA-NHS in green and glutaraldehyde in blue. The background signal was comparable in all three cases, nevertheless, signals in the glutaraldehyde gel were around half as the other two groups. The result did not show a striking difference between AcX and MA-NHS though.

(h) The chemical structure of Acrydite®, AcX, MA-NHS and glutaraldehyde. The area in (a - c) is 512 x 512 pixels, in (d - f) is 80 x 80 pixels, with 221.3 nm/ pixel in x and 220.4 nm/ pixel in y.

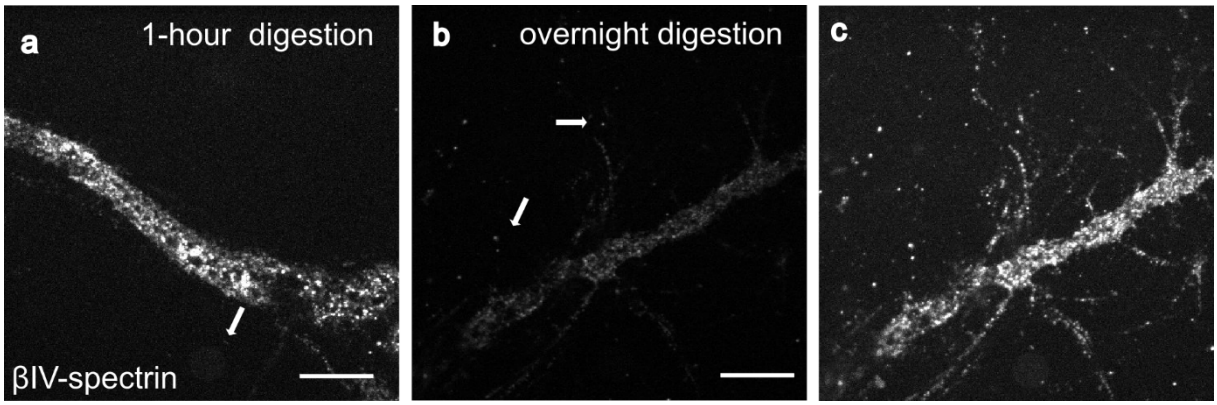

Figure S4 Comparison between 1-hour and overnight digestion of MA-NHS-crosslinked spectrin-immunostained neurons. Mouse hippocampal neurons were immunostained against β-IV spectrin and crosslinked via MA-NHS. The polymerized sample divided into two, which was incubated at 50 ºC for (a) 1 hour or (b) overnight. Both gels were washed intensively and expanded before imaged with a spinning disk confocal microscope with CCD camera. The overnight digested sample was with less fluorescence signals and (c) after scaling, the structures were still complete, but the background signals were comparably high to the short-time digested sample. White arrows indicated the clusters of fluorescent signals in the gel. Scale bars 2.5 μm.

Fluorescence partially retained in the hydrogel over long-term storage

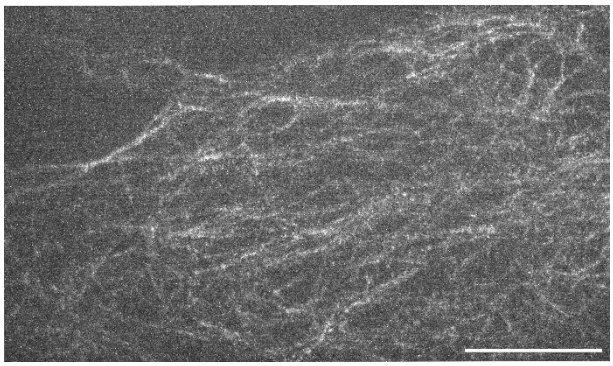

Figure S5 Fluorophore-carrying gels can be re-expanded and imaged after dehydration. Tubulin-immunostained HeLa cells were prepared according to ExM protocol, and the expanded gel was dehydrated slowly at 37 ºC in a petri dish with gentle shaking every half an hour. The shrunk gel was then parafilmed and stored at room temperature for 6 months. After adding water, the gel rehydrated, and fluorescent signal was still visible in the re-expanded gel. Surprisingly, MA-NHS-crosslinked gel could be stored for up to half year upon rehydrated allow to find the fluorescent structure again, suggesting that the crosslinking is very covalent and robust. However, only shorter time storage in water is recommended to ensure the maximum signal retention and lowest distortion. Scale bar 5 μm.

Comparing different crosslinkers and homogenization using microtubules

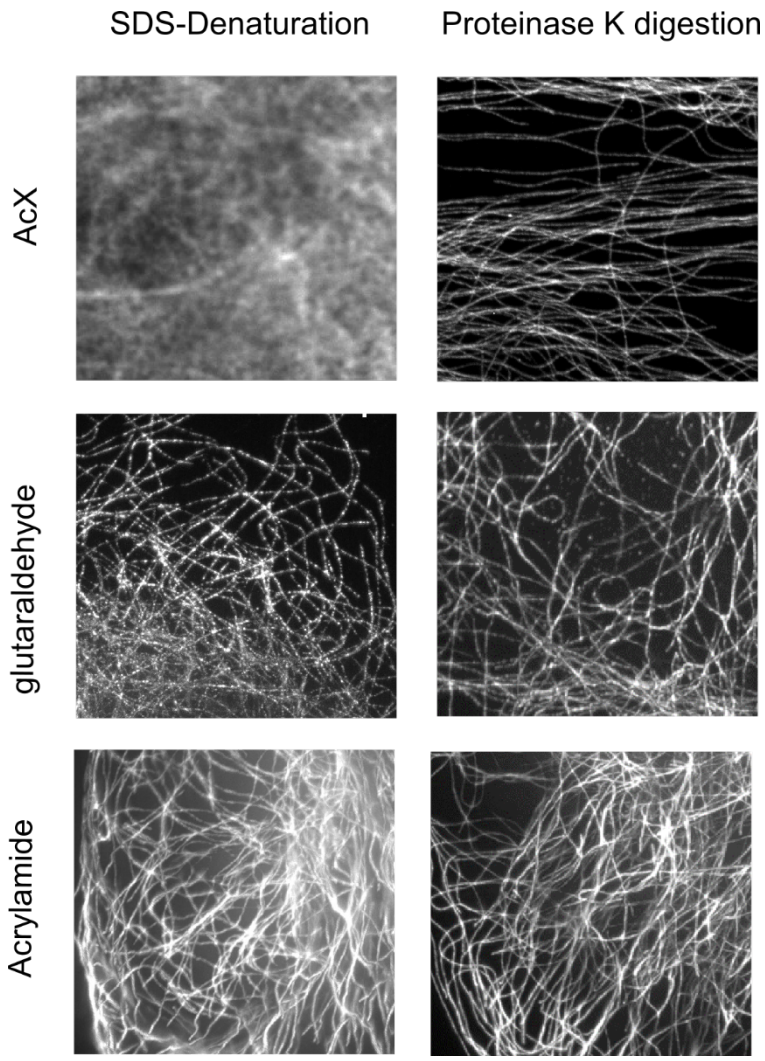

Figure S6 Different crosslinkers were tested in combination with different homogenization methods. 0.1 mg/ml AcX, 0.1 % glutaraldehyde and 20 % acrylamide together with 4 % PFA were used separately to crosslink the sample, and 95 ºC SDS-contained denature buffer or 37 ºC proteinase K contained digestion buffer were applied individually to the crosslinked gels. In the experiments, AcX-crosslinked and proteinase K-digested samples were more reproducible and showed high signal to noise ratio.

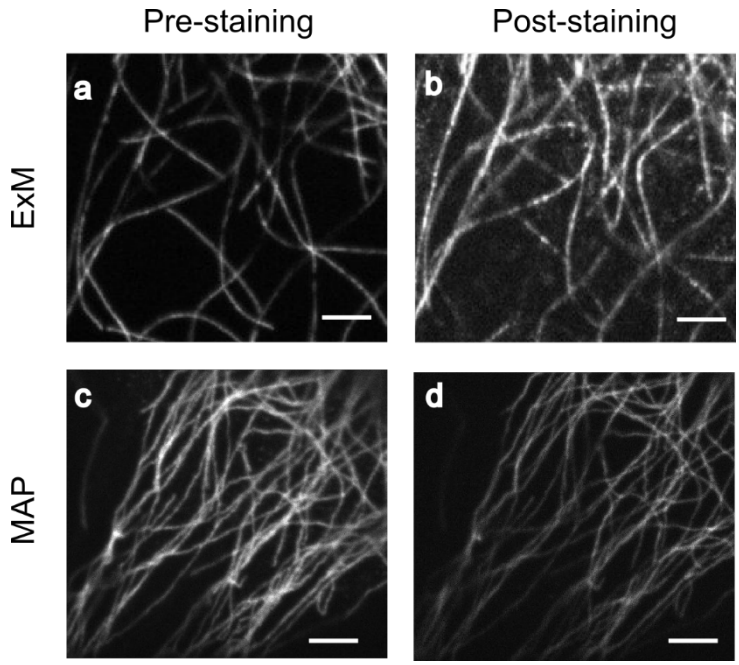

Figure S7 Comparison between post-staining in ExM and MAP. HeLa cells were fixed and immunostained using Atto 488-conjugated anti-tubulin-antibody (~ 10 dyes per antibody on average) and proceeded with ExM with O-hour 37 ºC Proteinase K digestion. The cells were treated with MAP (6-hour 30 % acrylamide and 4 % PFA incubation) and immunostained in the same way. After the gelation, denaturation buffer was applied at 95 ºC for one hour. Both samples were washed intensively in water and PBS and incubated overnight in a solution containing Alexa Fluor® 647-conjugated secondary antibody against the anti-tubulin-antibody. The gels were expanded in water and imaged with spinning disk confocal microscopy. Shown are expanded (a) pre-stained and (b) post-stained antibody signal with ExM and expanded (c) pre-stained and (d) post-stained antibody signal with MAP. In general, MAP was more efficient in post-staining than ExM, where the signals were brighter, homogenous and the structures were more complete. Scale bar 2 µm.

Publications

During the time of my doctoral work, I participated in the following publications:

Mengfei Gao, Riccardo Maraspini, Oliver Beutel, Amin Zehtabian, Britta Eickholt, Alf Honigmann, and Helge Ewers. 2018. ‘Expansion Stimulated Emission Depletion Microscopy (ExSTED)’. *ACS Nano* 12(5):4178–85.

Marcus Braun, Zdenek Lansky, Agata Szuba, Friedrich Schwarz, Aniruddha Mitra, Mengfei Gao, Annemarie Lüdecke, Pieter Rein ten Wolde & Stefan Diez. 2017. ‘Changes in microtubule overlap length regulate kinesin-14-driven microtubule sliding’. *Nature Chemical Biology* 13: 1245–1252.

Bibliography

Agasti, Sarit S., Yu Wang, Florian Schueder, Aishwarya Sukumar, Ralf Jungmann, and Peng Yin. 2017. ‘DNA-Barcoded Labeling Probes for Highly Multiplexed Exchange-PAINT Imaging’. *Chemical Science* 8(4):3080–91.

Ahmed, Enas M. 2015. ‘Hydrogel: Preparation, Characterization, and Applications: A Review’. *Journal of Advanced Research* 6(2):105–21.

Abberior Instruments GmbH’. Retrieved 28 June 2019 (https://www.abberior-instruments.com/products/).

Ariel, Pablo. 2017. ‘A Beginner’s Guide to Tissue Clearing.’ *The International Journal of Biochemistry & Cell Biology* 84:35–39.

Asano, Shoh M., Ruixuan Gao, Asmamaw T. Wassie, Paul W. Tillberg, Fei Chen, and Edward S. Boyden. 2018. ‘Expansion Microscopy: Protocols for Imaging Proteins and RNA in Cells and Tissues’. *Current Protocols in Cell Biology* e56.

Auer, Alexander, Thomas Schlichthaerle, Johannes B. Woehrstein, Florian Schueder, Maximilian T. Strauss, Heinrich Grabmayr, and Ralf Jungmann. 2018. ‘Nanometer-Scale Multiplexed Super-Resolution Imaging with an Economic 3D-DNA-PAINT Microscope’. *ChemPhysChem* 19(22):3024–34.

Barbu, Tudor. 2013. ‘A Novel Variational PDE Technique for Image Denoising’. Pp. 501–8 in. Springer, Berlin, Heidelberg.

Beija, Mariana, Carlos A. M. Afonso, and José M. G. Martinho. 2009. ‘Synthesis and Applications of Rhodamine Derivatives as Fluorescent Probes’. *Chemical Society Reviews* 38(8):2410.

Bettencourt-Dias, Mónica and David M. Glover. 2007. ‘Centrosome Biogenesis and Function: Centrosomics Brings New Understanding’. *Nature Reviews Molecular Cell Biology* 8(6):451–63.

Betzig, Eric, George H. Patterson, Rachid Sougrat, O. Wolf Lindwasser, Scott Olenych, Juan S. Bonifacino, Michael W. Davidson, Jennifer Lippincott-Schwartz, and Harald F. Hess. 2006. ‘Imaging Intracellular Fluorescent Proteins at Nanometer Resolution’. *Science* 313(5793):1642–45.

Bianchini, Paolo, Chiara Peres, Michele Oneto, Silvia Galiani, Giuseppe Vicidomini, and Alberto Diaspro. 2015. ‘STED Nanoscopy: A Glimpse into the Future’. *Cell and Tissue Research* 360(1):143–50.

Bonnes, Dominique, Catherine Heukle, Colette Simon, and Dominique Pantaloni. 1985. 4’,6-Diamidino-2-Phenylindole, a Fluorescent Probe for Tubulin and Microtubules, *The Journal of Biological Chemistry*. Vol. 260.

Bürgers, Jana, Irina Pavlova, Juan E. Rodriguez-Gatica, Christian Henneberger, Marc Oeller, Jan A. Ruland, Jan P. Siebrasse, Ulrich Kubitscheck, and Martin K. Schwarz. 2019. ‘Light-Sheet Fluorescence Expansion Microscopy: Fast Mapping of Neural Circuits at Super Resolution’. *Neurophotonics* 6(01):1.

Cahoon, Cori K., Zulin Yu, Yongfu Wang, Fengli Guo, Jay R. Unruh, Brian D. Slaughter, and R. Scott Hawley. 2017. 'Superresolution Expansion Microscopy Reveals the Three-Dimensional Organization of the *Drosophila* Synaptonemal Complex'. *Proceedings of the National Academy of Sciences* 201705623.

Chang, Jae-Byum Byum, Fei Chen, Young-Gyu Gyu Yoon, Erica E. Jung, Hazen Babcock, Jeong Seuk Kang, Shoh Asano, Ho-Jun Jun Suk, Nikita Pak, Paul W. Tillberg, Asmamaw T. Wassie, Dawen Cai, and Edward S. Boyden. 2017. 'Iterative Expansion Microscopy'. *Nature Methods* 14(6):593–99.

Chen, Fei, Paul W. Tillberg, and Edward S. Boyden. 2015. 'Expansion Microscopy'. *Science* Vol. 347, Issue 6221, pp. 543-548.

Chiang, Cheng-Feng, David T. Okou, Tony B. Griffin, C. Reynol. Verret, and Myron N. V. Williams. 2001. 'Green Fluorescent Protein Rendered Susceptible to Proteolysis: Positions for Protease-Sensitive Insertions'. *Archives of Biochemistry and Biophysics* 394(2):229–35.

Chozinski, Tyler J., Aaron R. Halpern, Haruhisa Okawa, Hyeon Jin Kim, Grant J. Tremel, Rachel O. L. Wong, and Joshua C. Vaughan. 2016. 'Expansion Microscopy with Conventional Antibodies and Fluorescent Proteins'. *Nature Methods* 13(6):485–88.

Chozinski, Tyler Joseph. 2018. 'Expansion Microscopy for the Interrogation of Nanoscale Features in Complex Biological Systems'.

Chrambach, Andreas. 1985. *The Practice of Quantitative Gel Electrophoresis*. Frist Edition. Weinheim, Germany.

Chung, Kwanghun and Karl Deisseroth. 2013. 'CLARITY for Mapping the Nervous System'. *Nature Methods* 10(6):508–13.

Cipriano, Bani H., Stephen J. Banik, Renu Sharma, Dominic Rumore, Wonseok Hwang, Robert M. Briber, and Srinivasa R. Raghavan. 2014. 'Superabsorbent Hydrogels That Are Robust and Highly Stretchable'. *Macromolecules* 47(13):4445–52.

D'Este, Elisa, Dirk Kamin, Francisco Balzarotti, and Stefan W. Hell. 2017. 'Ultrastructural Anatomy of Nodes of Ranvier in the Peripheral Nervous System as Revealed by STED Microscopy'. *Proceedings of the National Academy of Sciences* 114(2):E191–99.

Díaz, J. F., J. M. Valpuesta, P. Chacón, G. Diakun, and J. M. Andreu. 1998. 'Changes in Microtubule Protofilament Number Induced by Taxol Binding to an Easily Accessible Site. Internal Microtubule Dynamics.' *The Journal of Biological Chemistry* 273(50):33803–10.

Düring, Daniel Normen, Mariana Diales Rocha, Falk Dittrich, Manfred Gahr, and Richard Hans Robert Hahnloser. 2019. 'Expansion Light Sheet Microscopy Resolves Subcellular Structures in Large Portions of the Songbird Brain'. *Frontiers in Neuroanatomy* 13:2.

Fan, Junchao, Xiaoshuai Huang, Liuju Li, Shan Tan, and Liangyi Chen. 2019. 'A Protocol for Structured Illumination Microscopy with Minimal Reconstruction

Artifacts'. *Biophysics Reports* 5(2):80–90.

Fish, Kenneth N. 2009. 'Total Internal Reflection Fluorescence (TIRF) Microscopy.' *Current Protocols in Cytometry* Chapter 12:Unit12.18.

Freifeld, Limor, Iris Odstrcil, Dominique Förster, Alyson Ramirez, James A. Gagnon, Owen Randlett, Emma K. Costa, Shoh Asano, Orhan T. Celiker, Ruixuan Gao, Daniel A. Martin-Alarcon, Paul Reginato, Cortni Dick, Linlin Chen, David Schoppik, Florian Engert, Herwig Baier, and Edward S. Boyden. 2017. 'Expansion Microscopy of Zebrafish for Neuroscience and Developmental Biology Studies.' *Proceedings of the National Academy of Sciences of the United States of America* 201706281.

Gambarotto, Davide, Fabian U. Zwettler, Maeva Le Guennec, Marketa Schmidt-Cernohorska, Denis Fortun, Susanne Borgers, Jörn Heine, Jan-Gero Schloetel, Matthias Reuss, Michael Unser, Edward S. Boyden, Markus Sauer, Virginie Hamel, and Paul Guichard. 2019. 'Imaging Cellular Ultrastructures Using Expansion Microscopy (U-ExM)'. *Nature Methods* 16(1):71–74.

Gao, Mengfei, Riccardo Maraspini, Oliver Beutel, Amin Zehtabian, Britta Eickholt, Alf Honigmann, and Helge Ewers. 2018. 'Expansion Stimulated Emission Depletion Microscopy (ExSTED)'. *ACS Nano* 12(5):4178–85.

Gao, Ruixuan, Shoh M. Asano, Srigokul Upadhyayula, Igor Pisarev, Daniel E. Milkie, Tsung-Li Liu, Ved Singh, Austin Graves, Grace H. Huynh, Yongxin Zhao, John Bogovic, Jennifer Colonell, Carolyn M. Ott, Christopher Zugates, Susan Tappan, Alfredo Rodriguez, Kishore R. Mosaliganti, Shu-Hsien Sheu, H. Amalia Pasolli, Song Pang, C. Shan Xu, Sean G. Megason, Harald Hess, Jennifer Lippincott-Schwartz, Adam Hantman, Gerald M. Rubin, Tom Kirchhausen, Stephan Saalfeld, Yoshinori Aso, Edward S. Boyden, and Eric Betzig. 2019. 'Cortical Column and Whole-Brain Imaging with Molecular Contrast and Nanoscale Resolution.' *Science* 363(6424):eaau8302.

Göttfert, Fabian, Tino Pleiner, Jörn Heine, Volker Westphal, Dirk Görlich, Steffen J. Sahl, and Stefan W. Hell. 2017. 'Strong Signal Increase in STED Fluorescence Microscopy by Imaging Regions of Subdiffraction Extent.' *Proceedings of the National Academy of Sciences of the United States of America* 114(9):2125–30.

Gould, Travis J., Daniel Burke, Joerg Bewersdorf, and Martin J. Booth. 2012. 'Adaptive Optics Enables 3D STED Microscopy in Aberrating Specimens.' *Optics Express* 20(19):20998–9.

Grimm, Jonathan B., Anand K. Muthusamy, Yajie Liang, Timothy A. Brown, William C. Lemon, Ronak Patel, Rongwen Lu, John J. Macklin, Philipp J. Keller, Na Ji, and Luke D. Lavis. 2017. 'A General Method to Fine-Tune Fluorophores for Live-Cell and in Vivo Imaging.' *Nature Methods* 14(10):987–94.

Gustafsson, M. G. L. 2000. 'Surpassing the Lateral Resolution Limit by a Factor of Two Using Structured Illumination Microscopy.'. *Journal of Microscopy* 98(2):82–87.

Gustafsson, Mats G. L., Lin Shao, Peter M. Carlton, C. J. Rache. Wang, Inna N.

Golubovskaya, W. Zacheus Cande, David A. Agard, and John W. Sedat. 2008. ‘Three-Dimensional Resolution Doubling in Wide-Field Fluorescence Microscopy by Structured Illumination’. *Biophysical Journal* 94(12):4957–70.

Halpern, Aaron R., Germain C. M. Alas, Tyler J. Chozinski, Alexander R. Paredez, and Joshua C. Vaughan. 2017. ‘Hybrid Structured Illumination Expansion Microscopy Reveals Microbial Cytoskeleton Organization’. *ACS Nano* acsnano.7b07200.

Heilemann, Mike, Sebastian van de Linde, Anindita Mukherjee, and Markus Sauer. 2009. ‘Super-Resolution Imaging with Small Organic Fluorophores’. *Angewandte Chemie International Edition* 48(37):6903–8.

Heilemann, Mike, Sebastian van de Linde, Mark Schüttpelz, Robert Kasper, Britta Seefeldt, Anindita Mukherjee, Philip Tinnefeld, and Markus Sauer. 2008. ‘Subdiffraction-Resolution Fluorescence Imaging with Conventional Fluorescent Probes’. *Angewandte Chemie International Edition* 47(33):6172–76.

Heine, Jörn, Matthias Reuss, Benjamin Harke, Elisa D’Este, Steffen J. Sahl, and Stefan W. Hell. 2017. ‘Adaptive-Illumination STED Nanoscopy’. *Proceedings of the National Academy of Sciences* (11):201708304.

Hell, Stefan W. and Jan Wichmann. 1994. ‘Stimulated-Emission-Depletion Fluorescence Microscopy’. *Optics Letters* 19(11):780–82.

Holback, H., Y. Yeo, and K. Park. 2011. *Hydrogel Swelling Behavior and Its Biomedical Applications*. Woodhead Publishing Limited.

Holland, Andrew J., Weijie Lan, and Don W. Cleveland. 2010. ‘Centriole Duplication: A Lesson in Self-Control.’ *Cell Cycle* 9(14):2731–36.

Howard, Jonathon and Anthony A. Hyman. 2007. ‘Microtubule Polymerases and Depolymerases’. *Current Opinion in Cell Biology* 19(1):31–35.

Huang, Bo, Wenqin Wang, Mark Bates, and Xiaowei Zhuang. 2008. ‘Three-Dimensional Super-Resolution Imaging by Stochastic Optical Reconstruction Microscopy’. *Science* 319(5864):810–13.

Jiang, Nan, Hyeon-Jin Kim, Tyler J. Chozinski, Jorge E. Azpurua, Benjamin A. Eaton, Joshua C. Vaughan, and Jay Z. Parrish. 2018. ‘Superresolution Imaging of *Drosophila* Tissues Using Expansion Microscopy’ edited by D. Montell. *Molecular Biology of the Cell* 29(12):1413–21.

Jimenez, Angélique, Karoline Friedl, and Christophe Leterrier. 2019. ‘About Samples, Giving Examples: Optimized Single Molecule Localization Microscopy’. *Methods*.

Juette, Manuel F., Travis J. Gould, Mark D. Lessard, Michael J. Mlodzianoski, Bhupendra S. Nagpure, Brian T. Bennett, Samuel T. Hess, and Joerg Bewersdorf. 2008. ‘Three-Dimensional Sub-100 Nm Resolution Fluorescence Microscopy of Thick Samples’. *Nature Methods* 5(6):527–29.

Juillerat, Alexandre, Thomas Gronemeyer, Antje Keppler, Susanne Gendreizig, Horst Pick, Horst Vogel, and Kai Johnsson. 2003. ‘Directed Evolution of O6-Alkylguanine-DNA Alkyltransferase for Efficient Labeling of Fusion Proteins with

Small Molecules in Vivo.' *Chemistry & Biology* 10(4):313–17.

Jungmann, Ralf, Christian Steinhauer, Max Scheible, Anton Kuzyk, Philip Tinnefeld, and Friedrich C. Simmel. 2010. 'Single-Molecule Kinetics and Super-Resolution Microscopy by Fluorescence Imaging of Transient Binding on DNA Origami'. *Nano Letters* 10(11):4756–61.

Keppler, Antje, Susanne Gendreizig, Thomas Gronemeyer, Horst Pick, Horst Vogel, and Kai Johnsson. 2003. 'A General Method for the Covalent Labeling of Fusion Proteins with Small Molecules in Vivo'. *Nature Biotechnology* 21(1):86–89.

Kim, Doyeon, Taeyeon Kim, Jooyong Lee, and Sang‐Hee Shim. 2019. 'Amplified Expansion Stimulated Emission Depletion Microscopy'. *ChemBioChem* 20(10):1260–65.

Klar, T. A., S. Jakobs, M. Dyba, A. Egner, and S. W. Hell. 2000. 'Fluorescence Microscopy with Diffraction Resolution Barrier Broken by Stimulated Emission.' *Proceedings of the National Academy of Sciences of the United States of America* 97(15):8206–10.

Ku, Taeyun, Justin Swaney, Jeong-Yoon Park, Alexandre Albanese, Evan Murray, Jae Hun Cho, Young-Gyun Park, Vamsi Mangena, Jiapei Chen, and Kwanghun Chung. 2016. 'Multiplexed and Scalable Super-Resolution Imaging of Three-Dimensional Protein Localization in Size-Adjustable Tissues'. *Nature Biotechnology.* 34, pages 973–981

Kukic, Ira, Felix Rivera-Molina, and Derek Toomre. 2016. 'The IN/OUT Assay: A New Tool to Study Ciliogenesis'. *Cilia* 5(1):23.

Lawo, Steffen, Monica Hasegan, Gagan D. Gupta, and Laurence Pelletier. 2012. 'Subdiffraction Imaging of Centrosomes Reveals Higher-Order Organizational Features of Pericentriolar Material'. *Nature Cell Biology* 14(11):1148–58.

Leterrier, Christophe, Jean Potier, Ghislaine Caillol, Claire Debarnot, Fanny Rueda Boroni, and Bénédicte Dargent. 2015. 'Nanoscale Architecture of the Axon Initial Segment Reveals an Organized and Robust Scaffold'. *Cell Reports* 13(12):2781–93.

Li, Rongqin, Xuanze Chen, Zixi Lin, Yao Wang, and Yujie Sun. 2018. 'Expansion Enhanced Nanoscopy'. *Nanoscale* 10(37):17552–56.

Lin, Rui, Qiru Feng, Peng Li, Ping Zhou, Ruiyu Wang, Zhe Liu, Zhiqiang Wang, Xiangbing Qi, Nan Tang, Feng Shao, and Minmin Luo. 2018. 'A Hybridization-Chain-Reaction-Based Method for Amplifying Immunosignals'. *Nature Methods* volume 15, pages 275–278.

Liu, Cheng-Hsin and Matthew Neil Rasband. 2019. 'Axonal Spectrins: Nanoscale Organization, Functional Domains and Spectrinopathies'. *Frontiers in Cellular Neuroscience* 13:234.

Los, Georgyi V., Lance P. Encell, Mark G. McDougall, Danette D. Hartzell, Natasha Karassina, Chad Zimprich, Monika G. Wood, Randy Learish, Rachel Friedman

Ohana, Marjeta Urh, Dan Simpson, Jacqui Mendez, Kris Zimmerman, Paul Otto, Gediminas Vidugiris, Ji Zhu, Aldis Darzins, Dieter H. Klaubert, Robert F. Bulleit, and Keith V. Wood. 2008. 'HaloTag: A Novel Protein Labeling Technology for Cell Imaging and Protein Analysis'. *ACS Chemical Biology* 3(6):373–82.

Löwe, Jan, H. Li, K. Downing, and E. Nogales. 2001. 'Refined Structure of Aβ-Tubulin at 3.5 Å Resolution'. *Journal of Molecular Biology* 313(5):1045–57.

Lukinavičius, Gražvydas, Luc Reymond, Elisa D'Este, Anastasiya Masharina, Fabian Göttfert, Haisen Ta, Angelika Güther, Mathias Fournier, Stefano Rizzo, Herbert Waldmann, Claudia Blaukopf, Christoph Sommer, Daniel W. Gerlich, Hans Dieter Arndt, Stefan W. Hell, and Kai Johnsson. 2014. 'Fluorogenic Probes for Live-Cell Imaging of the Cytoskeleton'. *Nature Methods* 11(7):731–33.

Lukinavičius, Gražvydas, Keitaro Umezawa, Nicolas Olivier, Alf Honigmann, Guoying Yang, Tilman Plass, Veronika Mueller, Luc Reymond, Ivan R. Corrêa Jr, Zhen-Ge Luo, Carsten Schultz, Edward A. Lemke, Paul Heppenstall, Christian Eggeling, Suliana Manley, and Kai Johnsson. 2013. 'A Near-Infrared Fluorophore for Live-Cell Super-Resolution Microscopy of Cellular Proteins'. *Nature Chemistry* 5(2):132–39.

Ma, Xiaoyu, Xiangcheng Sun, Derek Hargrove, Jun Chen, Donghui Song, Qiuchen Dong, Xiuling Lu, Tai-Hsi Fan, Youjun Fu, and Yu Lei. 2016. 'A Biocompatible and Biodegradable Protein Hydrogel with Green and Red Autofluorescence: Preparation, Characterization and In Vivo Biodegradation Tracking and Modeling'. *Scientific Reports* 6(1):19370.

Mahecic, Dora, Ilaria Testa, Juliette Griffié, and Suliana Manley. 2019. 'Strategies for Increasing the Throughput of Super-Resolution Microscopies'. *Current Opinion in Chemical Biology* 51:84–91.

Maitra, Jaya and Vivek Kumar Shukla. 2014. 'Cross-Linking in Hydrogels - A Review'. *American Journal of Polymer Science* 4(2):25–31.

Mandelkow, E. M., E. Mandelkow, and R. A. Milligan. 1991. 'Microtubule Dynamics and Microtubule Caps: A Time-Resolved Cryo-Electron Microscopy Study.' *The Journal of Cell Biology* 114(5):977–91.

Mattheyses, Alexa L., Sanford M. Simon, and Joshua Z. Rappoport. 2010. 'Imaging with Total Internal Reflection Fluorescence Microscopy for the Cell Biologist.' *Journal of Cell Science* 123(Pt 21):3621–28.

McNally, James G., Tatiana Karpova, John Cooper, and José Angel Conchello. 1999. 'Three-Dimensional Imaging by Deconvolution Microscopy'. *Methods* 19(3):373–85.

Melak, Michael, Matthias Plessner, and Robert Grosse. 2017. 'Correction: Actin Visualization at a Glance'. *Journal of Cell Science* 130(9):1688–1688.

Mikhaylova, Marina, Bas M. C. Cloin, Kieran Finan, Robert Van Den Berg, Jalmar Teeuw, Marta M. Kijanka, Mikolaj Sokolowski, Eugene A. Katrukha, Manuel Maidorn, Felipe Opazo, Sandrine Moutel, Marylin Vantard, Frank Perez, Paul M.

P. Van Bergen En Henegouwen, Casper C. Hoogenraad, Helge Ewers, and Lukas C. Kapitein. 2015. 'Resolving Bundled Microtubules Using Anti-Tubulin Nanobodies'. *Nature Communications* 6(May):1–7.

Mirvis, Mary, Tim Stearns, and W. James Nelson. 2018. 'Cilium Structure, Assembly, and Disassembly Regulated by the Cytoskeleton.' *The Biochemical Journal* 475(14):2329–53.

Mortensen, Kim I., L. Stirling Churchman, James A. Spudich, and Henrik Flyvbjerg. 2010. 'Optimized Localization Analysis for Single-Molecule Tracking and Super-Resolution Microscopy'. *Nature Methods* 7(5):377–81.

Murray, John M., Paul L. Appleton, Jason R. Swedlow, and Jennifer C. Waters. 2007. 'Evaluating Performance in Three-Dimensional Fluorescence Microscopy'. *Journal of Microscopy* 228(3):390–405.

Nogales, Eva, Sharon G. Wolf, and Kenneth H. Downing. 1998. *Structure of the Tubulin Dimer by Electron Crystallography*. Vol. 391.

Olivier, Nicolas, Debora Keller, Pierre Gönczy, and Suliana Manley. 2013. 'Resolution Doubling in 3D-STORM Imaging through Improved Buffers' edited by M. Sauer. *PLoS ONE* 8(7):e69004.

Opazo, Felipe, Matthew Levy, Michelle Byrom, Christina Schäfer, Claudia Geisler, Teja W. Groemer, Andrew D. Ellington, and Silvio O. Rizzoli. 2012. 'Aptamers as Potential Tools for Super-Resolution Microscopy'. *Nature Methods* 9(10):938–39.

Oreopoulos, John, Richard Berman, and Mark Browne. 2014. *Spinning-Disk Confocal Microscopy. Present Technology and Future Trends*. Vol. 123. 1st ed. Elsevier Inc.

Ott, Carolyn and Jennifer Lippincott-Schwartz. 2012. 'Visualization of Live Primary Cilia Dynamics Using Fluorescence Microscopy.' *Current Protocols in Cell Biology* Chapter 4:

Park, Suk-Youl, Jung-Eun Park, Tae-Sung Kim, Ju Hee Kim, Mi-Jeong Kwak, Bonsu Ku, Lan Tian, Ravichandran N. Murugan, Mija Ahn, Shinobu Komiya, Hironobu Hojo, Nam-Hyung Kim, Bo Yeon Kim, Jeong K. Bang, Raymond L. Erikson, Ki Won Lee, Seung Jun Kim, Byung-Ha Oh, Wei Yang, and Kyung S. Lee. 2014. 'Molecular Basis for Unidirectional Scaffold Switching of Human Plk4 in Centriole Biogenesis.' *Nature Structural & Molecular Biology* 21(8):696–703.

Patton, Brian R., Daniel Burke, David Owald, Travis J. Gould, Joerg Bewersdorf, and Martin J. Booth. 2016. 'Three-Dimensional STED Microscopy of Aberrating Tissue Using Dual Adaptive Optics'. *Optics Express* 24(8):8862.

Pavani, S. R. P., M. A. Thompson, J. S. Biteen, S. J. Lord, N. Liu, R. J. Twieg, R. Piestun, and W. E. Moerner. 2009. 'Three-Dimensional, Single-Molecule Fluorescence Imaging beyond the Diffraction Limit by Using a Double-Helix Point Spread Function'. *Proceedings of the National Academy of Sciences* 106(9):2995–99.

Pesce, Luca, Marco Cozzolino, Luca Lanzanò, Alberto Diaspro, and Paolo Bianchini.

2019. ‘Measuring Expansion from Macro- to Nanoscale Using NPC as Intrinsic Reporter’. Journal of Biophotonics e201900018.

Platonova, Evgenia, Christian M. Winterflood, and Helge Ewers. 2015. ‘Letter A Simple Method for GFP- and RFP-Based Dual Color Single Molecule Localization Microscopy’. *ACS Chemical Biology* 10(6):1411–16.

Reiter, Jeremy F. and Michel R. Leroux. 2017. ‘Genes and Molecular Pathways Underpinning Ciliopathies’. *Nature Reviews Molecular Cell Biology* 18(9):533–47.

Rhodin, Johannes and Tore Dalhamn. 1956. 'Electron Microscopy of the tracheal ciliated mucosa in rat.' *Springer*

Richardson, Douglas S. and Jeff W. Lichtman. 2017. ‘SnapShot: Tissue Clearing’. *Cell* 171(2):496-496.e1.

Ries, Jonas, Charlotte Kaplan, Evgenia Platonova, Hadi Eghlidi, and Helge Ewers. 2012. ‘A Simple, Versatile Method for GFP-Based Super-Resolution Microscopy via Nanobodies’. *Nature Methods* 9(6):582–84.

Rüchel, Reinhard and Myles D. Brager. 1975. ‘Scanning Electron Microscopic Observations of Polyacrylamide Gels’. *Analytical Biochemistry* 68(2):415–28.

Rüchel, Reinhard, Russell L. Steere, and Eric F. Erbe. 1978. ‘Transmission-Electron Microscopic Observations of Freeze-Etched Polyacrylamide Gels’. *Journal of Chromatography A* 166(2):563–75.

Rust, Michael J., Mark Bates, and Xiaowei Zhuang. 2006. ‘Sub-Diffraction-Limit Imaging by Stochastic Optical Reconstruction Microscopy (STORM)’. *Nature Methods* 3(10):793–96.

Sadeghi, Mohammad and Hossein Hosseinzadeh. 2010. ‘Swelling Behaviour of a Novel Protein-Based Super Absorbent Hydrogel Composed of Poly(Methacrylic Acid) and Collagen’. *Asian Journal of Chemistry* 22(9):6734–46.

Sage, Daniel, Hagai Kirshner, Thomas Pengo, Nico Stuurman, Junhong Min, Suliana Manley, and Michael Unser. 2015. ‘Quantitative Evaluation of Software Packages for Single-Molecule Localization Microscopy’. *Nature Methods* 12(8):717–24.

Sage, Daniel, Thanh-An Pham, Hazen Babcock, Tomas Lukes, Thomas Pengo, Jerry Chao, Ramraj Velmurugan, Alex Herbert, Anurag Agrawal, Silvia Colabrese, Ann Wheeler, Anna Archetti, Bernd Rieger, Raimund Ober, Guy M. Hagen, Jean-Baptiste Sibarita, Jonas Ries, Ricardo Henriques, Michael Unser, and Seamus Holden. 2019. ‘Super-Resolution Fight Club: Assessment of 2D and 3D Single-Molecule Localization Microscopy Software’. *Nature Methods* 16(5):387–95.

Salem, Michèle, Yves Mauguen, and Thierry Prangé. 2010. ‘Revisiting Glutaraldehyde Cross-Linking: The Case of the Arg-Lys Intermolecular Doublet.’ *Acta Crystallographica. Section F, Structural Biology and Crystallization Communications* 66(Pt 3):225–28.

Scheible, Max B. and Philip Tinnefeld. 2018. ‘Quantifying Expansion Microscopy in 2D

Using DNA Origami Nanostructures'. *BioRxiv* https://doi.org/10.1101/265405

Schermelleh, Lothar, Alexia Ferrand, Thomas Huser, Christian Eggeling, Markus Sauer, Oliver Biehlmaier, and Gregor P. C. Drummen. 2019. 'Super-Resolution Microscopy Demystified'. *Nature Cell Biology* 21(1):72–84.

Schermelleh, Lothar, Rainer Heintzmann, and Heinrich Leonhardt. 2010. 'A Guide to Super-Resolution Fluorescence Microscopy'. *Journal of Cell Biology* 190(2):165–75.

Schiff, Peter, Jane Fant and Susan Horwitz. 1979. 'Promotion of Microtubule Assembly in Vitro by Taxol'. *Nature* 277(5698):665–67.

Schindelin, Johannes, Ignacio Arganda-Carreras, Erwin Frise, Verena Kaynig, Mark Longair, Tobias Pietzsch, Stephan Preibisch, Curtis Rueden, Stephan Saalfeld, Benjamin Schmid, Jean-Yves Tinevez, Daniel James White, Volker Hartenstein, Kevin Eliceiri, Pavel Tomancak, and Albert Cardona. 2012. 'Fiji: An Open-Source Platform for Biological-Image Analysis'. *Nature Methods* 9(7):676–82.

Schlichthaerle, Thomas, Maximilian T. Strauss, Florian Schueder, Alexander Auer, Bianca Nijmeijer, Moritz Kueblbeck, Vilma Jimenez Sabinina, Jonas Ries, Jan Ellenberg, and Ralf Jungmann. 2019. 'Direct Visualization of Single Nuclear Pore Complex Proteins Using Genetically-Encoded Probes for DNA-PAINT'. *BioRxiv* 579961.

Schlichthaerle, Thomas, Maximilian T. Strauss, Florian Schueder, Alexander Auer, Bianca Nijmeijer, Moritz Kueblbeck, Vilma Jimenez Sabinina, Jervis V. Thevathasan, Jonas Ries, Jan Ellenberg, and Ralf Jungmann. 2019. 'Direct Visualization of Single Nuclear Pore Complex Proteins Using Genetically-Encoded Probes for DNA-PAINT'. *BioRxiv* 579961.

Schnitzbauer, Joerg, Maximilian T. Strauss, Thomas Schlichthaerle, Florian Schueder, and Ralf Jungmann. 2017. 'Super-Resolution Microscopy with DNA-PAINT'. *Nature Protocols* 12(6):1198–1228.

Seeley, E. Scott and Maxence V Nachury. 2010. 'The Perennial Organelle: Assembly and Disassembly of the Primary Cilium.' *Journal of Cell Science* 123(Pt 4):511–18.

Shi, Xiaoyu, Qi Li, Zhipeng Dai, Arthur A. Tran, Siyu Feng, Alejandro D. Ramirez, Zixi Lin, Xiaomeng Wang, Tracy T. Chow, Ian B. Seiple, and Bo Huang. 2019. 'Label-Retention Expansion Microscopy'. *BioRxiv* 687954.

Shotton, David M. 1989. '*REVIEW Confocal Scanning* Optical Microscopy and Its Applications for Biological Specimens.' *Journal of Cell Science* 94:175-206.

Shroff, Hari, Helen White, and Eric Betzig. 2008. 'Photoactivated Localization Microscopy (PALM) of Adhesion Complexes'. *Curr. Protoc. Cell Biol*. 4:Unit 4.21

Sibarita, Jean-Baptiste. 2005. 'Deconvolution Microscopy'. Pp. 201–43 in. Springer, Berlin, Heidelberg.

Sieben, Christian, Niccolò Banterle, Kyle M. Douglass, Pierre Gönczy, and Suliana

Manley. 2018. ‘Multicolor Single-Particle Reconstruction of Protein Complexes’. *Nature Methods* 15(10):777–80.

Singla, Veena and Jeremy F. Reiter. 2006. ‘The Hedgehog Response Network: Sensors, Switches, and Routers’. *Science* 304(5678):1755–59.

Sonnen, Katharina F., Anna-Maria Gabryjonczyk, Eduard Anselm, York-Dieter Stierhof, and Erich A. Nigg. 2013. ‘Human Cep192 and Cep152 Cooperate in Plk4 Recruitment and Centriole Duplication.’ *Journal of Cell Science* 126(Pt 14):3223–33.

Sonnen, Katharina Friederike. 2012. *Investigation of Human Centrosomes-with a Special Focus on the Function of Cep152 and Cep192 in Centriole Duplication*.

Sun, Xiaoli, Aihua Zhang, Brenda Baker, Luo Sun, Angela Howard, John Buswell, Damien Maurel, Anastasiya Masharina, Kai Johnsson, Christopher J. Noren, Ming-Qun Xu, and Ivan R. Corrêa. 2011. ‘Development of SNAP-Tag Fluorogenic Probes for Wash-Free Fluorescence Imaging.’ *Chembiochem : A European Journal of Chemical Biology* 12(14):2217–26.

Thevathasan, Jervis Vermal, Maurice Kahnwald, Konstanty Cieśliński, Philipp Hoess, Sudheer Kumar Peneti, Manuel Reitberger, Daniel Heid, Krishna Chaitanya Kasuba, Sarah Janice Hoerner, Yiming Li, Yu-Le Wu, Markus Mund, Ulf Matti, Pedro Matos Pereira, Ricardo Henriques, Bianca Nijmeijer, Moritz Kueblbeck, Vilma Jimenez Sabinina, Jan Ellenberg, and Jonas Ries. 2019. ‘Nuclear Pores as Versatile Reference Standards for Quantitative Superresolution Microscopy’. *BioRxiv* 582668.

Thompson, Russell E., Daniel R. Larson, and Watt W. Webb. 2002. ‘Precise Nanometer Localization Analysis for Individual Fluorescent Probes’. *Biophysical Journal* 82(5):2775–83.

Tiede, Christian, Anna A. S. Tang, Sarah E. Deacon, Upasana Mandal, Joanne E. Nettleship, Robin L. Owen, Suja E. George, David J. Harrison, Raymond J. Owens, Darren C. Tomlinson, and Michael J. McPherson. 2014. ‘Adhiron: A Stable and Versatile Peptide Display Scaffold for Molecular Recognition Applications.’ *Protein Engineering, Design & Selection : PEDS* 27(5):145–55.

Tillberg, Paul W., Fei Chen, Kiryl D. Piatkevich, Yongxin Zhao, Chih-Chieh Yu, Brian P. English, Linyi Gao, Anthony Martorell, Ho-Jun Suk, Fumiaki Yoshida, Ellen M. DeGennaro, Douglas H. Roossien, Guanyu Gong, Uthpala Seneviratne, Steven R. Tannenbaum, Robert Desimone, Dawen Cai, and Edward S. Boyden. 2016. ‘Protein-Retention Expansion Microscopy of Cells and Tissues Labeled Using Standard Fluorescent Proteins and Antibodies’. *Nature Biotechnology* 34(9):987–92.

Tillberg, PW. 2016. ‘Expansion Microscopy: Improving Imaging through Uniform Tissue Expansion’.

Tilney, L. G., J. Bryan, D. J. Bush, K. Fujiwara, M. S. Mooseker, D. B. Murphy, and D. H. Snyder. 1973. ‘Microtubules: Evidence for 13 Protofilaments.’ *The Journal of*

Cell Biology 59(2 Pt 1):267–75.

Tokunaga, Makio, Naoko Imamoto, and Kumiko Sakata-Sogawa. 2007. 'Highly Inclined Thin Illumination Enables Clear Single-Molecule Imaging in Cells'. *Nature Methods* 5(2).

Tomer, Raju, Li Ye, Brian Hsueh, and Karl Deisseroth. 2014. 'Advanced CLARITY for Rapid and High-Resolution Imaging of Intact Tissues'. *Nature Protocols* 9(7):1682–97.

Tong, Zhisong, Paolo Beuzer, Qing Ye, Joshua Axelrod, Zhenmin Hong, and Hu Cang. 2016. 'ExM - STORM : Expansion Single Molecule Nanoscopy'. https://doi.org/10.1101/049403.

Tony Yang, T., Jimmy Su, Won-Jing Wang, Branch Craige, George B. Witman, Meng-Fu Bryan Tsou, and Jung-Chi Liao. 2015. 'Superresolution Pattern Recognition Reveals the Architectural Map of the Ciliary Transition Zone'. *Scientific Reports* 5(1):14096.

Truckenbrodt, Sven, Manuel Maidorn, Dagmar Crzan, Hanna Wildhagen, Selda Kabatas, and Silvio O. Rizzoli. 2018. 'X10 Expansion Microscopy Enables 25-Nm Resolution on Conventional Microscopes.' *EMBO Reports* e45836.

Truckenbrodt, Sven, Christoph Sommer, Silvio O. Rizzoli, and Johann G. Danzl. 2019. 'A Practical Guide to Optimization in X10 Expansion Microscopy'. *Nature Protocols* 14(3):832–63.

Tsai, Yun-Chi, Wei-Chun Tang, Christine Siok Lan Low, Yen-Ting Liu, Jyun-Sian Wu, Po-Yi Lee, Lindsay Quinn Chen, Yi-Ling Lin, Pakorn Kanchanawong, Liang Gao, and Bi-Chang Chen. 2019. 'Rapid High Resolution 3D Imaging of Expanded Biological Specimens with Lattice Light Sheet Microscopy'. *Methods*.

Turcotte, Raphaël, Yajie Liang, Masashi Tanimoto, Qinrong Zhang, Ziwei Li, Minoru Koyama, Eric Betzig, and Na Ji. 2019. 'Dynamic Super-Resolution Structured Illumination Imaging in the Living Brain.' *Proceedings of the National Academy of Sciences of the United States of America* 116(19):9586–91.

Unnersjö-Jess, David, Lena Scott, Sonia Zambrano Sevilla, Jaakko Patrakka, Hans Blom, and Hjalmar Brismar. 2018. 'Confocal Super-Resolution Imaging of the Glomerular Filtration Barrier Enabled by Tissue Expansion.' *Kidney International* 93(4):1008–13.

Wang, Yongfu, Zulin Yu, Cori K. Cahoon, Tari Parmely, Nancy Thomas, Jay R. Unruh, Brian D. Slaughter, and R. Scott Hawley. 2018. 'Combined Expansion Microscopy with Structured Illumination Microscopy for Analyzing Protein Complexes'. *Nature Protocols* 13(8).

Wegel, Eva, Antonia Göhler, B. Christoffer Lagerholm, Alan Wainman, Stephan Uphoff, Rainer Kaufmann, and Ian M. Dobbie. 2016. 'Imaging Cellular Structures in Super-Resolution with SIM, STED and Localisation Microscopy: A Practical Comparison'. *Scientific Reports* 6(May):1–13.

Westphal, Volker and Stefan W. Hell. 2005. 'Nanoscale Resolution in the Focal Plane

of an Optical Microscope'. *Physical Review Letters* 94(14):143903.

Wildanger, D., R. Medda, L. Kastrup, and S. W. Hell. 2009. 'A Compact STED Microscope Providing 3D Nanoscale Resolution'. *Journal of Microscopy* 236(1):35–43.

Xu, Ke, Hazen P. Babcock, and Xiaowei Zhuang. 2012. 'Dual-Objective STORM Reveals Three-Dimensional Filament Organization in the Actin Cytoskeleton'. *Nature Methods* 9(2):185.

Xu, Ke, Guisheng Zhong, and Xiaowei Zhuang. 2013. 'Actin, Spectrin, and Associated Proteins Form a Periodic Cytoskeletal.' *Science.* 339(January):452–56.

Yang, T. Tony, Weng Man Chong, and Jung-Chi Liao. 2016. 'STED and STORM Superresolution Imaging of Primary Cilia'. Pp. 169–92 in.

Yoon, Joshua, Colin J. Comerci, Lucien E. Weiss, Ljiljana Milenkovic, Tim Stearns, and W. E. Moerner. 2019. 'Revealing Nanoscale Morphology of the Primary Cilium Using Super-Resolution Fluorescence Microscopy'. *Biophysical Journal* 116(2):319–29.

You, Yu-Li and M. Kaveh. 2000. Fourth-Order Partial Differential Equations for Noise Removal. *IEEE.*Vol. 9.

Zdankowski, Piotr, Maciej Trusiak, David McGloin, and Jason R. Swedlow. 2019. 'Numerically Enhanced Adaptive Optics-Based 3D STED Microscopy for Deep-Tissue Super-Resolved Imaging'. *BioRxiv* 653394.

Zhao, Yongxin, Octavian Bucur, Humayun Irshad, Fei Chen, Astrid Weins, Andreea L. Stancu, Eun-Young Young Oh, Marcello DiStasio, Vanda Torous, Benjamin Glass, Isaac E. Stillman, Stuart J. Schnitt, Andrew H. Beck, and Edward S. Boyden. 2017. 'Nanoscale Imaging of Clinical Specimens Using Pathology-Optimized Expansion Microscopy'. *Nature Biotechnology* 35(8):757–64.

Zhou, Xianju, Lihui Weng, Qiang Chen, Jianming Zhang, Deyan Shen, Zhuchuan Li, Manjun Shao, and Jian Xu. 2003. 'Investigation of PH Sensitivity of Poly(Acrylic Acid-Co-Acrylamide) Hydrogel'. *Polymer International* 52(7):1153–57.

Zohuriaan-Mehr, Mohammad, J. and Kabiri Kourosh. 2008. 'Superabsorbent Polymer Materials: A Review'. *Iranian Polymer Journal* 17(6):452–54.

Acknowledgment

To start, I would like to thank my supervisor, Prof. Helge Ewers. It was a great pleasure to join his lab in Berlin since the very beginning. I have been watching, listening and learning from him. He taught me not only how to conduct science but also how to enjoy being a scientist.

I am so grateful for my second supervisor, Prof. Francesca Bottanelli, who offered many insightful ideas in the last year of my doctorate work.

I will also appreciate for my collaborators, Dr. Alf Honigmann, with whom we developed the ExSTED, and Isabelle Heing-Becker for the new probe we are working on. It was enjoyable and inspiring to work with them,

I am also thankful for my colleagues: Dr. Hylkje Geertsema and Purba Kashyap for checking my thesis, Dr. Amin Zehtabian for the coding and discussion, Dr. Susanne Fehse and Raluca Groza for being my sunshine the dark days, Saskia Kutz and Ando zehrer for keeping our microscopy facility running, Valentin Fabricius and Jonathan lefebre for the nanobodies, Jiahui Li and Iwona Mucha-Kruczynska for our early years together, Clarie Schlack, Manuela Gibson and Andrea Senge for their helping through the piles of documents.

I also want to thank my parents, Bin Gao and Qin Fan and grandparents, Yongde Fan and Huizhen Sun. I was not good enough and may never be in the future, but I will try my best.

Finally, I thank my friends Xuanbo Zhang, Hong Zheng, Chao Li, who companied me through those white nights. I was very happy to have them around.

2019 夏 柏林

Selbstständigkeitserklärung

Hiermit erkläre ich, dass ich die vorliegende Arbeit mit dem Titel

Combining expansion microscopy with other super-resolution techniques

selbstständig und ohne unerlaubte fremde Hilfe angefertigt, keine anderen als die angegebenen Quellen und Hilfsmittel verwendet und die den verwendeten Quellen und Hilfsmitteln wörtlich oder inhaltlich entnommenen Stellen als solche kenntlich gemacht habe.

Berlin, 20.01.2020

Mengfei Gao